



DeepWind Deliverable

Grant Agreement number: 256769

Project title: Future Deep Sea Wind Turbine Technologies

Deliverable No.: D4.1

Deliverable title: Description of simplified numerical model relevant for development of control concepts

Deliverable status: Closed

Name of lead beneficiary: SINTEF Energi AS

Nature of deliverable: Report(R)

Dissemination level: Public (PU)

Due date from Annex 1: Month 16

Actual submission date: 2012-01-31

Quality check approval by: John O. Tande

date: 2012-06-28

Report

Description of simplified numerical model relevant for development of control concepts

DeepWind Deliverable D4.1

Author(s)

Harald G Svendsen

Karl O Merz

SINTEF Energi AS
SINTEF Energy Research

Address:
P. O. box 4761 Sluppen
NO-7465 Trondheim
NORWAY
Telephone: +47 73597200
Telefax: +47 73597250

energy.research@sintef.no
www.sintef.no/energi
www.sintef.no
Enterprise / VAT No.:
NO 939 350 675 MVA

KEYWORDS:
VAWT, DeepWind, floating
turbine, system

Report

Description of simplified numerical model relevant for development of control concepts

DeepWind Deliverable D4.1

VERSION
1.0

DATE
31st January 2012

AUTHOR(S)
Harald G Svendsen
Karl O Merz

CLIENT(S)
DeepWind consortium, EC

CLIENT'S REFERENCE
D4.1

PROJECT
12X721

NUMBER OF PAGES AND ATTACHMENTS
41 + 45

ABSTRACT

This report gives a description of a simplified numerical model for a floating vertical axis wind turbine relevant for development of control concepts. The model consists of a look-up table of aerodynamic forces based on a double-multiple streamtube representation of the aerodynamics, coupled with spring-damper representations of the most relevant floating tower and mooring system degrees of freedom, a simple representation of the hydrodynamic Magnus effect, and different versions of a model describing the electrical system (generator, converter and grid connection) with varying level of detail.

This model includes the most relevant characteristics and degrees of freedom of the DeepWind turbine, and is well suited for analyses of control concepts without involving too time-consuming simulations.

PREPARED BY
Harald G Svendsen

SIGNATURE


CHECKED BY
John O Tande

SIGNATURE


APPROVED BY
Knut Samdal

SIGNATURE


REPORT NUMBER
TR A7179

ISBN
978-82-594-3507-1

CLASSIFICATION
Unrestricted

CLASSIFICATION THIS PAGE
Unrestricted



Document History

VERSION	DATE	VERSION DESCRIPTION
1.0	2012-01-31	Final version



Contents

1	Introduction	5
1.1	The DeepWind turbine concept	5
1.2	The DeepWind project	6
1.3	Control challenges	6
2	Literature Review	8
2.1	Control of Variable-Speed VAWTs	8
2.2	Torque Control of HAWTs Below the Rated Windspeed	9
2.3	Torque Control of Fixed-Pitch HAWTs Above the Rated Windspeed	9
2.4	Control of Pitch-Regulated Floating Wind Turbines	12
3	Simplified model overview	14
3.1	Assumptions and simplifications	16
3.2	Single degree of freedom spring-damper system	17
4	Aerodynamic model	19
4.1	Double-multiple streamtube model	19
4.2	Table-based model	19
5	Floating tower model	20
5.1	Magnus effect	20
5.2	Shaft twisting	21
5.3	Shaft tilting	22
5.4	Mooring system	25
6	Electrical model	25
6.1	Detailed model – PMSG with full converter	26
6.1.1	Per unit system and dq0 transformation	26
6.1.2	Permanent magnet synchronous generator	27
6.1.3	Converters	28
6.1.4	DC link dynamics	29
6.1.5	Grid voltage and power	30
6.1.6	Control – generator side converter	31
6.1.7	Control – grid side converter	32
6.2	Intermediate model – Speed control with DC link dynamics	34
6.2.1	Speed control (generator and generator side converter)	34
6.2.2	Other simplifications	35
6.3	Basic model – Speed control, no grid representation	35
7	Initial thoughts on control concepts	36
7.1	Aerodynamic Design	36
7.2	Controller Architecture	36
7.3	Considerations for a Floating Platform	37
8	Conclusions	38



ATTACHMENTS

-
1. Karl O. Merz, *A Blade Element Momentum Method for Dynamic Analysis of Vertical Axis Wind Turbines – Rev B*
-

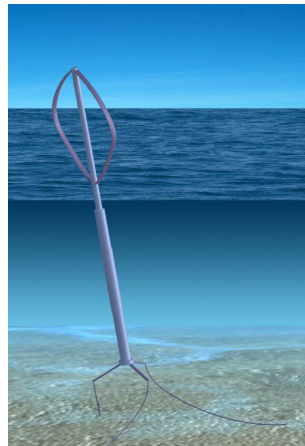


Figure 1: Artistic illustration of the DeepWind turbine

1 Introduction

Land-based vertical axis wind turbines (VAWT) have been investigated in the past and attracted a lot of attention in the 80s and early 90s before they lost ground relative to horizontal axis wind turbines which are predominant today. For very large turbines intended for offshore applications, however, this may change as the costs associated with installation and maintenance become relatively more important. New turbine concepts that offer higher reliability and simpler installation may thus be competitive even if the aerodynamic efficiency is less than for state-of-the art horizontal axis turbines. Such considerations motivate a renewed interest in VAWTs, and a concrete example is the floating wind turbine concept studied in the DeepWind project (see below).

This report gives a description of a simplified numerical model for a floating vertical axis wind turbine relevant for development of control concepts. The model consists of a look-up table of aerodynamic forces based on a double-multiple streamtube representation of the aerodynamics, coupled with spring-damper representations of the most relevant floating tower and mooring system degrees of freedom, a simple representation of the hydrodynamic Magnus effect, and different versions of a model describing the electrical system (generator, converter and grid connection) with varying level of detail.

This model includes the most relevant characteristics and degrees of freedom of the DeepWind turbine, and is well suited for analyses of control concepts without involving too time-consuming simulations.

The model has been implemented in Simulink, which offers a visual interface to the model and is a commonly used simulation framework for analysis of control systems. The more detailed aerodynamic model, however, has been implemented in Fortran. In principle this model can be coupled directly to the Simulink model, but for reasons of simulation speed, the approach we have settled for is to couple the aerodynamics with the rest of the system by means of a set of look-up tables derived from the more detailed model.

1.1 The DeepWind turbine concept

The DeepWind concept is a vertical axis wind turbine with a two-bladed Darrieus rotor. A long rotating shaft extends into the water, with the generator at the bottom end. The floating tower is stabilised by ballast and kept in place by mooring lines attached to the non-rotating part of the generator.

The perceived potential advantages of the DeepWind concept are its simplicity, up-scaling potential and suitability for deep sea sites. Simplicity refers both to the turbine manufacturing, involving e.g. blades made by pultrusion, and installation and maintenance. Up-scaling is important for offshore installations due to the high fixed costs *per turbine unit*. The DeepWind concept has been described in more detail in refs. [1, 2]. An illustration of the DeepWind turbine is shown in Figure 1.



1.2 The DeepWind project

DeepWind [3] is a four-year project funded by the EU's 7th Framework Programme – *Future Emerging Technologies*, and runs from October 2010 to September 2014.

Offshore wind energy is set to play a steadily increasing role as a source of electric power. The hypothesis of the DeepWind project is that a new wind turbine concept developed specifically for offshore application has potential for better cost efficiency than existing offshore technology which is adapted from established onshore designs. Based on this hypothesis the project has the overall objective to explore the technologies needed for development of a new and simple floating offshore concept with a vertical axis rotor and a floating and rotating foundation. An additional objective is to develop calculation and design tools for development and evaluation of very large wind turbines based on this concept.

The project is divided in several work packages (WP), as indicated below.

- WP1 Aero-elastic code and simulation of performance, dynamics and loads
- WP2 Blade technology and blade design
- WP3 Generator concepts
- **WP4 Turbine operational control**
 - **Task 4.1 Numerical code adaptation**
 - Task 4.2 Assessment of alternative rotor control strategies
 - Task 4.3 Assessment of control strategies for grid code compliance
- WP5 Mooring, floating and torque absorption systems
- WP6 Exploration of torque, lift and drag on a rotating tube
- WP7 Proof-of-principle experiments
- WP8 Integration of technologies and upscaling
- WP9 Dissemination and Exploitation
- WP10 Management

The objective of Work Package 4 is to assess and suggest a rational control concept for the turbine. The control concept should consider both normal and abnormal operation, aiming for a system that provides for optimised power performance (aerodynamic efficiency), reduced dynamic stress on tower (shaft) and mooring system, safe rotor braking (emergency stop) as well as grid code compliance (reactive power and voltage control, low-voltage fault ride through, etc).

This report is the deliverable associated with Task 4.1, and gives a description of the simplified turbine model. The emphasis is on the model itself and less on model parameters and model application. The analyses in Tasks 4.2 and 4.3 will be based on the simplified model developed in Task 4.1

1.3 Control challenges

Large wind turbines in general require an active control system to maximise power extraction, minimise structural loads, and comply with grid code requirements. A particular challenge for vertical axis turbines is the large aerodynamic torque ripple due to $2p$ (twice per period) variations in the aerodynamic torque exerted on the rotor. Another challenge is the braking of the turbine at high wind speeds, which without blade pitching must be done via a fast-acting speed control.

For the assessment of control strategies, a stepwise approach is proposed that focusses on the most fundamental control challenges first. In a rough order of priority, the main control challenges for this type of turbine are thought to be:

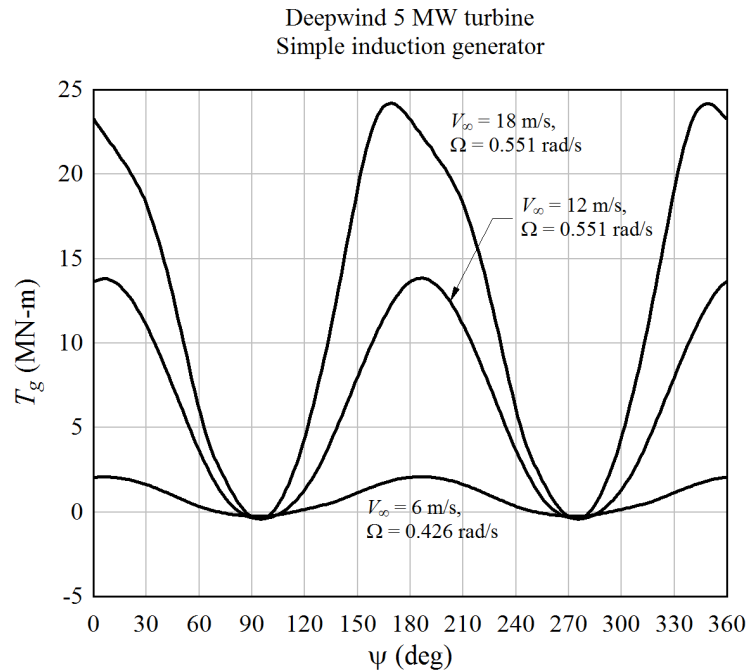


Figure 2: Aerodynamic torque variations during one revolution for different wind speeds and rotational speeds.

- Maximise aerodynamic efficiency, and hence power extraction
- Limit the power at the rated value (at high wind speeds)
- Reduce 2p torque ripple
- Avoid excitation of eigenfrequencies (if possible)
- Reduce impact of grid-side disturbances

Floater stabilisation is thought to be achieved by ballast and mooring system. Negative damping of tower oscillations in the wind direction, which is an important issue for pitch-regulated horizontal axis turbines like Hywind [4], is not considered to be relevant here as the DeepWind turbine is operated without any pitch control.

For the primary control objectives of maximising power extraction and reducing the torque ripple, it is sufficient in the first instance to consider only the aerodynamic model and the shaft twisting, i.e. a setup similar to a land-based turbine. Having achieved satisfactory operation in this case, more model components can be included to validate the results and to address the other issues, such as the control system interaction with structural modes. The dynamics of the electrical system is fast compared to the mechanical dynamics of the turbine, and for many purposes it can therefore be assumed that the actual electrical counter-torque equals the controller set-point value. However, a good and adequately detailed model of the electrical system is important in order to investigate power quality and impact of grid disturbance on the mechanical system and vice versa.

An important difference between VAWT and the more common horizontal axis types is the torque ripple as mentioned above. For a two-bladed turbine, this implies a 2p (twice per revolution) pulsation of the torque, with instantaneous values ranging from near zero to about twice the average value, see Figure 2. This represents a problem both for fatigue lifetime and for the power export into the grid.

The 2p pulsation of the torque/power adds another challenge for the control system, namely in obtaining an instantaneous estimate of the revolution-average rotational speed or power. This is necessary in order to be able to compensate for wind gusts.

Development and analysis of control strategies for the DeepWind turbine is the main objective of Work Package 4 within the DeepWind project. The results of this work will be described in reports due in September 2012 and April 2013. However, some initial thoughts on control strategies are presented in Section 7.



2 Literature Review

A literature review has been conducted, focusing on four topics: variable-speed generator torque control of vertical-axis wind turbines, generator torque control of stall-regulated horizontal-axis wind turbines above the rated windspeed, generator torque control of horizontal-axis wind turbines below the rated windspeed, and control of floating wind turbines. Below the rated windspeed, it makes no difference if the rotor is pitch- or stall-regulated, because the pitch regulation systems are typically not active.

In summary, variable-speed generator torque control has been implemented on utility-scale vertical-axis wind turbines. It is possible to use ac-dc-ac power conversion to reduce or eliminate the $2p$ (for two-bladed turbines, or $3p$ for three-bladed turbines) fluctuation in electrical power output and to damp drivetrain vibrations, while limiting maximum power to the generator rating.

There are strong similarities in the power-speed-windspeed relationship between vertical-axis wind turbines and stall-regulated horizontal-axis wind turbines. Generator torque control algorithms have been developed for variable-speed, stall-regulated horizontal-axis wind turbines, and it is expected that such algorithms will be directly applicable to vertical-axis designs.

There is no precedent for a stall-regulated floating offshore wind turbine. Active damping of the platform rigid-body modes could be required, depending upon the thrust characteristics of the rotor in stall.

A couple important topics are not yet included in the literature search; for instance, startup and shutdown sequences, emergency stop, and fault conditions (either mechanical or electrical).

2.1 Control of Variable-Speed VAWTs

A series of studies by Hydro-Québec in the mid-1980's provide precedence for variable-speed control of a utility-scale vertical-axis wind turbine. The context for the research was a wind turbine supplying up to 33% of the capacity of a small, isolated grid; therefore power quality was of primary importance. Lefebvre et al. [5] and Dessaint et al. [6] demonstrated that a synchronous generator with an ac-dc-ac power converter can be used to isolate the electrical power output from $2p$ fluctuations in the aerodynamic torque. Nakra and Dubé [7] later extended the investigation to include induction generators.

Dessaint et al. [6] give a detailed description of the controller. The idea is to make the generator torsional stiffness very low. While a fixed-speed synchronous generator has a high torsional stiffness, this can be made arbitrarily low by controlling the grid-side converter firing angle in a way which mimics a soft torsional spring. The firing angle governs the average output voltage in the dc link, and thereby the dc link current and generator torque (cf. Sections 6.1.3 and 6.1.7). An induction generator has a low stiffness, but nonetheless transmits fluctuations in rotor speed to the electrical output; by contrast, active frequency control allows the speed to fluctuate independently of the electrical power. Note that either a synchronous or an induction generator could be controlled in this manner. The transfer function between aerodynamic and generator torque is then dominated by the rotor inertia, rather than drivetrain stiffness, and thus it does not respond significantly to the $2p$ frequency.

Dessaint et al. found that moving the first mode of drivetrain torsional vibration to a low frequency did not eliminate resonance. The resonant response was damped by applying an adjustment to the speed set-point. A derivative control block, filtered to contain only frequencies in the immediate vicinity of the resonant frequency, was applied to the measured firing angle of the network-side converter.

Similarly, moving the first drivetrain mode did not influence the second torsional mode (the first torsional mode of the rotor). This mode was also damped by adjusting the speed set-point according to a derivative control block with a frequency filter. Here the control input was torque on the low-speed shaft. This is not a typical control input on modern wind turbines. See for instance, Hau [8] Chapter 10. Acceleration of the low-speed shaft might be an equivalent signal that is available from typical sensors.

Dessaint et al. do not describe how the speed set-point was determined. Lefebvre et al. used a power set-point, from which the speed set-point was determined via proportional control with a low-pass filter. The power



set-point was truncated to a maximum value based upon a time-averaged measurement of the windspeed.

Ralph [9] studied variable-speed operation of the Sandia 34 m Darrieus VAWT. Based upon a P - Ω - V_∞ (power, rotational speed, and mean remote windspeed) map measured on the turbine, an operating schedule was defined, specifying a desired Ω as a function of a measured estimate of V_∞ . The windspeed was measured by two anemometers located 5 rotor diameters upwind of the turbine. The highest value between the two was taken as the estimated windspeed. A moving average was computed using a period of 200 seconds, and the average was updated every 20 seconds. The desired rotational speed was then computed from a look-up table, with the acceleration limited to 0.01 rad/s^2 .

Performance of the controller was very poor, showing large fluctuations in the output power, to the extent that power was drawn intermittently from the grid. This was attributed to the speed regulator being underdamped. It is not entirely clear from the article, but it sounds as though the main control algorithm requests a speed, and then a separate speed regulator attempts to hold the requested speed within $\pm 5\%$.

This type of control system is not representative of modern wind turbines.

One noteworthy thing about the Sandia control algorithm is the Ω - V_∞ schedule (see Ralph [9] Figure 2). This has a variable-speed section below the rated windspeed, increasing so as to follow the maximum C_P , with a maximum speed limit that is held (almost) constant through the cut-out windspeed. This type of operating schedule is expected to be appropriate for the Deepwind turbine, not considering damping of platform motion.

2.2 Torque Control of HAWTs Below the Rated Windspeed

Below the rated windspeed, it is desired that the rotor operates as to maximize energy capture. At any point in time, the power coefficient C_P should be maximized. On the basis of quasi-steady calculations, the criterion that C_P is maximum corresponds to a single curve in T_G - Ω space, where T_G is the generator torque and Ω is the rotational speed of the rotor. In the case of a two-bladed VAWT, with a torque that pulsates as a function of rotor azimuth angle, T_G is the revolution-average generator torque. An acceptable control strategy is thus to specify the generator torque as a function of the measured rotational speed. cf. Leithead and Connor [10], Jonkman [11]. More complicated control algorithms can provide marginally better energy capture [12].

2.3 Torque Control of Fixed-Pitch HAWTs Above the Rated Windspeed

There are several published examples of generator torque control algorithms used to govern the rotational speed and power output of fixed-pitch turbines in stall.

Thiringer and Linders [13] provide an early example. Here the electrical power and rotational speed were measured. The rate of change of rotational speed was used to estimate the acceleration of the rotor. The aerodynamic power was calculated as the sum of the electric power and the power associated with rotor acceleration. The goal of the control system was to hold the aerodynamic power equal to a chosen reference value.

The reference power was determined on the basis of the measured rotational speed and electric power, together with the computed quasi-steady power-speed characteristics of the turbine. Specifically, the electric power and drivetrain efficiency were used to estimate the aerodynamic power¹, then the quasi-steady P - Ω - V_∞ map was used to estimate the instantaneous value of V_∞ . Knowing V_∞ and Ω , the operating schedule gives the desired, reference aerodynamic power.

The operating schedule chosen by Thiringer and Linders is shown in the left plot of Figure 3. This operating schedule consists of three regimes. In the first, at low windspeeds, the rotational speed is selected so as to maximize the power output. Just below the rated windspeed, the rotational speed is limited to a maximum value. Above the rated windspeed, the rotational speed varies such that the average power output is equal to the rated power.

¹It would seem that this estimate of aerodynamic power does not consider inertial effects of the rotor.

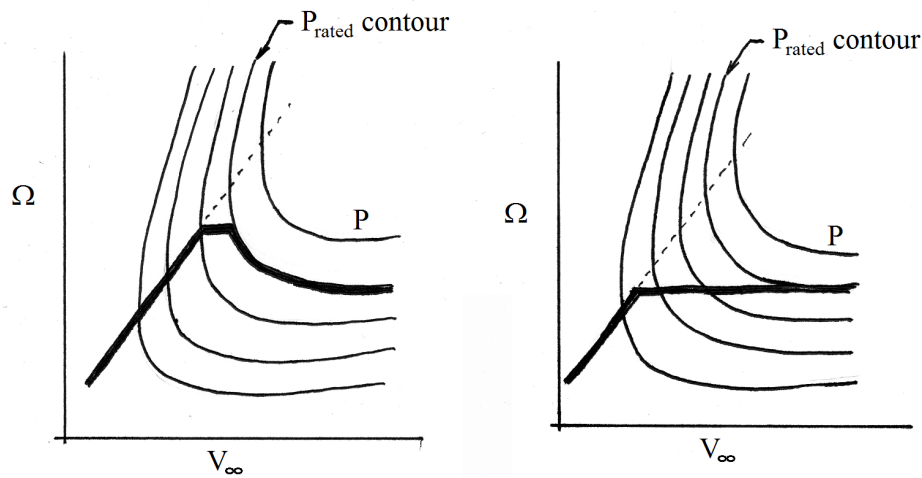


Figure 3: The operating schedule chosen by Thiringer and Linders (left), compared with a simple speed cutoff, like Muljadi et al. (right).

In experiments on a small (20 kW) wind turbine, Thiringer and Linders noted that when the turbine was operating at its maximum rotational speed (just below the rated windspeed), wind gusts caused large peaks in power exceeding the nominal 20 kW rating. That this would occur is obvious from the P - Ω - V_∞ map.

More recently, Muljadi et al. [14] describe a somewhat simpler approach, where the reference power is calculated as a unique function of the rotational speed. In other words, Muljadi et al. applied a low, conservative cutoff in the rotational speed. Contrast this with Thiringer and Linders, who set the speed cutoff higher; but then they had to brake the rotor above the rated windspeed. The operating schedule of Muljadi et al. is shown in the right plot of Figure 3. This is basically the same as the operating schedule implemented by Ralph, although Muljadi et al. showed that such a control strategy could be implemented successfully.

These sorts of issues in selecting the operating schedule of the turbine were reviewed in detail during the ICORASS design study. Bulder et al. [15] document this design study, including a chapter on the control system. Bang et al. [16] also discuss the control system. The goal of the ICORASS study was the conceptual design of an offshore, two-bladed, stall-regulated, horizontal-axis wind turbine. Several control strategies were investigated, including operating schedules like those shown in Figure 3. It was concluded that implementing a rotational-speed cutoff, like that shown on the right in Figure 3, resulted in a very high rated windspeed (20 m/s) and an annual energy capture of only 80% of that obtained by a pitch-regulated turbine. A rotational-speed cutoff was therefore discarded as a realistic option. Several strategies were investigated for dealing with the possible overpower during gusts, when using an operating schedule like the left plot of Figure 3. Here the options are basically to forecast gusts by measuring the wind well upstream (several tens of seconds) from the turbine, and correcting the speed ahead of time, or else to use an oversized generator which can handle the gusts.

The doctoral thesis by Merz [17] dealt with the design of rotors for fixed-pitch, stall-regulated, horizontal-axis wind turbines. Here it was shown that the reason that Bulder et al. found a rotational-speed cutoff to be unacceptable was that the rotor was optimized for aerodynamic efficiency below the rated windspeed, rather than for stall behavior above the rated windspeed.

It is emphasized that it is possible to design a fixed-pitch, stall-regulated rotor such that good aerodynamic characteristics are obtained using an operating schedule that employs a rotational-speed cutoff. However, *this stall behavior must be designed into the rotor from the start*. It follows from a carefully set-up optimization, in which a realistic cost model is used to balance the aerodynamic efficiency, both below and above the rated windspeed, against structural loads and generator rating.

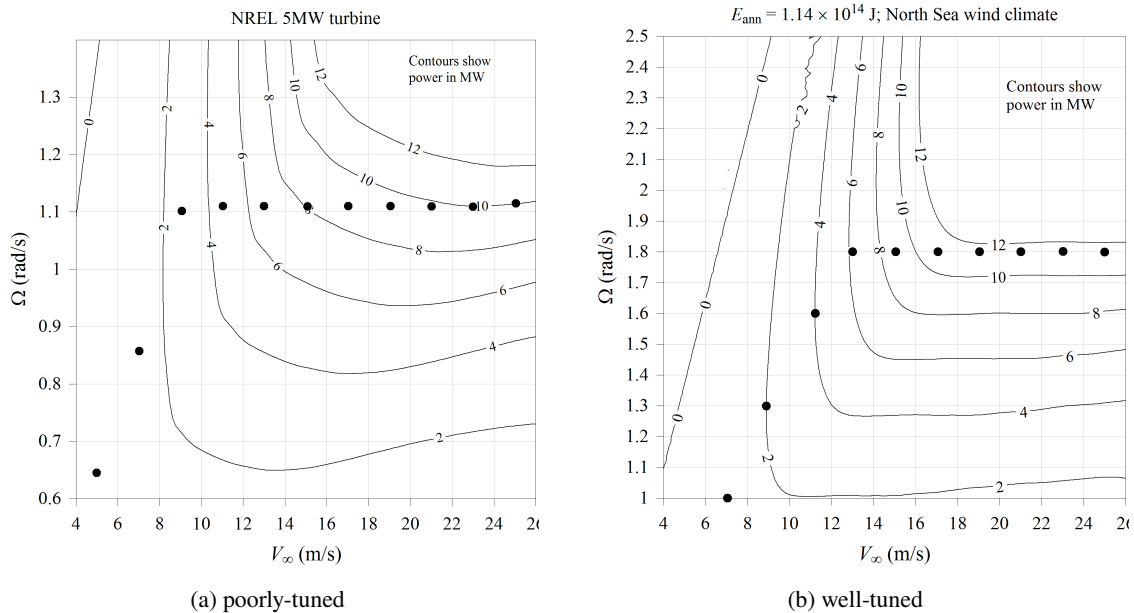


Figure 4: A comparison of operating schedules between a blade that has been optimized for maximum aerodynamic efficiency, and an optimal stall-regulated blade of a similar size

Figure 4 illustrates the difference in behavior between a poorly-tuned and well-tuned rotor. The plot to the left shows a rotor that was designed for maximum aerodynamic efficiency below the rated windspeed. This clearly shows a large loss in power, in the range $13 \text{ m/s} < V_\infty < 20 \text{ m/s}$, when operated with a rotational-speed cutoff. By contrast, the plot to the right shows a rotor that was designed and optimized according to a minimum overall cost-of-energy function. (The cost model is described in Merz [17] Chapter 4.) Here losses are limited to the range $16 \text{ m/s} < V_\infty < 18 \text{ m/s}$.

It should be noted that, despite their historical significance, the aerodynamic design of stall-regulated wind turbines is not a well-developed field. We were not able to find precedence in the literature describing a well-designed variable-speed rotor, with behavior like the right plot of Figure 4. The emphasis on aerodynamic design has traditionally been on maximizing C_P at a design windspeed (below the rated windspeed), and then adjusting the design to provide acceptable stall properties, see e.g. Petersen et al. [18].

The optimal pitch-regulated blade is close to a design with maximum aerodynamic efficiency. Because the majority of publications on blade design over the last 10 years have focused on pitch-regulated turbines, the state of the art in the design of stall-regulated blades has not progressed significantly during this time.

Historically, issues of power quality have been decisive in the utilities' preference of variable-speed, pitch-regulated turbines over constant-speed pitch- or stall-regulated turbines.² It is not possible to design a fixed-pitch turbine (without some alternative method of active aerodynamic control) whose power output is insensitive to gusts. This is especially true for variable-speed, stall-regulated turbines, where power fluctuations are associated with the control action, varying the generator torque. By contrast, above the rated windspeed, a pitch-regulated variable speed turbine can isolate the generator from gusts by initially absorbing the excess energy in the rotational speed of the rotor, and then pitching the blades to compensate.

It is expected that the above discussion of fixed-pitch horizontal-axis wind turbines will also apply to vertical-axis wind turbines: despite significant differences between vertical- and horizontal-axis wind turbines, there are

²Peter Fuglsang, personal communication

close parallels in the P - Ω - V_∞ map, generator control algorithm, and choice of operating schedule.

2.4 Control of Pitch-Regulated Floating Wind Turbines

Recently, blade pitch control algorithms have been developed for floating wind turbines.

Larsen and Hanson [19] describe a stability problem with typical land-based pitch control algorithms, if these are implemented directly on a floating platform. Above the rated windspeed, when blade pitch control is active, the quasi-steady relationship of thrust with respect to windspeed has a negative slope. Considering the slow surge and pitch displacements of the platform as fluctuations in the windspeed, the aerodynamic damping of these modes is negative; the blade pitch action tends to destabilize the platform motion.

One solution to this problem has been described in a patent by Nielsen et al. [4], where a stabilizer is added to the pitch controller that essentially adds an anti-phase contribution to the pitch set-point for frequencies in the tower eigenfrequency region. The effect of this contribution is that the negative damping described above is avoided.

Another solution to this stability problem is presented by Larsen and Hanson: slow the characteristic response time of the controller such that its frequency lies below that of the platform motion. This makes the effective aerodynamic damping positive. However, the slow blade pitch response means that the rotor is more sensitive to low-frequency turbulence and coherent gusts. To avoid rotor overspeed, the generator is controlled with the objective of holding torque constant above the rated windspeed; typically, the objective is to hold output power constant. Constant-torque control results in greater fluctuations in electrical power, in comparison with constant-power control.

Although the gains were tuned differently, the control system architecture used by Larsen and Hanson was typical for onshore turbines. Therefore, it is possible to adapt an onshore controller for use on a floating wind turbine.

Larsen and Hanson did not consider passive-stall rotors. Figure 5 shows a map of the thrust of a sample stall-regulated rotor. (See Merz [17] Section 6.2.4.) Here the slope of the thrust-windspeed curve is not negative (although it can approach zero), and aerodynamic damping remains positive. In theory, it is possible to increase the damping of platform surge and pitch by controlling the rotational speed of the rotor. The idea is shown in Figure 5, and is also described by Lackner [20]. The rotational-speed cutoff can be increased or decreased slightly, with an appropriate phase relative to a given mode of motion, such that the thrust force acts to counter the motion. Note that below the rated windspeed, such damping is automatic, because rotor thrust increases with relative windspeed. It is above the rated windspeed, when thrust is insensitive to the incoming wind, that active damping should be considered.

A problem with active damping is that the output power is directly related to the thrust and rotational speed, therefore active damping will increase the severity of power fluctuations.

Karimirad and Moan [21] employed the method of Larsen and Hanson – slowing the characteristic response time of the controller – to eliminate negative damping of a tension-leg spar type platform. Results were similar, with the slower controller showing a greatly reduced surge and pitch response.

Jonkman [22] also addressed the problem of negative damping of floating, pitch-regulated wind turbines. Pitch oscillation of a barge was studied.³ The method of Larsen and Hanson was employed, decreasing the characteristic frequency of the control system. It was verified that this reduced the platform pitch response, in comparison with a typical onshore controller.

Jonkman also attempted to increase platform pitch damping by employing active control based upon measured tower-top acceleration. (This is an established technique for damping of tower fore-aft modes of onshore

³The design of the barge was very poor, with a pitch natural frequency of 0.086 Hz, in the range of wave frequencies. Jonkman concluded that the various control strategies were not effective in reducing the barge pitch response; but this may have more to do with the barge design than the control strategies. The conclusions drawn from the study may not be directly applicable to other types of floating wind turbines.

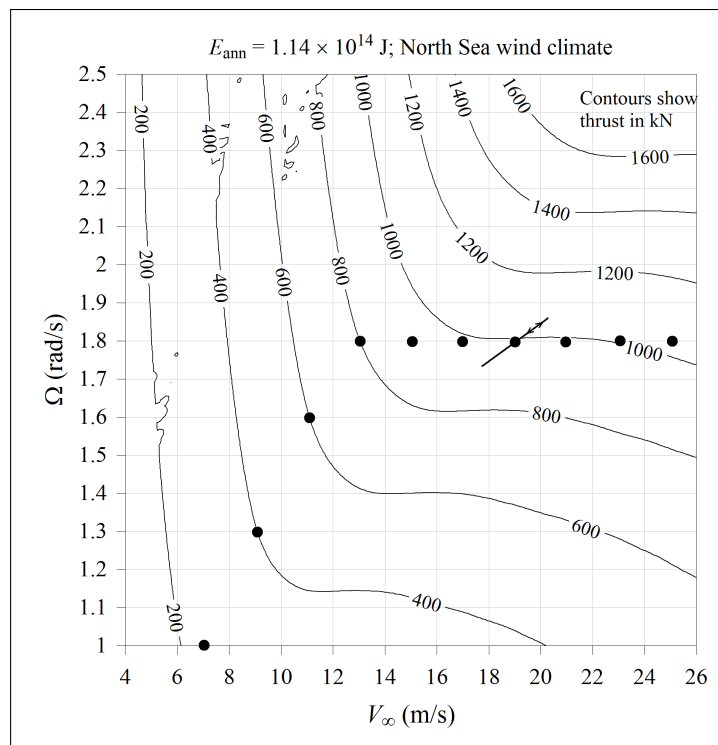


Figure 5: An example of how changing the rotational speed in response to platform pitch and surge motion can be used to increase damping of this motion



wind turbines; Bossanyi [23].) This was found to be ineffective, because the damping and power-regulation control objectives effectively cancel one another: they try to pitch the blades simultaneously in opposite directions. One of the reasons for the interference between damping and power regulation appears to be the proximity of the platform pitch natural frequency and the chosen control system natural frequency: 0.086 Hz and 0.095 Hz, respectively. The ineffectiveness of the tower feedback control seems to be due in part to poor design, rather than a fundamental limitation.

Namik and Stol [24] improved upon Jonkman's controller, showing that the platform pitch motion can be reduced by using a more advanced control algorithm. While Jonkman employed PI control, Namik and Stol used a linear quadratic regulator (LQR), which is based upon a linearized state-space model of the turbine. Optimization is used to determine gains at each of a series of operating points, such that specified control objectives are attained.

Above the rated windspeed, Namik and Stol controlled to constant power, whereas Larsen and Hanson (using a basic PI controller) found it necessary to control to constant torque. LQR control allows for simultaneous objectives of constant power, minimum platform motion, and limited rotor speed variation. The tradeoffs between these are influenced by weights chosen for the performance index, which is used in the optimization.

Individual blade pitch (IBP) control was used to create a restoring moment, in addition to the restoring thrust, which counteracted platform pitch motion. The IBP/LQR controller improved upon the basic PI controller in all the objectives.

The improvement in the control objectives was obtained at the cost of a large increase in blade pitch activity. In other words, the pitch actuators have to work a lot harder (about four times as much) in order to improve the turbine response.

Namik and Stol studied the same barge as Jonkman. Thus it is again necessary to qualify the conclusions; they could be biased by the poor design of the barge. For instance, Namik and Stol report LQR controller performance that is significantly improved over a baseline PI controller, for the case of a barge; but would a similar degree of improvement be obtained for a well-designed spar buoy? A large improvement could be expected in the uniformity of power output above the rated windspeed, but the reduction in platform motion would be much less significant. Indeed, this is demonstrated by the references mentioned below.

Namik and Stol [25] extended their previous study to include a tension-leg platform in addition to the barge, and also added a disturbance-accommodating control (DAC) technique. The DAC was found to have little influence on control objectives. For the tension-leg platform, the IBP/LQR controller provided improved performance with respect to the baseline PI controller; however, the improvement was not as pronounced as for the barge.

Christiansen et al. [26] extended the work of Namik and Stol, employing LQR control on a spar buoy. Control objectives were to minimize platform motion, exceedance of the rated power, and generator overspeed. A moderate improvement (about 20%) was achieved in each of the control objectives, at the cost of highly increased blade pitch activity.

3 Simplified model overview

The aim of the simplified wind turbine model is to be detailed enough to capture the most relevant degrees of freedoms and dynamical characteristics of the wind turbine system, whilst being simple enough to allow fast simulation times. Reasonably fast simulation time is important since the assessment of control strategies will likely involve many simulations to test out different ideas under different conditions and parameter values. The best candidates will subsequently be implemented for validation in full-scale detailed models.

For a comprehensive introduction to land-based vertical axis wind turbines, good starting points are refs. [27, 28].

Schematic drawings of the turbine and coordinate system are shown in Figure 6. The dimensions and other model parameters are given in Table 1.

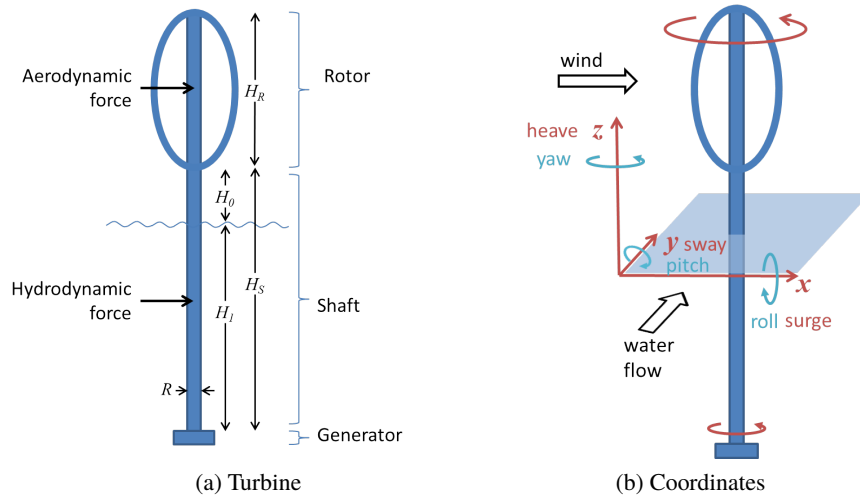


Figure 6: Schematic view of turbine and coordinate system

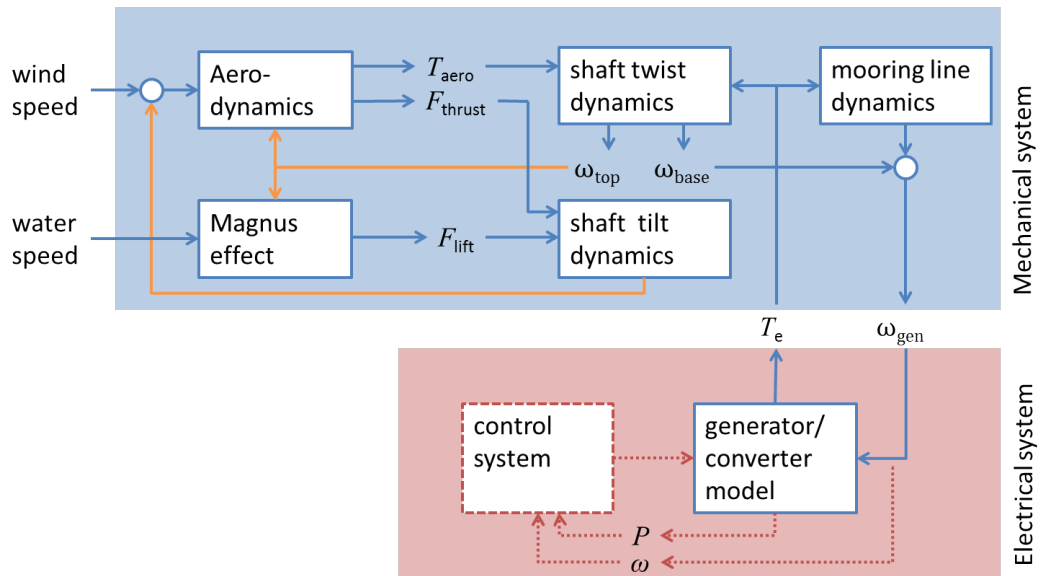


Figure 7: Illustration of simplified model modules and interfaces.



The simplified model consists of different modules representing different degrees of freedom, with links and feedback links coupling them, as indicated in Figure 7. On the highest level, the model is split in a mechanical system and an electrical system, in the same way as the actual turbine would be. The connection between the two systems is the electromagnetic interaction in the air-gap between the generator rotor and stator. This is where the conversion from mechanical energy to electrical energy occurs. The rotor speed ω_{gen} is the input from the mechanical to the electrical system, and the electric counter-torque T_e is the input from the electrical to the mechanical system.

The control system acts on the electrical system, and effectively adjusts the electrical torque in order to obtain the desired rotational speed. Since the DeepWind turbine has no pitch system, additional tasks such as rotor braking also has to be achieved via the electrical system. Generator and converter models with different levels of detail are described later in this report. It is expected that the intermediate model (Section 6.2) is suitable for the development and assessment of control strategies.

The mechanical system consists of 1) an aerodynamic module that computes aerodynamic torque and thrust forces; 2) a hydrodynamic module that computes the Magnus lift force; 3) a module describing the twisting of the shaft around its own axis; 4) a module describing the tilting of the shaft; and 5) a module describing the mooring system dynamics. The general approach has been to model each of these modules in the simplest possible way, whilst maintaining the fundamental properties. In practice, this means formulations in terms of spring-damper models and lookup tables.

3.1 Assumptions and simplifications

The coordinate system is shown in Figure 6b. It is assumed that the wind blows in positive x direction, whereas the direction of the water current can be specified with an angle relative to the x -axis. Both wind and water current are assumed to be horizontal.

The stator side of generator at the bottom of the shaft is assumed fixed in both vertical and horizontal direction, i.e. it has no translational degrees of freedom. However, it is allowed to rotate to a certain degree. It is held in place in the rotational direction by the (torque absorption) mooring system.

Below, the main assumptions and simplifications related to the modelling of each system module is presented. This list is intended as a quick overview only. More details are given in subsequent sections where the modules are described one by one.

Aerodynamics – wind forces acting on Darrieus turbine

- Double-multiple streamtube blade element momentum model, which includes dynamic inflow, dynamic stall and atmospheric turbulence
- Simulations of coupled system is based on lookup tables with coefficients computed using the above model.

Hydrodynamics – water forces acting on rotating shaft

- Magnus lift and friction forces are included
- The tilting of the shaft (and therefore the motion of the shaft itself) is ignored in the derivation of the Magnus forces
- The water current is considered independent of depth
- Wave loads are not presently included. However, if it is deemed necessary for the analyses, waves can readily be added to the model.

Shaft tilting

- The shaft is assumed fixed at the bottom, so that forces acting on the shaft will give rise to a tilt (described by tilt angles in x and y directions). This tilt is represented by a spring–damper in x and y directions
- Displacement of the tilt pivot point is not included – Since the shaft is assumed fixed at the bottom, translational displacement (in horizontal or vertical direction) is not included in the simplified model

Shaft twisting

- The aerodynamic torque acts on the shaft where the shaft meets the Darrieus rotor (see Figure 6a) and the generator gives a torque that acts on the shaft at the bottom. These forces give rise to the rotation as well as a twisting of the shaft. The twist degree of freedom is represented by a 2-body (or 3-body) description of the shaft with a spring–damper coupling

Mooring system

- The stator of the generator is assumed fixed in vertical and horizontal directions, but is free to rotate, and is held in place by mooring lines which are represented by a spring–damper

The simple shaft tilt model and hydrodynamic model (Magnus effect) described above are likely to ignore important natural frequencies in the floating structure. Therefore, an improved representation with 6 degrees of freedom (linear and rotational motion in 3 spatial dimensions) is presently being developed and will likely replace the above model. The new version includes wave loads, which are thought to be important.

As a general note, it should be said that the simplified model described in this report is a good starting point, but it is quite likely that it will have to be modified in order to address issues that may arise when the model is put in actual work. Where modifications are made, these will be documented in a revised version or incorporated in future reports.

Structural parameters used in the model are specified in Table 1. Note that these parameters are initial assumptions only, and are subject to change.

Table 2 show the inertia constants in per units base (see Section 6.1.1). The inertia constant is defined as the rotational kinetic energy for rotation at rated speed divided by the base power rating,

$$H = \frac{\frac{1}{2}J(\omega_n^{\text{mech}})^2}{S_n}, \quad (1)$$

and gives the same information as the rotational inertia J , but in units more suitable for direct analysis in electrical models based on the per unit system. See Section 6.1.1 and e.g. ref. [29] for more details about the per unit base.

3.2 Single degree of freedom spring–damper system

Since both tower and mooring system dynamics are represented by spring–damper models, a brief review of single degree of freedom spring–damper systems is included here as a reminder and to clarify the notation.

The general equation describing a one degree of freedom spring–damper system is the angular version of Newton’s second law:

$$J\ddot{\theta} = T_{\text{ext}} - k\theta - d\dot{\theta}, \quad (2)$$

where θ is the angular displacement, J is the inertia, d is the damping constant, k is the spring constant and T_{ext} is the external torque. Slightly rewritten, this becomes

$$\ddot{\theta} + 2\zeta\omega_0^2\dot{\theta} + \omega_0^2\theta = \frac{1}{J}T_{\text{ext}}, \quad (3)$$

Table 1: Structural parameters (initial values subject to change)

Description	Symbol	Units	2 MW	5 MW	20 MW
Rated rotational speed	ω_{\max}	rad/s	1.6	0.5510	
Geometry					
Total shaft+rotor length	$H_S + H_R$	m	183	253	
Darrieus rotor height	H_R	m	75	130	
Shaft length over water	H_0	m	15	15	
Underwater shaft length	H_1	m	93	108	
Underwater shaft radius	R	m		4.15	
Shaft tilting					
Tilt inertia	J_{tilt}	kg m ²	$5 \cdot 10^8$	$1.97 \cdot 10^{10}$	
Tilt periodicity	T_{tilt}	s	3.7	33.58	
Tilt damping coefficient	ζ_{tilt}	–	0.1	0.1	
Shaft twisting (2-mass)					
Inertia of Darrieus rotor	J_{rotor}	kg m ²	$1.25 \cdot 10^6$	$2.37 \cdot 10^8$	
Inertia of shaft	J_{shaft}	kg m ²	$0.50 \cdot 10^6$	$2.12 \cdot 10^7$	
Inertia of generator rotor	J_{gen}	kg m ²	$0.5 \cdot 10^6$	$0.5 \cdot 10^6$	
Twist periodicity	T_{twist}	s	0.93	1.2	
Twist damping coefficient	ζ_{twist}	–	0.01	0.01	
Shaft spring constant	k	kg/s ²		$1.05 \cdot 10^{10}$	
Shaft damping constant	d	kg/s ²		$1.34 \cdot 10^8$	
Shaft twisting (3-mass)					
Rotor spring constant	k_r	kg/s ²		$1.05 \cdot 10^{10}$	
Rotor damping constant	d_r	kg/s ²		$1.4 \cdot 10^8$	
Shaft spring constant	k_s	kg/s ²		$1.05 \cdot 10^{10}$	
Shaft damping constant	d_s	kg/s ²		$1.4 \cdot 10^8$	
Mooring					
Inertia of generator stator	J_{stator}	kg m ²	$1.0 \cdot 10^5$		
Damping constant	d_{moor}	kg m ² /s	0		
Spring constant	k_{moor}	kg m ² /s ²	$1.0 \cdot 10^6$		

Table 2: Inertia constants in per unit base ($S_n = 5$ MVA)

Tilt inertia	H_{tilt}	600 s
Darrieus rotor twist inertia	H_{rotor}	7.2 s
Shaft twist inertia	H_{shaft}	0.64 s
Generator rotor inertia	H_{gen}	0.015 s



where $\omega_0 = \sqrt{\frac{k}{J}}$ is the undamped natural angular frequency of oscillations (eigenfrequency), and $\zeta = \frac{d}{2J\omega_0}$ is the damping coefficient ($\zeta < 1$ for under-damped systems, and $\zeta > 1$ for over-damped systems).

For an under-damped system, the damped natural (angular) frequency is

$$\omega_d = \omega_0 \sqrt{1 - \zeta^2} \quad (4)$$

The (damped) natural frequency is the system's frequency of unforced oscillations.

If the system is exposed to an external periodic force, it may resonate at a certain frequency called the resonant frequency ω_{peak} ,

$$\omega_{\text{peak}} = \omega_0 \sqrt{1 - 2\zeta^2} \quad (5)$$

For multi-mass (coupled) spring-damper systems, the relationship between spring and damping constants and natural frequencies and damping coefficients is more complicated. In this case, natural frequencies are found by first diagonalising the coupled system of equations.

4 Aerodynamic model

The aerodynamic model governs the dynamics of the wind and rotor blades, and computes torque and thrust forces on the rotor from wind speed and rotational speed input. Two models for the aerodynamics have been developed, one physical model based on a double-multiple streamtube blade element momentum (BEM) method, and a simplified model which includes only the first two terms in a Fourier expansion. These models are described in more detail below.

4.1 Double-multiple streamtube model

A double-multiple streamtube blade element momentum method was implemented as a Fortran program. It is similar to previous methods, such as those described by Paraschivoiu [28], however it includes dynamic inflow. The dynamic inflow calculation was based upon the TUDk model, described by Snel and Schepers [30].

The approach is unique in that it explicitly models many blades about the azimuth of the rotor; a number of fictitious (ghost) blades are modelled, in addition to the real blades. In this manner, the induced velocity is allowed to evolve naturally, according to a dynamic inflow model, while the flow about the blades is also allowed to evolve naturally, according to a dynamic stall model. The rotor therefore responds appropriately to the spatial and frequency distribution of fluctuations in the incoming velocity.

The model calculates the aerodynamic loads on a vertical-axis wind turbine, specifically the torque on the main shaft, which is the force that drives the electromagnetic generator, and the thrust forces that tend to tilt the turbine.

The aerodynamic model is described in more detail in Attachment 1.

4.2 Table-based model

Based on the double-multiple streamtube model described above, look-up tables have been generated that give maps from windspeed (V_∞) and rotational speed (ω) to torque and thrust forces that include 2p and 4p variations, i.e. by postulating that the forces are well represented by the first terms in a Fourier expansion:

$$\begin{aligned} T(\psi) &= T_0 + T_2 \cos(2\psi + \psi_{2p}^T) + T_4 \cos(4\psi + \psi_{4p}^T), \\ F^x(\psi) &= F_0^x + F_2^x \cos(2\psi + \psi_{2p}^x) + F_4^x \cos(4\psi + \psi_{4p}^x), \\ F^y(\psi) &= F_0^y + F_2^y \cos(2\psi + \psi_{2p}^y) + F_4^y \cos(4\psi + \psi_{4p}^y), \end{aligned} \quad (6)$$

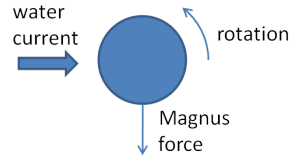


Figure 8: Magnus lift force

where ψ is the angular position of the rotor, i.e. azimuthal angle relative to the wind speed. Assuming that the wind direction is constant (and in x direction), the angular rotor position is the integral of the rotational speed, $\psi = \int \omega dt$. The coefficients $\{T_0, T_2, \psi_{2p}^T, \psi_{4p}^T, F_0^x, F_2^x, \psi_{2p}^x, \psi_{4p}^x, F_0^y, F_2^y, \psi_{2p}^y, \psi_{4p}^y\}$ are specified in the tables for different values of V_∞ and ω .

In the simulation model, 2-dimensional interpolation is used to get these coefficients for any values of V_∞ and ω , which are inputs to the model. Together with ψ , which is also an input, good approximations for torque and thrust forces can then be computed from equations (6).

This simple method is much faster than the full double-multiple streamtube model. It is an approximation that doesn't take into account dynamic inflow, but explicit comparisons of the full model with and without dynamic inflow have shown that the effects are small [31]. It is therefore considered a good model for use in turbine control concept studies.

This approach of approximating the aerodynamic forces by the first terms in a Fourier expansion is similar to techniques for horizontal axis wind turbines, where the dominant aerodynamic force variations due to wind shear and tower shadow occur at $3p$ (for 3-bladed turbine). It may also be convenient to derive an *equivalent* wind speed field $V_{eq}(\psi)$ which depends on the rotor angle ψ and is found by requiring that the aerodynamic power including harmonics be given by the familiar power efficiency (C_p) curve formula for wind power:

$$P = P_0 + P_3 \cos(3\psi) + \dots = \frac{1}{2} \rho A C_p V_{eq}^3. \quad (7)$$

In this form the $3p$ effect and other harmonics are incorporated in the wind field.

5 Floating tower model

The floating tower consists of a rotating (massive) shaft with a rotor mass on the top and a generator mass at the bottom. It is held in place by gravity and buoyancy, and by mooring lines at the bottom.

5.1 Magnus effect

The lift and friction forces are important for the part of the rotating shaft which is under water (rotation in a viscous medium). The lift force, often referred to as the Magnus force, is derived from water current speed and rotational speed of the shaft. See figure 8.

For the computation of the lift force, the tilting of the shaft is ignored, and water current is assumed to be independent of depth. Since the shaft is assumed to be cylindrical with constant radius, the Magnus force is therefore uniform along the length of the underwater shaft. The overall torque around the bottom fixed point of the shaft (i.e. tilt torque) is then

$$T_m = \int_0^{H_1} z f_m dz = \frac{1}{2} H_1^2 f_m, \quad (8)$$

where f_m is the Magnus force per length unit, and H_1 is the length of the underwater part of the rotating shaft.

The Magnus lift force per unit length (of the rotating shaft) can be written in terms of the lift coefficient c_l^m as

$$f_m = c_l^m \frac{1}{2} \rho_{water} U_{water}^2 (2R), \quad (9)$$

where c_l^m is the lift coefficient (see below), $\rho_{water} \approx 1000 \text{kg/m}^3$ is the water density, U_{water} is the water flow speed, and R is the radius of the underwater rotating shaft. The direction of the Magnus force is given by the direction of the vector product $-\vec{\omega} \times \vec{U}_{water}$.

In this equation, it is assumed that the tower fixed in its vertical position. However, the tilt motion of the tower itself can be significant compared to the water current, so this is an approximation that may have to be improved for later detailed analyses.

The lift coefficient for the rotating shaft in the water is approximated according to⁴

$$c_l^m = \begin{cases} 0 & \alpha_m \leq 0.5 \\ -1.15 + 3.67\alpha_m & 0.5 < \alpha_m < 3.15 \\ 10.4 & \alpha_m \geq 3.15 \end{cases} \quad (10)$$

where $\alpha_m = \frac{\omega R}{U_{water}}$.

There is also a friction torque due to drag forces on the rotating shaft. The friction torque per unit length is

$$t_m = c_f^m \rho_{water} \omega^2 R^4, \quad c_f^m = 0.0022, \quad (11)$$

where c_f^m is the friction coefficient. This friction acts as a torque that tends to slow down the rotation of the shaft. Since this friction is relatively small, it has been ignored in the current simplified model (but it can easily be added).

To give a sense of the magnitude of the numbers, for a 5 MW turbine at 10 m/s wind speed and 0.5 m/s water current, the revolution-average aerodynamic thrust force is 0.45 MN, whereas the Magnus lift force is 1.2 MN. In other words, the Magnus force is large, but does not have the same pulsating characteristic as the aerodynamic forces. Its overall effect is to make the turbine tilt in one direction.

5.2 Shaft twisting

Concerning the rotational dynamics, the shaft is represented by a multi-mass spring-damper model. Two versions have been implemented, a 2-mass model where the Darreius rotor is considered as a single mass, and a 3-mass model with a 2-mass representation of the rotor.

The external forces are the aerodynamic torque T_a due to the wind acting on the rotor, and the electromagnetic torque T_e due to the electrical machine acting on the base (generator rotor).

2-mass model In this model, the mass of the shaft itself is split in two, with half at the top and half at the bottom. The top and base inertias are therefore given as

$$J_{\text{top}} = J_{\text{rotor}} + \frac{1}{2} J_{\text{shaft}}, \quad (12)$$

$$J_{\text{base}} = J_{\text{gen}} + \frac{1}{2} J_{\text{shaft}}, \quad (13)$$

where J_{rotor} is the inertia of the rotor part and J_{shaft} is the inertia of the shaft, see Figure 9a. Note that the upper part of the shaft which sits between the attachment points of the blades is considered as a part of the rotor (together with the blades), i.e. it is included in J_{rotor} and not in J_{shaft} . The rotor is considered as a single mass.

⁴Luca Vita, DTU, private communication.

The equations describing the twist dynamics of the shaft is a system of two coupled second order differential equations:

$$T_a - k_{\text{twist}}\phi - d_{\text{twist}}\dot{\phi} = J_{\text{top}}\ddot{\theta}_{\text{top}} \quad (14)$$

$$-T_e + k_{\text{twist}}\phi + d_{\text{twist}}\dot{\phi} = J_{\text{base}}\ddot{\theta}_{\text{base}} \quad (15)$$

where ϕ is the angular displacement of the top relative to the base (twist angle), defined as

$$\phi = \theta_{\text{top}} - \theta_{\text{base}} \quad \Rightarrow \quad \dot{\phi} = \omega_{\text{top}} - \omega_{\text{base}}. \quad (16)$$

The spring constant k and damping constant d are related to the (free floating undamped) natural frequency ω_{twist} and the damping coefficient ζ_{twist} according to

$$d_{\text{twist}} = 2\zeta_{\text{twist}}\omega_{\text{twist}}J_{\text{eff}}; \quad (17)$$

$$k_{\text{twist}} = J_{\text{eff}}\omega_{\text{twist}}^2, \quad (18)$$

$$J_{\text{eff}} = (J_{\text{top}}^{-1} + J_{\text{base}}^{-1})^{-1}. \quad (19)$$

With these definitions, the free floating damped natural frequency becomes $\omega_d = \omega_{\text{twist}}\sqrt{1 - \zeta_{\text{twist}}^2}$ as for a single degree of freedom spring–damper system (Section 3.2).

3-mass model The 3-mass model is illustrated in Figure 9b. The mass is considered lumped together at three points: The bottom of the shaft, the lower attachment point of the blades, and the upper attachment point of the blades. The rotational inertias associated with these three masses are

$$J_{\text{base}} = J_{\text{gen}} + \frac{1}{2}J_{\text{shaft}}, \quad J_{r_1} = \frac{1}{2}J_{\text{shaft}} + \frac{1}{2}J_{\text{rotor}}, \quad J_{r_2} = \frac{1}{2}J_{\text{rotor}}. \quad (20)$$

The coupled system of differential equations describing the system in this case is as follows.

$$\begin{aligned} J_{r_2}\ddot{\theta}_{r_2} &= -k_r\phi_2 - d_r\dot{\phi}_2 + \frac{1}{2}T_a, \\ J_{r_1}\ddot{\theta}_{r_1} &= k_r\phi_2 + d_r\dot{\phi}_2 - k_s\phi_1 - d_s\dot{\phi}_1 + \frac{1}{2}T_a, \\ J_{\text{base}}\ddot{\theta}_{\text{base}} &= k_s\phi_1 + d_s\dot{\phi}_1 - T_e, \end{aligned} \quad (21)$$

where $\phi_1 = \theta_{r_1} - \theta_{\text{base}}$, $\phi_2 = \theta_{r_2} - \theta_{r_1}$, and k_r , d_r , k_s , d_s are the spring and damping constants for the rotor and shaft parts respectively. These spring and damping constant must be tuned to get realistic frequency response characteristics of the system.

5.3 Shaft tilting

Tilting of the shaft refers to rotation around the bottom-fixed point in x (roll) and y (pitch) directions. This dynamics is represented as two independent one-mass spring–damper models. The shaft is assumed bottom-fixed, and two external forces are considered (see Figure 10 and Figure 6a):

- An aerodynamic thrust force acting at the top of the shaft (from wind forces on the rotor blades)
- A hydrodynamic lift force acting on the underwater part of the shaft (Magnus effect due to spin in viscous medium)

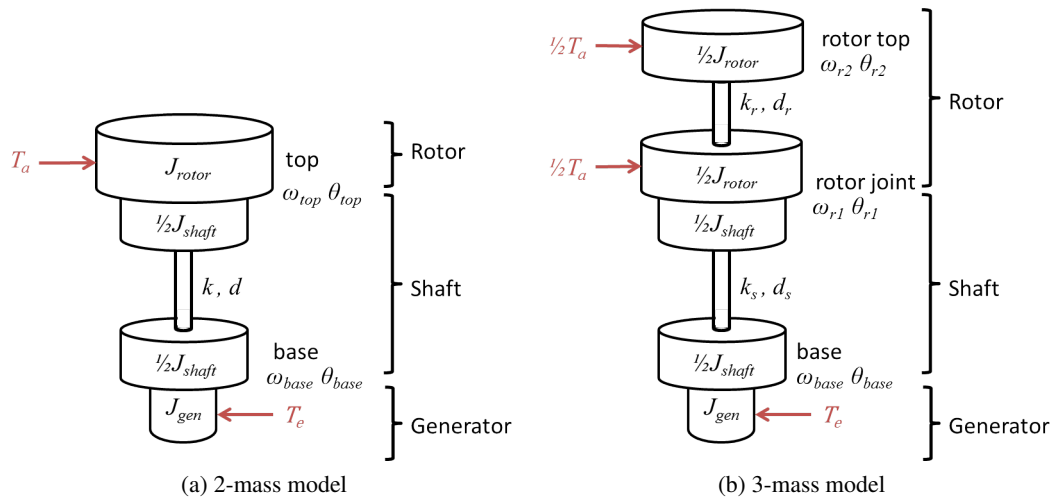


Figure 9: Multi-mass representations for shaft and rotor twist dynamics

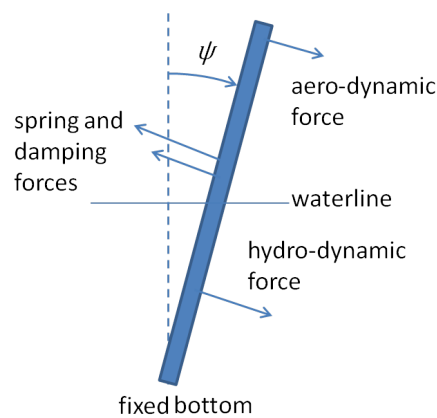


Figure 10: Tilt forces



The equation that describes the tilt dynamics is given in angular form, with torques T and angular displacement ψ from the vertical line:

$$T_{\text{aero}} + T_{\text{hydro}} - k_{\text{tilt}}\psi - d_{\text{tilt}}\dot{\psi} = J_{\text{tilt}}\ddot{\psi}, \quad (22)$$

where J_{tilt} is the tilt inertia, and the spring and damping constants are computed according to

$$k_{\text{tilt}} = J_{\text{tilt}}\omega_{\text{tilt}}^2 \quad (23)$$

$$d_{\text{tilt}} = 2\zeta_{\text{tilt}}\omega_{\text{tilt}}J_{\text{tilt}} \quad (24)$$

The external torques are derived from the aerodynamic thrust force F_a (see Section 4) and the Magnus lift torque (see Section 5.1) and

$$T_{\text{aero}}^x = (H_S + \frac{1}{2}H_R)F_a^x, \quad (25)$$

$$T_{\text{aero}}^y = (H_S + \frac{1}{2}H_R)F_a^y, \quad (26)$$

$$T_{\text{hydro}}^x = \frac{1}{2}H_1^2 f_m \cos(\beta_w), \quad (27)$$

$$T_{\text{hydro}}^y = \frac{1}{2}H_1^2 f_m \sin(\beta_w), \quad (28)$$

where β_w is the angle between the water flow direction and the x axis.

The tilting of the shaft induces motion of the rotor that affects the apparent wind speed.

Gravity, buoyancy and the spring constant The description of the shaft tilting as independent spring–dampers in the x and y directions is valid for small tilt angles and slow motion, as the following considerations show.

A natural choice of coordinates to describe the shaft tilting would be spherical coordinates, using declination (tilt) and azimuth angle to describe the shaft position. This is a suitable choice since it takes advantage of the symmetry of the system. On the other hand, the output (forces) from the aerodynamic model is in Cartesian coordinates (x and y), so a coordinate transformation would then have to be performed to couple these systems.

The spring–damper representation in x and y directions are (cf. eq. (22))

$$\begin{aligned} J\ddot{\psi}_x + d\dot{\psi}_x + k\psi_x &= T_x \\ J\ddot{\psi}_y + d\dot{\psi}_y + k\psi_y &= T_y \end{aligned} \quad (29)$$

Small tilt angles means in spherical coordinates that the shaft is close to the “north pole”. Then the x and y tilt angles ψ_x and ψ_y are small angles along the 0-meridian and along the 90°-meridian respectively. In terms of spherical coordinates, i.e. declination θ and azimuth angle ϕ , we can write (if θ is small)

$$R\psi_x = R\theta \cos \phi \quad (30)$$

$$R\psi_y = R\theta \sin \phi, \quad (31)$$

where the length of the shaft, R drops out of the equation. Inserting these expressions into the equations (29), and assuming slow motions such that quadratic expressions in derivatives can be dropped ($(\frac{d\phi}{dt})^2 \approx 0$ and $\frac{d\phi}{dt} \frac{d\theta}{dt} \approx 0$), gives

$$\begin{aligned} J\ddot{\theta} + d\dot{\theta} + k\theta &= T_x \cos \phi + T_y \sin \phi, \\ J\ddot{\phi} + d\dot{\phi} &= \frac{1}{\theta}(-T_x \sin \phi + T_y \cos \phi). \end{aligned} \quad (32)$$

As expected, there is no spring term in the azimuth direction. In spherical coordinates it is furthermore clear that the spring term stems from the combined torque from gravity (G) and buoyancy (B), that are approximately

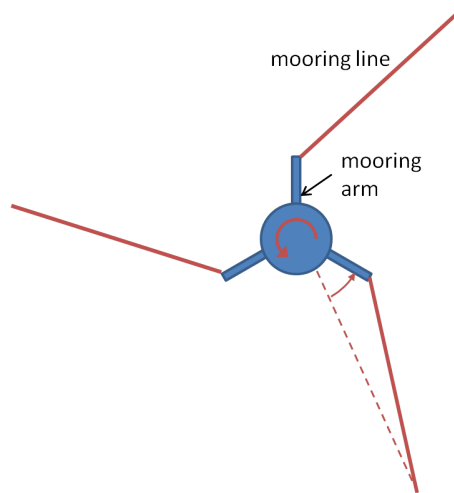


Figure 11: Mooring system

equal, $B \approx G$. Hence the spring constant k can be computed by considering the tilt torque from gravity and buoyancy as follows:

$$\begin{aligned} R_g G \sin \theta - R_b B \sin \theta &\approx (R_b - R_g) G \theta \stackrel{!}{=} -k\theta \\ \Rightarrow k &= (R_b - R_g) G, \end{aligned} \quad (33)$$

where R_b and R_g is the distance from the bottom-fixed point to the centre of buoyancy and centre of gravity respectively. As long as the centre of buoyancy is above the centre of gravity, the spring constant is positive, indicating a stabilising force.

5.4 Mooring system

The mooring system is modelled as a pure torque absorption system represented by a one degree of freedom spring-damper. This means that the stator part of the generator is assumed fixed in translational directions, but is allowed to rotate. The mooring system torque T_{moor} is then expressed

$$T_{\text{moor}} = -d_{\text{moor}} \dot{\theta}_{\text{moor}} - k_{\text{moor}} \theta_{\text{moor}}, \quad (34)$$

where θ_{moor} is the angular displacement of the stator, k_{moor} is the spring constant, and d_{moor} is the damping constant.

The stator rotational dynamics is thus described by the following equation

$$J_{\text{stator}} \ddot{\theta}_{\text{moor}} + d_{\text{moor}} \dot{\theta}_{\text{moor}} + k_{\text{moor}} \theta_{\text{moor}} = T_e, \quad (35)$$

where J_{stator} is the inertia of the generator stator, and T_e is the external torque acting on the stator, which is identical to the electrical counter-torque.

A simplified illustration of how the mooring system may be realised using mooring arms and mooring lines is illustrated in Figure 11.

6 Electrical model

The electrical system consists of the generator at the bottom of the shaft and everything between the generator and the (strong) grid connection point, including converter, transformer and connection cable.

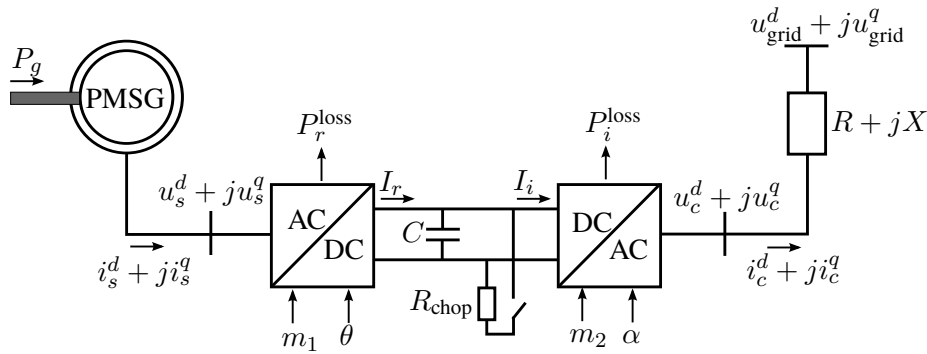


Figure 12: Schematic of electrical system

Table 3: Symbols used in description of electrical system

Symbol	Definition
$i_s = i_s^d + ji_s^q$	stator current
$u_s = u_s^d + ju_s^q$	stator voltage
$i_c = i_c^d + ji_c^q$	grid side converter output (clamp) current
$u_c = u_c^d + ju_c^q$	grid side converter output (clamp) voltage
$u_{grid} = u_{grid}^d + ju_{grid}^q$	external grid voltage
I_r	DC current out of generator side converter (rectifier)
I_i	DC current into grid side converter (inverter)
U_{dc}	DC link voltage
m_1	generator side converter modulation index
θ	generator side converter phase angle reference
m_2	grid side converter modulation index
α	grid side converter phase angle reference
C	DC link capacitance
R_{chop}	DC chopper resistance
P_r^{loss}	generator side converter (rectifier) loss
P_i^{loss}	grid side converter (inverter) loss
$R + jX$	grid impedance

6.1 Detailed model – PMSG with full converter

This model consists of a direct-drive permanent magnet synchronous generator (PMSG) connected via a full scale back-to-back frequency converter to a stiff electrical grid. The model is illustrated in Figure 12. Symbols used are defined in Table 3. Turbine operational control is acheived through the control variables of the power converters, which are both represented as pulse width modulation (PWM) converters. The control variables are therefore the modulation index and the phase angle.

6.1.1 Per unit system and dq0 transformation

The electrical system is described using the *per unit* system, making it easy to adapt to different power ratings. In the per unit system, quantities are expressed relative to a chosen base quantity, thus making them dimensionless. The base quantities are usually related to rated values of the equipment, and must be consistent with each other.

The per unit base power is the generator (apparent) power rating and is denoted S_n . The per unit base rotational speed is denoted $\omega_n = \frac{p_f}{2}\omega_n^{mech}$, where p_f is the number of poles in the generator and ω_m^{mech} is the

Table 4: Generator parameters

Parameter	Value (pu)	Description
ω_n	295	Rated generator electrical angular frequency
r_s	0.02	Armature resistance
x^d	0.5	d -axis reactance
x^q	0.5	q -axis reactance
ψ_m	1	PM rotor flux linkage

nominal (base) mechanical rotational speed. (Since rotational speed has physical units s^{-1} , defining a per unit base implies a per unit time $t_{pu} = \omega_n t$ which is different from physical time t . However, we will express all equations using physical time, and instead insert the factor ω_n if necessary.)

The base torque is determined by the relationship between torque, power and rotational speed, $T = \omega P$, giving $T_{base} = \omega_n^{mech} S_n$.

The description of the electrical system is done using the $dq0$ transformation from a 3-phase formulation to a 2-axis formulation in a rotating reference frame. The two axes are the direct axis (d -axis), which points in the same direction as the permanent magnet's north pole, and the quadrupole axis (q -axis), which is 90° ahead of the d -axis (in electrical degrees). The 0-components will not be relevant in our analyses.

This transformation factors out the sinusoidal content of the 3-phase currents and voltages such that all equations are expressed in terms of dq -phasors that in steady state conditions are constants, e.g. $i = i_0 e^{j\phi} = i^d + j i^q$. Note that in this document, dq coordinates are denoted by an upper index, whereas lower indices denote which part of the system the given quantity refers to, e.g. 's' for stator.

6.1.2 Permanent magnet synchronous generator

This model of a permanent magnet synchronous generator (PMSG) does not include transients due to stator flux, damper windings and magnetic saturations, which are considered of little importance for our studies. The model parameters are given in Table 4.

The PMSG equations are given in dq -coordinates, which is a standard and suitable choice for electrical machines. The stator voltage equations are (cf. equation (3.83) in ref. [29])⁵

$$\begin{aligned} u_s^d &= -r_s i_s^d + \frac{1}{\omega_n} \frac{d\psi^d}{dt} - \omega_r \psi^q, \\ u_s^q &= -r_s i_s^q + \frac{1}{\omega_n} \frac{d\psi^q}{dt} + \omega_r \psi^d, \end{aligned} \quad (36)$$

where r_s is armature resistance, ω_n is the base electrical angular frequency of the generator, ω_r is the per unit rotational speed, and u_s and i_s are stator voltages and currents respectively. The quantities ψ^d and ψ^q are flux linkages, given by

$$\begin{aligned} \psi^d &= -x^d i_s^d + \psi_m, \\ \psi^q &= -x^q i_s^q, \end{aligned} \quad (37)$$

where $x^{d,q}$ is d - and q -axis reactance and ψ_m is permanent magnet (PM) rotor linkage flux. Combined, these equations can be rearranged to give the following system of first order differential equations:

$$\begin{aligned} \frac{di_s^d}{dt} &= -\frac{\omega_n}{x^d} \left(u_s^d + r_s i_s^d - \omega_r x^q i_s^q \right) \\ \frac{di_s^q}{dt} &= -\frac{\omega_n}{x^q} \left(u_s^q + r_s i_s^q + \omega_r (x^d i_s^d - \psi_m) \right) \end{aligned} \quad (38)$$

⁵Note that the flux linkage ψ is often defined with the opposite sign to what is used here

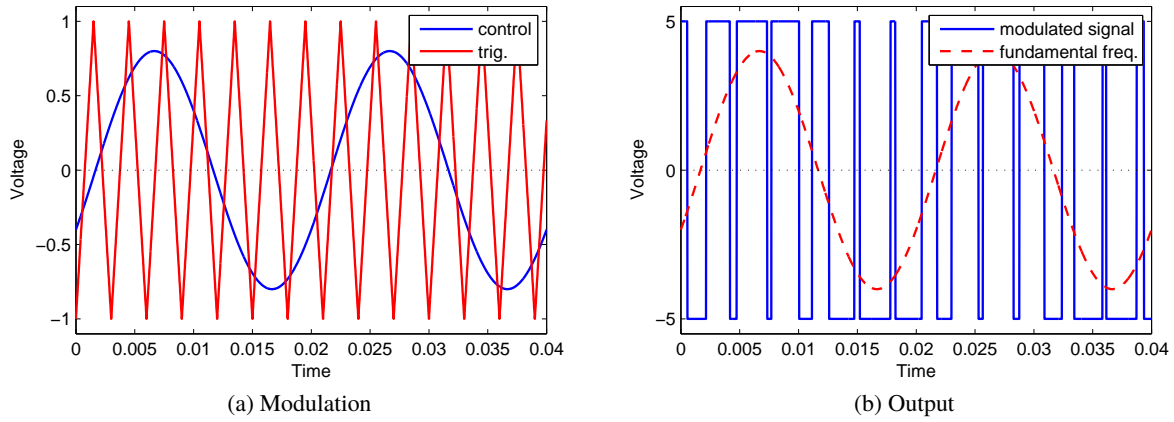


Figure 13: PWM converter principle, modulation signals (a), and output signal (b).

In steady state conditions, time derivatives are zero, and the above equations become explicit expressions for i_s^d and i_s^q :

$$\begin{aligned} i_s^d &= -\frac{\omega_r x^q (u_s^q - \omega_r \psi_m) + r_s u_s^d}{r_s^2 + \omega_r^2 x_s^d x_s^q}, \\ i_s^q &= \frac{u_s^d + r_s i_s^d}{\omega_r x^q} = -\frac{\omega_r (-u_s^d x^d - \omega_r \psi_m) + r_s u_s^q}{r_s^2 + \omega_r^2 x_s^d x_s^q}. \end{aligned} \quad (39)$$

The electrical torque m_e is computed according to the following equation (cf. equation (3.117) in ref. [29]).

$$m_e = \psi^d i_s^q - \psi^q i_s^d. \quad (40)$$

The stator current equations (38) depend on the stator voltages, which again depend on the currents (36). In other words, these equations form part of a coupled system of equations.

The apparent power output from the generator is given by the complex equation $S_s = u_s i_s^*$, which gives the following expressions for active and reactive power flow into the generator side converter:

$$\begin{aligned} P_s &= u_s^d i_s^d + u_s^q i_s^q, \\ Q_s &= u_s^q i_s^d - u_s^d i_s^q. \end{aligned} \quad (41)$$

6.1.3 Converters

Both the generator side and the grid side converters are thought of as pulse width modulation (PWM) converters. Simply put, these convert between AC and DC signals by rapidly opening and closing paths in a circuit. The on/off switching schedule is determined by a signal that alternate between two values representing on and off. This signal is generated by pulse width modulation, typically using a comparison between a fixed triangle signal (v_{trig}) whose period equals the switching period, and a sinusoidal control signal (v_{control}) whose amplitude and phase are the controllable parameters, see Figure 13. The output is +1 if $v_{\text{control}} > v_{\text{trig}}$ and -1 if $v_{\text{control}} < v_{\text{trig}}$. The *modulation index* is defined as the amplitude of the control signal relative to the amplitude of the triangle signal, and the *phase angle* is the phase shift relative to a given reference (e.g. grid voltage or rotor angle).

For our purposes, the fast switching dynamics in the converters can be ignored, such that only the fundamental frequency component of the AC signal is taken into account. A time delay (t_v) of half the switching period is added to represent the reaction time of the converter, since this is the average time it takes before

Table 5: Converter parameters

Parameter	Value (pu)	Description
t_v	0.0001	Time delay (sec)

the switches are next reversed. More information about converters and PWM in general can be found e.g. in ref. [32].

With these assumptions the generator side AC voltage is related to the DC-side voltage by the equations

$$\begin{aligned} u_s^d(t + t_v) &= U_{dc} u_{s,\text{control}}^d, & u_{s,\text{control}}^d &= m_1 \cos(\theta), \\ u_s^q(t + t_v) &= U_{dc} u_{s,\text{control}}^q, & u_{s,\text{control}}^q &= m_1 \sin(\theta), \end{aligned} \quad (42)$$

where m_1 is the modulation index and θ is the phase shift. Similarly, the grid side AC voltage is related to the DC-side voltage by the equations

$$\begin{aligned} u_c^d(t + t_v) &= U_{dc} u_{c,\text{control}}^d, & u_{c,\text{control}}^d &= m_2 \cos(\alpha), \\ u_c^q(t + t_v) &= U_{dc} u_{c,\text{control}}^q, & u_{c,\text{control}}^q &= m_2 \sin(\alpha), \end{aligned} \quad (43)$$

where m_2 is the modulation index and α is the phase shift. The control voltages are determined by the converter controllers, as described later in Sections 6.1.6 and 6.1.7

Parameters for the converter models are specified in Table 5.

6.1.4 DC link dynamics

The DC-link voltage calculation is based on Kirchoff's current law which implies that

$$I_r = I_C + I_{\text{chop}} + I_i, \quad (44)$$

where I_r is the current flowing out of the rectifier, I_C is the current flowing into the capacitor bank, I_{chop} is the current flowing into the DC chopper (resistor), and I_i is the current flowing into the inverter. Since capacitor current is given by $I_C = C \frac{dU_{dc}}{dt}$, this gives

$$\frac{dU_{dc}}{dt} = \frac{1}{C} (I_r - I_i - I_{\text{chop}}), \quad (45)$$

The total power flowing into the converter is equal to the power flowing out plus losses.

The converter DC currents can be written in terms of the power flow, or alternatively in terms of d - and q -axis voltages and currents on the terminals of the generator and grid side converters, cf. equations (41) and (51):

$$\begin{aligned} I_r &= \frac{1}{U_{dc}} (P_s - P_r^{\text{loss}}) = \frac{1}{U_{dc}} (u_s^q i_s^q + u_s^d i_s^d - P_r^{\text{loss}}), \\ I_i &= \frac{1}{U_{dc}} (P_c - P_i^{\text{loss}}) = \frac{1}{U_{dc}} (u_c^q i_c^q + u_c^d i_c^d - P_i^{\text{loss}}), \\ I_{\text{chop}} &= \frac{U_{dc}}{R_{\text{chop}}}, \end{aligned} \quad (46)$$

where R_{chop} is the DC chopper resistance.

Table 6: Grid parameters

Parameter	Value (pu)	Description
R	0.01	External grid resistance
X	0.5	External grid reactance
u_{grid}^d	0	Grid d-axis voltage
u_{grid}^q	1	Grid q-axis voltage

6.1.5 Grid voltage and power

Between the grid side converter and the external grid, there is an impedance which can be thought of as a resistor and an inductor in series. The complex grid voltage is the grid side converter voltage minus the voltage drop over the impedance,

$$\mathbf{u}_{\text{grid}} = \mathbf{u}_c - R\mathbf{i}_c - L\frac{d\mathbf{i}_c}{dt}, \quad (47)$$

where R is the resistance, L is the inductance of the grid connection, and bold face indicate complex quantities in a non-rotating frame. To get the above equation expressed in terms of dq -phasors, we need to expand using d - and q -axis components. $\mathbf{i} = (i^d + ji^q)e^{j\omega t}$, and $\mathbf{u} = (u^d + ju^q)e^{j\omega t}$. The time derivative of the current then becomes

$$\frac{d\mathbf{i}_c}{dt} = \left(\frac{di_c^d}{dt} + j\frac{di_c^q}{dt}\right)e^{j\omega t} + (i_c^d + ji_c^q)(j\omega)e^{j\omega t}. \quad (48)$$

Inserting this into the above voltage equation, and observing that the $e^{j\omega t}$ factor drops out, we find that that the equation can be written in d - and q -axis components as

$$\begin{aligned} u_{\text{grid}}^d &= u_c^d - Ri_c^d - L\frac{di_c^d}{dt} - \omega Li_c^q, \\ u_{\text{grid}}^q &= u_c^q - Ri_c^q - L\frac{di_c^q}{dt} + \omega Li_c^d. \end{aligned} \quad (49)$$

Given the external grid voltages, the grid side currents are given by the following system of first order differential equations.

$$\begin{aligned} \frac{di_c^d}{dt} &= \frac{1}{L} \left(u_{\text{grid}}^d - u_c^d + Ri_c^d + Xi_c^q \right), \\ \frac{di_c^q}{dt} &= \frac{1}{L} \left(u_{\text{grid}}^q - u_c^q + Ri_c^q - Xi_c^d \right), \end{aligned} \quad (50)$$

where $X = \omega L = 2\pi L$ is the reactance. (Grid frequency is unity in the per unit system.)

The apparent power output from the grid side converter is given by the complex equation $S_c = u_c i_c^*$, which gives the following expressions for active and reactive power exported to the grid:

$$\begin{aligned} P_c &= u_c^d i_c^d + u_c^q i_c^q, \\ Q_c &= u_c^q i_c^d - u_c^d i_c^q. \end{aligned} \quad (51)$$

The external grid is assumed to be a strong grid point with constant voltage and zero phase angle, i.e. $u_d^{\text{grid}} = 0$, $u_q^{\text{grid}} = 1$.

The equations (37,38,40,42,43, 45,46,50) together constitute 15 independent equations that are solved (numerically) for the 15 independent variables $\{u_s^d, u_s^q, i_s^d, i_s^q, \psi_d, \psi_q, m_e, U_{dc}, I_r, I_i, I_{\text{chop}}u_c^d, u_c^q, i_c^d, i_c^q\}$. In addition comes the rotational speed ω_r , which is the input to the electrical model, and all the model parameters that also determine the system's behaviour.

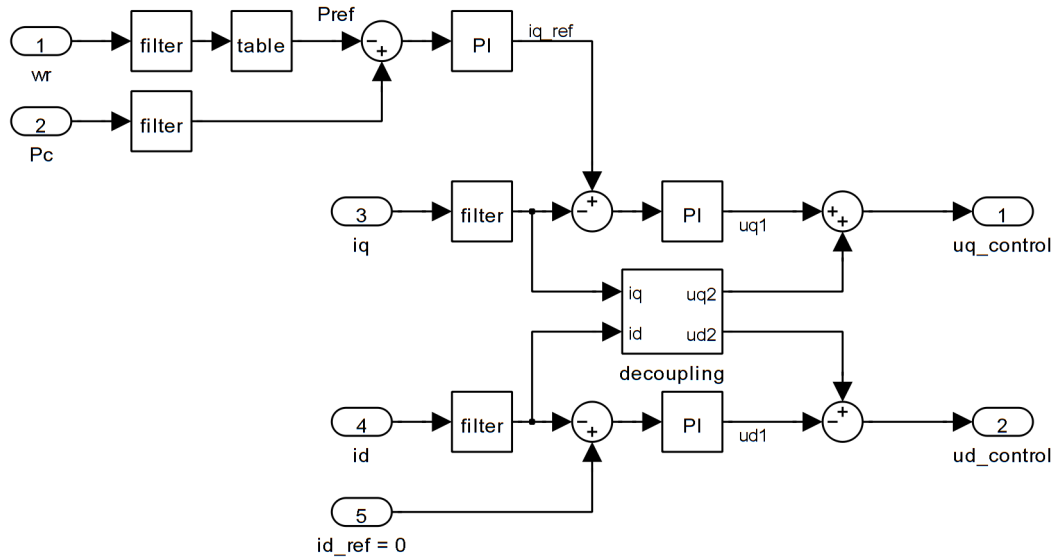


Figure 16: Alternative generator side converter control block diagram

and then $u_{s,2}$ is *chosen* such that it cancels the speed-dependent terms in equation (38), i.e.

$$\begin{aligned} u_{s,2}^d &= -\omega_r \psi^q = \omega_r x^q i_s^q, \\ u_{s,2}^q &= \omega_r \psi^d = -\omega_r (x^d i_s^d - \psi_m). \end{aligned} \quad (52)$$

Then equation (38) separates into two independent equations,

$$\begin{aligned} \frac{di_s^d}{dt} &= -\frac{\omega_n}{x^d} (u_{s,1}^d + r_s i_s^d), \\ \frac{di_s^q}{dt} &= -\frac{\omega_n}{x^q} (u_{s,1}^q + r_s i_s^q). \end{aligned} \quad (53)$$

This means that the d - and q -axis currents can be controlled independently by adjusting the voltages u_s^d and u_s^q respectively. The decoupling circuit is used to derive $u_{s,1} = u_s - u_{s,2}$ based on measured values for u_s and computed/estimated values for $u_{s,2}$.

In order to compute $u_{s,2}$, the controller is dependent on measurements of the currents as well as knowledge of the impedances x^d and x^q and the flux ψ_m generated by the permanent magnets. However, by using PI controllers, errors introduced by minor inaccuracies in these assumed values are compensated for by the integrating controller [33].

A block diagram for a controller using this approach is shown in Figure 16, with feedback logic indicated in Figure 17. This controller regulates the d -axis current to zero, which gives the maximum torque (for a given current), c.f. equation (40). A speed control loop generates the reference q -axis current. The current controller uses the decoupling technique described above to get the converter control signal voltage.

6.1.7 Control – grid side converter

Figure 18 shows block diagrams for a grid side controller that controls DC-link voltage and grid side voltage (indirectly via reactive power). The phase angle parameter (α) controls the DC-link voltage by comparing measured value (U_{dc}) with a constant reference value (U_{dc}^{ref}) and feeding the error signal through a PI-regulator. Similarly, the modulation index parameter (m_2) controls reactive power by comparing measured value (Q_c) with

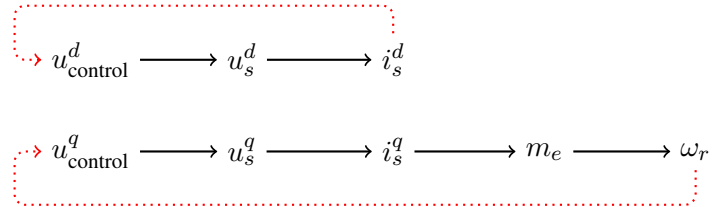


Figure 17: Alternative generator side converter – relationship between measured variable and controller output.

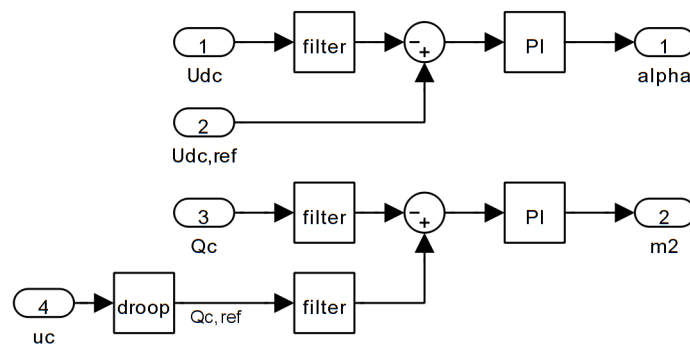


Figure 18: Grid side converter control block diagram

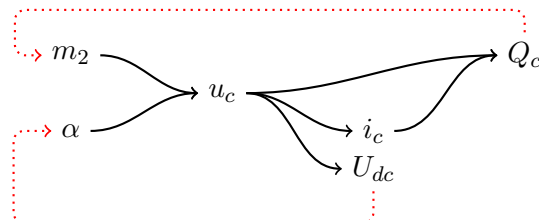


Figure 19: Relationship between measured variable and control output for grid side converter controller

Table 7: Voltage droop control parameters

Parameter	Value (pu)	Description
K_{u_c}	1	Droop function slope
Q_{\max}^{ref}	$0.328P_c$	Reactive power reference upper limit
Q_{\min}^{ref}	$-0.328P_c$	Reactive power reference lower limit

a reference value (Q_c^{ref}) and feeding the error signal through a PI regulator. In this case, however, the reference value is not a constant, but is determined by a *voltage droop* function.

The voltage droop function gives the reactive power reference (Q_c^{ref}) as a function of the grid side converter voltage magnitude $|u_c|$ and a constant voltage reference $|u_c^{\text{ref}}|$. In the present setup, it is assumed that the reactive power should be relatively small, or more specifically, that the *power factor* is limited to $\cos \varphi > 0.95$. The power factor is defined as $\cos \varphi = \frac{P}{S}$, where P is active power and $S = \sqrt{P^2 + Q^2}$ is apparent power. Putting a constant limit on power factor instead of on the reactive power itself, implies that the reactive power will be limited by upper and lower bounds that depend on the active power, since $Q = P \tan \varphi$ and $\cos \varphi > 0.95 \Rightarrow -0.33 < \tan \varphi < 0.33$.

The magnitude of the measured grid side voltage is compared with the reference and the error is multiplied by a proportional gain to generate the desired droop in the reference. The reactive power reference is thus computed according to

$$Q_c^{\text{ref}} = -K_{u_c}(|u_c| - |u_c^{\text{ref}}|), \quad Q_{\min}^{\text{ref}} \leq Q_c^{\text{ref}} \leq Q_{\max}^{\text{ref}} \quad (54)$$

High measured grid voltage magnitude gives negative reactive power reference (that tends to decrease the voltage) and vice versa. The parameters for the droop function is shown in Table 7.

Figure 19 illustrates the relationship between measured/controlled variables (U_{dc}, Q_c) and the converter parameters (α, m_2). Black arrows indicate dependence as described by the system equations, and the dotted red lines indicate controller feedback.

6.2 Intermediate model – Speed control with DC link dynamics

This model is a simplification of the PMSG model above that avoids complex current calculations, and therefore is considerably faster. Essentially, the PMSG and grid side converter are replaced by a simple speed controller, whilst the DC link and grid side converter are kept (almost) as described above.

6.2.1 Speed control (generator and generator side converter)

Instead of including dynamic equations for stator currents and voltages as in the model described above, this model reduced the generator and generator side converter description to a simple speed control algorithm, assuming that the electrical torque equals the electrical torque set-point, $m_e = m_e^{\text{set}}$, and that the power flowing into the DC link equals the electrical torque times the rotational speed, $P_s = \omega_r m_e$. The justification is that the converter dynamics is fast compared to the dynamics of the mechanical system as well as compared to the grid dynamics.

The speed control example shown in Figure 20 is based on a look-up table, that for measured values of rotational speed ω_r gives the associated torque reference value. This value is compared to the torque derived directly from the power P_c and rotational speed, giving an error signal that feeds into a PI regulator to give the electrical torque set-point m_e^{set} . Controller parameters are specified in Table 8.

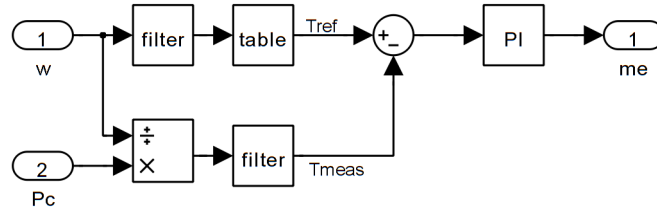


Figure 20: Speed control block diagram – intermediate model

Table 8: Speed control parameters

Parameter	Value (pu)	Description
Kwts	5	Rotor speed filter bandwidth
Kfts	10	Torque filter bandwidth
Kits	3	PI regulator integral gain
Kpts	5	PI regulator proportional gain
Me_max	1	Electrical torque upper limit
Me_min	0	Electrical torque lower limit

6.2.2 Other simplifications

Since this simplified model omits computing stator voltages and currents, the DC link current equation (46) for the current flowing out of the generator side converter must be written in the first form, i.e. in terms of power flow rather than currents and voltages:

$$I_v = \frac{1}{U_{dc}} (P_s - P_s^{\text{loss}}), \quad P_s = \omega_r m_e. \quad (55)$$

It is further assumed that the grid side currents change slowly compared to the DC-link dynamics, such that the time derivatives in equation (50) can be ignored. Setting these to zero, gives the equations

$$\begin{aligned} i_c^d &= \frac{1}{R^2 + X^2} \left(R(u_c^d - u_{\text{grid}}^d) + X(u_c^q - u_{\text{grid}}^q) \right), \\ i_c^q &= \frac{1}{R^2 + X^2} \left(-X(u_c^d - u_{\text{grid}}^d) + R(u_c^q - u_{\text{grid}}^q) \right). \end{aligned} \quad (56)$$

6.3 Basic model – Speed control, no grid representation

This model is a further simplification that also omits the DC link dynamics, assuming that $P_c = P_s$. What is left is therefore the same as the intermediate model described above without any coupling to the electrical system.

Again, the justification is that the dynamics of the electrical system is so much faster than the dynamics of the rest of the system that the electrical torque can be assumed to be equal to the set-point value determined by the control system, and that the power output from the generator is identical to the power flowing into the electrical grid. This is a reasonable assumption when focussing on the mechanical system. But since the electrical system is not included at all, it cannot be used to study system behaviour during e.g. grid faults or other phenomena linked to the interaction between the mechanical and electrical systems.



7 Initial thoughts on control concepts

A brief overview of the control challenges was presented in Section 1.3. This Section follows-up the remarks made there with some initial thoughts on how to design the control system such that it enables best possible operation of the turbine.

The control system for the DeepWind platform can be thought of as performing three functions: first, there is the basic control of the generator torque such that the rotational speed follows the specified operating schedule. This is heavily dependent upon the aerodynamic design of the rotor, and is discussed in Section 7.1. Second, the pulsating aerodynamic torque must be smoothed, such as to minimise fatigue on the mooring system and ensure a reasonably smooth power output. Smooth power output is important on a wind farm level in order to satisfy grid code requirements, but less relevant on turbine level since consorted wind farm control can ensure that variations from individual turbines are smoothed out. The choice of control architecture, discussed in Section 7.2, will influence the degree of load reduction that can be achieved. Third, the fact that DeepWind is a floating platform may add additional tasks for the control system, namely helping to damp the rigid-body motion of the buoy. This is discussed in Section 7.3.

7.1 Aerodynamic Design

The aerodynamic design of the rotor will be decisive in determining whether the control system design task is successful. As Bulder et al. [15] demonstrated, if the turbine has poor stall behavior at a constant rotational speed (like the left plot in Figure 4), then the control designer must choose between two difficult options: attempt to anticipate and correct for gusts ahead of time, or demand an oversized generator. On the other hand, if the turbine has good stall behavior at a constant rotational speed (like the right plot in Figure 4), then the task is straightforward: follow the operating schedule which maximizes energy capture, but constrain the rotational speed to be less than a maximum value. (As described later in this section, the maximum rotational speed may vary on a long timescale, say, several tens of seconds or more.)

Rotor design based upon C_P (aerodynamic efficiency) is misleading, because in calculating C_P the power is normalized by the swept area. But the swept area in itself does not matter, because the wind blows everywhere; the wind is not limited to a specified area.⁶ What matters is the relationship between energy capture, blade loads, and generator rating (and utility grid connection issues, which are lumped in with the generator for the present discussion). Blade loads are associated with the swept area, but not as a 1:1 correspondence. In other words, if two rotors produce the same annual energy, it is possible that the one with the larger swept area (and lower C_P) has lighter blades and less severe loads; this depends upon the details of the blade design. It is also incorrect to compare a Darrieus (VAWT) and propeller-type (HAWT) rotor on the basis of C_P , because the structural design of the blades is very different. Normalizing to a given area does not provide a level comparison.

The DeepWind rotor should be designed on the basis of a cost model that considers the influence of stall behavior on energy production, blade loads, and generator rating. This can be a model like that used in ref. [17], or it can be a more elaborate method, for instance, as in Fuglsang et al. [34], Fuglsang [35], or Hjort [36]. It should be specified up front that the operating schedule employs a rotational-speed cut-off, like that shown at the right of Figures 3 and 4. Minimizing the cost function will then force the blade design to have good stall behavior.

7.2 Controller Architecture

Established control strategies include PID (of varying complexity), linear state-space (like LQR), and more advanced model-predictive algorithms.

⁶That is, C_P matters in the case of a fan or turbine in a closed duct, where the swept area is fixed as an external constraint.



The references of Section 2 demonstrate that a fairly straightforward PID architecture is sufficient to achieve the control objectives to a reasonable degree, provided that the characteristic frequencies (controller, platform, and structure) are well-separated. It is therefore planned to implement the simplest possible PID controller as a baseline. More advanced control algorithms may be investigated as time allows.

DeepWind is a stall-regulated turbine. Without the blade pitch degree-of-freedom, there is a tight coupling between control action – which is limited to generator torque under normal operation – and electrical power output. This indicates that the best control strategy will be one in which the controller acts quite slowly, allowing the energy from disturbances to be stored in and extracted from the rotor rotational speed, rather than being transmitted directly to the generator. The strategy of Dessaint et al. seems especially promising, because it allows for both uniform power output and active damping of drivetrain modes. However, it may be challenging to place the electrically-altered drivetrain natural frequency far enough away from floating platform modes.

It is not known upfront how the Magnus effect (coupling rotational speed with transverse force on the tower) will influence the control system design.

As pointed out above, the large 2p aerodynamic torque variations should not transfer into the generator and mooring system, but instead the turbine should be allowed to speed up and slow down during each revolution allowing the electromagnetic torque to be more or less constant. Because of the large rotational inertia of the turbine, the required speed variations are modest, as the following simple considerations show.

Assume that the electromagnetic torque T_e is constant, and that the turbine speeds up and slows down twice per period. Each speed-up period then lasts one quarter of a period, $\Delta t = \frac{\pi}{2\omega}$. For simplicity, let us approximate the aerodynamic torque T_a as a sinusoidal that varies between zero and twice the average value: $T_a \approx T_e(1 + \sin(2\omega t))$, where the average value equals T_e . The energy absorbed during the speed-up period is given by the integral

$$\Delta E = \omega \int_0^{T/4} (T_a - T_e) dt \approx T_e, \quad (57)$$

where the rotational speed has been approximated as constant in the integration. The absorbed energy is transformed into rotational kinetic energy ($E_k = \frac{1}{2}J\omega^2$), which gives a speed-up

$$\Delta\omega = \frac{\Delta E}{J\omega} = \frac{T_e}{J\omega}. \quad (58)$$

For a turbine with total rotational inertia $J_{\text{rotor}} + J_{\text{shaft}} = 2.6 \cdot 10^8 \text{ kg/m}^2$, rotational speed $\omega = 0.551$ and electromagnetic torque $T_e = 9 \text{ MN}$ (corresponding to average power of 5 MW), the above expression gives $\Delta\omega = 0.06 \text{ rad/s}$. In conclusion, the turbine speed variations required to keep the electromagnetic torque fixed when operating at rated power are about 0.06 rad/s, or about 11% of nominal speed.

7.3 Considerations for a Floating Platform

The floating platform will exhibit two types of responses: resonant and wave-frequency. The resonant response is sensitive to the level of damping, and can be influenced by actively controlling the thrust on the rotor, for instance, by varying the rotational speed by a small amount. The wave-frequency response is inertia-dominated, and is not sensitive to damping. It cannot typically be compensated by control of the rotor. Rather, it can only be influenced by the design of the spar.

In the case of DeepWind, the Magnus effect might provide a small amount of control of the wave-frequency response by varying the rotor rotational speed. But the level of control is unlikely to be large enough to make much of a difference in the response.

Investigations of spar buoy dynamics, such as Karimirad [37], indicate the following: under operating conditions, with a “slow” PI controller as employed by Larsen and Hanson, the pitch motion of the spar is dominated by wave excitation under moderate to severe wave states. The results of Christiansen et al. indicate that there is

$V_\infty = 8 \text{ m/s}$; $I = 0.2$; $\Omega = 0.55 \text{ rad/s}$
 $H_s = 4 \text{ m}$; $T_p = 9 \text{ s}$; $U_c = (0.8, 0.2) \text{ m/s}$; $D_t = 6.3 \text{ m}, 8.3 \text{ m}$
 Airy wave theory; Jonswap wave spectrum (DNV)

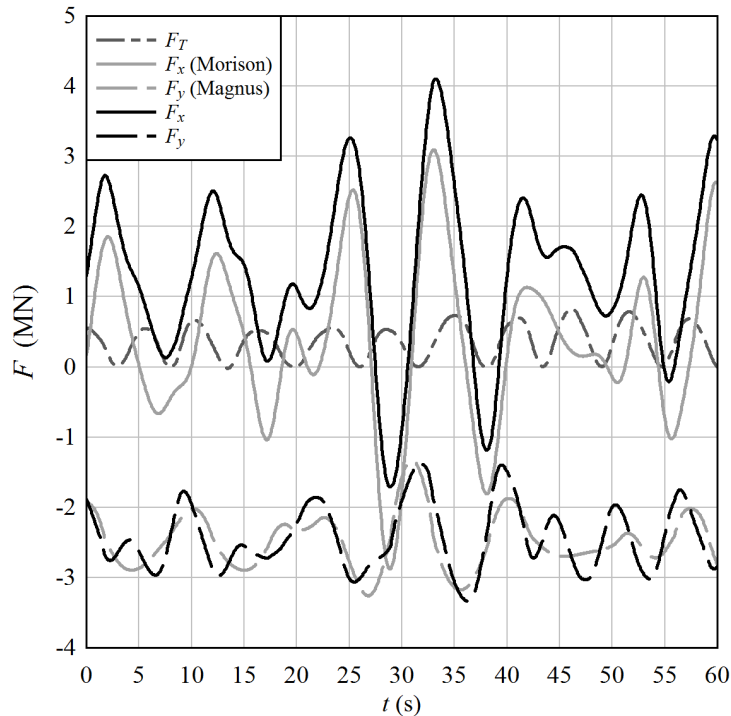


Figure 21: Timeseries of dominant forces acting on the 5 MW DeepWind turbine. The plot shows aerodynamic thrust force (F_T), Hydrodynamic thrust force (Morrison, F_x), hydrodynamic lift force (Magnus, F_y), and sum in x direction (F_x) and y direction (F_y).

a limited potential to reduce the response, by use of a more advanced control algorithm. Under extreme conditions, when the rotor is shut down, the resonant and wave-frequency responses are of comparable severity; but here there is no possibility for aerodynamic control.

It therefore seems natural to pursue a simple PID control algorithm as a baseline.

8 Conclusions

This report has described in detail a simplified numerical model for a floating vertical axis wind turbine which is suitable for the development of control concepts. The model consists of multiple modules, implemented in Matlab/Simulink, with flexibility regarding the level of complexity to be included in any given simulation. The aerodynamics is based on a double-multiple streamtube model implemented in Fortran and coupled with the rest of the system either directly, or indirectly via a set of look-up tables. The tower model consists of spring-damper representations of the most relevant floating tower and mooring system degrees of freedom and a simple representation of the hydrodynamic Magnus effect. The electrical system is modelled based on a permanent magnet synchronous generator with full-scale converter and an impedance to a stiff electric grid.

This model includes the most relevant characteristics and degrees of freedom of the DeepWind turbine, and is considered well suited for analyses of control concepts without involving too time-consuming simulations.

Of the simplifications made, it is thought that the most questionable ones are the omission of waves and the simple representation of the mooring system. As indicated in Figure 21, the variation in the wave forces can be quite significant, although the average value is small compared to the average value of the Magnus lift force.



Hence, an improved model will include wave loads and more advanced hydro/structural/mooring model. Such an improved model has in fact already been implemented, and if it does indeed prove to be necessary for the control concept analyses, it will be documented in a new revision of this document, or in another future report.

The literature review that was presented gives an overview of relevant studies and the current status regarding control of horizontal and vertical axis wind turbines. Finally, some initial thoughts on control strategies were given to indicate the direction of upcoming work.

The next step is to implement a baseline torque control strategy that ensures the turbine operates at maximum aerodynamic efficiency. This should be straightforward, at least in the variable speed range, using the same principles as for horizontal axis turbines. Additional logic must then be added to ensure satisfactory speed limitation and power limitation at high wind speeds, and eventually shut-down at very high wind speeds. This is considered one of the main challenges for the control system (and blade design), as there is no possibility for blade pitching, and the wind speeds can vary a lot on short timescales. Another main challenge, which will also be the focus of initial investigations, is the smoothing of the $2p$ variations in the aerodynamic torque. In principle this can be done by allowing the turbine itself to act as an energy storage through its rotational inertia, absorbing variations in the aerodynamic torque/power by increasing or decreasing the rotational speed. In other words, the pulsating torque can be traded for (a much smaller) pulsating rotational speed. However, it remains to demonstrate this principle in practice.

For these initial analyses it may be sufficient to include only the aerodynamics and the basic torque control, ignoring in the first instance shaft and mooring dynamics and the electrical system altogether. When the control concepts are successful at this level, it makes sense to include additional detail to ensure stability, and show how the controller can be implemented in the electrical system. At a later stage in the project, the coupling to the electrical grid will be studied in more detail, addressing issues of grid code compliance and electrical grid–turbine dynamical interactions.

Subsequent reports will describe alternative control strategies and present simulation results based on the model described in this report.

References

- [1] L. Vita, et al., A novel floating offshore wind turbine concept: New developments, in: EWEC 2010, 2010. URL <http://orbit.dtu.dk/All.external?recid=261913>
- [2] U. Poulsen, et al., Deepwind – an innovative wind turbine concept for offshore, in: EWEA Annual Meeting, 2011.
- [3] Deepwind, accessed 1 Dec 2011. URL <http://www.deepwind.eu>
- [4] F. G. Nielsen, B. Skaare, J. O. G. Tande, I. Norheim, K. Uhlen, Method for damping tower vibrations in a wind turbine installation, patent US20080260514 (2008). URL <http://www.google.com/patents/US20080260514>
- [5] S. Lefebvre, et al., Simulator study of a vertical axis wind turbine generator connected to a small hydro network, IEEE Transactions on Power Apparatus and Systems PAS-104 (1985) 1095–1101.
- [6] L. Dessaint, et al., Propagation and elimination of torque ripple in a wind energy conversion system, IEEE Transactions on Energy Conversion EC-1 (1986) 104–112.
- [7] H. Nakra, B. Dub e, Slip power recovery induction generators for large vertical axis wind turbines, IEEE Transactions on Energy Conversion 3 (4) (1988) 733–737. doi:10.1109/60.9346.



- [8] E. Hau, *Wind Turbines – Fundamentals, Technologies, Application, Economics*, 2nd Edition, Springer-Verlag, Berlin, Germany, 2006.
- [9] M. Ralph, Control of the variable speed generator on the sandia 34-metre vertical axis wind turbine, in: *Windpower '89*, San Francisco, CA, 1989, also in Report SAND90-1615, Sandia National Laboratories, Albuquerque, New Mexico, USA, 1992.
- [10] W. Leithead, B. Connor, Control of variable speed wind turbines: Design task, *International Journal of Control* 73 (13) (2000) 1189–1212.
- [11] J. Jonkman, Dynamics modeling and loads analysis of an offshore floating wind turbine, technical Report NREL/TP-500-41958, National Renewable Energy Laboratory, Golden, CO, USA (2007).
- [12] B. Boukhezzer, et al., Nonlinear control of variable-speed wind turbines for generator torque limiting and power optimization, *Journal of Solar Energy Engineering* 128 (4) (2006) 516–530.
- [13] T. Thiringer, J. Linders, Control by variable rotor speed of a fixed-pitch wind turbine operating in a wide speed range, *IEEE Transactions on Energy Conversion* 8 (3) (1993) 520–526.
- [14] E. Muljadi, et al., Soft stall control for variable-speed stall-regulated wind turbines, *Journal of Wind Engineering and Industrial Aerodynamics* 85 (2000) 277–291.
- [15] B. Bulder, et al., The icorass feasibility study – final report, report ECN-E-07-010, Energy Research Centre of the Netherlands (2007).
- [16] D. Bang, et al., New active speed stall control compared to pitch control for a direct-drive wind turbine, TU Delft; accessed in June 2011 at <http://repository.tudelft.nl/assets/uuid:7fc9247d-8868-4d7f-9a65-b51ccd27f8ea/211573.pdf>.
- [17] K. Merz, Conceptual design of a stall-regulated rotor for a deepwater offshore wind turbine, Ph.D. thesis, NTNU (2011).
- [18] J. Petersen, et al., Prediction of dynamic loads and induced vibrations in stall, Tech. Rep. Risø-R-1045(EN), Risø National Laboratory, Roskilde, Denmark (1998).
- [19] T. Larsen, T. Hanson, A method to avoid negative damped low frequent tower vibrations for a floating, pitch controlled wind turbine, *Journal of Physics: Conference Series* 75 (2007) 012073. doi:10.1088/1742-6596/75/1/012073.
- [20] M. Lackner, Controlling platform motion and reducing blade loads for floating wind turbines, *Wind Engineering* 33 (2009) 541–553. doi:10.1260/0309-524X.33.6.541.
- [21] M. Karimirad, T. Moan, Ameliorating the negative damping in the dynamic responses of a tension leg spar-type support structure with a downwind turbine, presented at the European Wind Energy Conference, Brussels, Belgium, March 14-17 (2011).
- [22] J. Jonkman, Influence of control on the pitch damping of a floating wind turbine, conference Paper NREL/CP-500-42589, National Renewable Energy Laboratory, Golden, CO, USA, 2008; presented at the 2008 ASME Wind Energy Symposium, Reno, NV, USA, January 7-10 (2008).
- [23] E. A. Bossanyi, Wind turbine control for load reduction, *Wind Energy* 6 (3) (2003) 229–244. doi:10.1002/we.95.



- [24] H. Namik, K. Stol, Individual blade pitch control of floating offshore wind turbines, *Wind Energy* 13 (1) (2010) 74–85. doi:10.1002/we.332.
- [25] H. Namik, K. Stol, Performance analysis of individual blade pitch control of offshore wind turbines on two floating platforms, *Mechatronics* 21 (4) (2011) 691–703. doi:10.1016/j.mechatronics.2010.12.003.
- [26] S. Christiansen, T. Knudsen, T. Bak, Optimal control of a ballast-stabilized floating wind turbine, in: *IEEE International Symposium on Computer-Aided Control System Design (CACSD)*, Denver, CO, USA, September 28-30, 2011, pp. 1214–1219. doi:10.1109/CACSD.2011.6044574.
- [27] L. L. Freris (Ed.), *Wind Energy Conversion Systems*, Prentice Hall, 1990.
- [28] I. Paraschivoiu, *Wind Turbine Design, with Emphasis on Darrieus Concept*, Polytechnic International Press, Montréal, Québec, Canada, 2002.
- [29] P. Kundur, *Power System Stability and Control*, McGraw-Hill, 1994.
- [30] H. Snel, J. Schepers, Joint investigation of dynamic inflow effects and implementation of an engineering method, Tech. rep., Energy Research Centre of the Netherlands (1995).
- [31] K. Merz, A method for analysis of VAWT aerodynamic loads under turbulent wind and platform motion, presented at the 9th Deep Sea Offshore Wind R&D Seminar, 19-20 January 2012, Trondheim, Norway.
- [32] N. Mohan, T. M. Undeland, W. P. Robbins, *Power Electronics*, 2nd Edition, John Wiley & Sons, 1995.
- [33] T. P. Fuglseth, Modeling and control of a floating offshore wind turbine, Ph.D. thesis, Norwegian University of Science and Technology (2011).
- [34] P. Fuglsang, et al., Site-specific design optimization of wind turbines, *Wind Energy* 5 (4) (2002) 261–279.
- [35] L. Fuglsang, Integrated design of turbine rotors, in: *European Wind Energy Conference*, Brussels, Belgium, 2008.
- [36] S. Hjort, et al., Fast prototype blade design, *Wind Engineering* 33 (4) (2009) 321–334.
- [37] M. Karimirad, Stochastic dynamic response analysis of spar-type wind turbines with catenary or taut mooring systems, Ph.D. thesis, Norwegian University of Science and Technology (2011).



Technology for a better society
www.sintef.no

Attachment 1

A Blade Element Momentum Method for Dynamic Analysis of Vertical Axis Wind Turbines – Rev B

Karl O. Merz
NTNU, Department of Civil and Transport Engineering
Trondheim, Norway

November 9, 2011

Abstract

A computer program has been developed to calculate the aerodynamic loads on a vertical-axis wind turbine. The program is based upon a double-multiple streamtube blade element momentum method. The approach is unique in that it explicitly models many blades about the azimuth of the rotor; a number of fictitious (ghost) blades are modelled, in addition to the real blades. In this manner, the induced velocity is allowed to evolve naturally, according to a dynamic inflow model, while the flow about the blades is also allowed to evolve naturally, according to a dynamic stall model. The rotor therefore responds appropriately to the spatial and frequency distribution of fluctuations in the incoming velocity.

Contents

1	Introduction	3
1.1	Coordinate Systems	4
1.2	Problem Setup and Required Inputs	6
1.2.1	Discretization of the Blade and Swept Surface	7
1.2.2	Chord, Twist, and Pitch	7
1.2.3	Blade Azimuth Angle	9
1.2.4	Incoming Airflow	9
2	Airfoil Forces	10
2.1	Airfoil Coefficients	10
2.1.1	Airfoil Coefficient Extrapolation	12
2.2	Dynamic Stall	13
2.2.1	Separation Point Motion	15
2.2.2	Implementation of the Øye Method	15
2.2.3	Positive and Negative Angles-of-Attack	17
2.2.4	An Example of Dynamic Stall	18
2.2.5	Changes in Reynolds Number	23
3	Momentum Balance	24
3.1	Momentum Balance Equation	24
3.2	Double-Multiple Streamtube BEM	25
3.3	Correction for Finite Aspect Ratio	26
3.4	Induced Velocity	27
3.5	Dynamic Inflow	29
3.6	Vector Versus X^r Momentum Balance	31
4	Validation	34
5	Conclusions	42

Revision Log

Rev A: Corrected an error in calculating the matching velocity, which was previously incorrectly set to the same value as the velocity upwind of the rotor. Updated the plots.

Rev B: Section 3.6 has been added. This section discusses momentum balance using the full three-component V_i induced velocity vector, in comparison with only the $(V_i^r)_X$ component.

Using the full V_i vector, the matching velocity must also include all three components. This was implemented, and the plots in Chapter 4 have been updated according to the latest version of the software.

Deleted the placeholder chapter on turbulence; the turbulence model can be considered independently of the basic aerodynamic methods described in this document.

Chapter 1

Introduction

A computer program, implementing a double-multiple streamtube type of blade element momentum (BEM) method, has been developed for calculating aerodynamic loads on vertical-axis wind turbine (VAWT) blades. The program is intended for preliminary analyses, with the current motivation being to design the generator torque control system of a Darrieus turbine mounted atop a floating platform.

The blade element momentum method implemented here is not accurate enough to be recommended for final design or certification. More advanced methods are required in order to accurately predict power and loads above the rated windspeed. In particular, a more complex dynamic stall model is required. Also, the present approach does not explicitly represent the convection of flow through the interior of the turbine. These shortcomings are discussed further in Chapters 2 and 3.

Alternatives to the BEM method include wake vortex analysis or some form of CFD. In comparison with the BEM method, these latter approaches are more physically accurate, but are very slow, and can be numerically unstable.¹ In general, it can be said that the BEM method is useful, because it provides an approximate solution with minimal computational effort.

Under quasi-steady conditions, solution by the BEM method consists of iterating between local forces at the blades and the change in the momentum of the air that flows through the surface swept by the blades: these aspects of the analysis are discussed in Chapters 2 and 3, respectively. Under dynamic conditions, though, the calculation is not iterative. Rather, a time-delay function, described in Section 3.5, is applied which numerically damps the momentum calculation.² Provided that timesteps are small, the solution is numerically stable.

The present implementation of the BEM method is well-suited for calculating aerodynamic loads under atmospheric turbulence, as well as translational motion (as a rigid body) of the rotor.³ Limitations in the BEM method – in particular, the lack of an explicit model of the wake as it is convected through the rotor – require the use of simplifying assumptions. The implementation of turbulence in the software can be considered independently from the basic momentum-balance calculation. A discussion of turbulence is therefore deferred to a future document. (Reference [18] presents the results of an initial investigation.)

¹For example, Leishman [12] p 95, discussing free-wake vortex methods

²This time-delay has a physical basis, as it represents the downwind convection of vorticity in the wake.

³... for example, a rotor on a floating wind turbine.

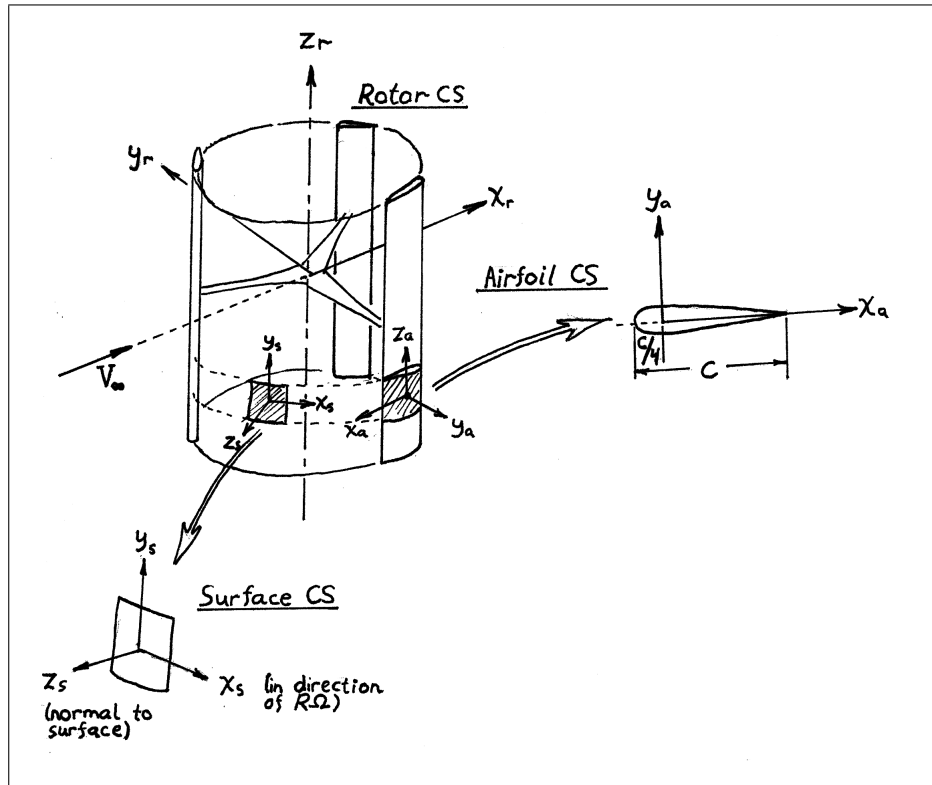


Figure 1.1: Definitions of coordinate systems

Chapter 4 compares output power calculated by the BEM code against measurements on a 17 m diameter turbine tested at Sandia Laboratories. There are clear shortcomings in the BEM method, but the predictions are good enough to be useful for tuning a generator torque control system, provided that some adaptability is built into the algorithm.⁴

1.1 Coordinate Systems

There are three coordinate systems which are relevant to the VAWT aerodynamic loads calculation. These are the rotor, airfoil, and surface coordinate systems, which are shown in Figure 1.1. (There are two other coordinate systems which are needed when turbulence and rotor translation are included in the model. These are a fixed global coordinate system, and the “wind” coordinate system, associated with the turbulent windfield.)

The rotor coordinate system has its origin at the geometric center of the rotor. The Z_r axis is aligned with the axis of rotation, and the X_r axis points in the mean downwind direction. Thus the (Y_r, Z_r) plane defines the “upwind” and “downwind” halves of the rotor. The azimuth angle ψ is defined relative to the X_r axis.

According to the above definition, the rotor coordinate system shifts, relative to a ground-fixed coordinate system, with both the attitude of the turbine and the average direction of the

⁴In other words, the generator torque should not be decided based upon a fixed schedule, as a function of windspeed, derived from a BEM analysis. The algorithm should consider the measured rotational speed and power output and adapt the torque accordingly.

incoming wind. This is necessary in order to define pairs of elements that form a streamtube, without making the calculations unduly complicated. In reality, as the rotor translates or the wind changes direction, the position of the rotor changes with respect to the existing vortex wake. This effect is not captured in the present analysis; it is implicitly assumed that the position of the rotor and the mean wind direction change over timescales that are greater than a couple rotor revolutions. Note, however, that changes in the *incoming* velocity (as opposed to the wake induced velocity) caused by motion of the rotor can be accounted for by modifying the input velocity field.

There is an airfoil coordinate system associated with each blade element. The origin of the airfoil coordinate system is located at the quarter-chord point. The X_a axis is opposite the direction of rotation, and the Y_a axis is perpendicular to the swept surface, when the blade pitch and twist angles, measured about the Z_r axis, are zero. The angle-of-attack α is defined relative to the airfoil coordinate system.

Finally, there is a surface coordinate system associated with each swept surface element. (The swept surface is the surface formed by rotating the blade quarter-chord line 360° about the Z_r axis.) The Z_s axis is normal to the surface, pointing outwards, while the X_s axis points in the direction of rotation. The surface coordinate system is used in the momentum balance portion of the calculation.

It is required to refer vectors to one coordinate system or the other. This requires use of transformation matrices. The transform from the rotor to the airfoil coordinate system is defined in the following manner:

1. Define Z_a parallel to Z_r , Y_a parallel to X_r , and X_a opposite Y_r :

$$T_1 = \begin{bmatrix} 0 & -1 & 0 \\ 1 & 0 & 0 \\ 0 & 0 & 1 \end{bmatrix}. \quad (1.1)$$

2. Rotate about the Z_r axis by the blade pitch angle ζ plus twist angle ξ :

$$T_2 = \begin{bmatrix} \cos(\zeta + \xi) & \sin(\zeta + \xi) & 0 \\ -\sin(\zeta + \xi) & \cos(\zeta + \xi) & 0 \\ 0 & 0 & 1 \end{bmatrix}. \quad (1.2)$$

3. Rotate about the Y_r axis by the blade tilt angle β (Figure 1.2):

$$T_3 = \begin{bmatrix} \cos \beta & 0 & -\sin \beta \\ 0 & 1 & 0 \\ \sin \beta & 0 & \cos \beta \end{bmatrix}. \quad (1.3)$$

4. Rotate about the Z_r axis by the azimuth angle ψ :

$$T_4 = \begin{bmatrix} \cos \psi & \sin \psi & 0 \\ -\sin \psi & \cos \psi & 0 \\ 0 & 0 & 1 \end{bmatrix}. \quad (1.4)$$

5. Finally:

$$T_r^a = T_1 T_2 T_3 T_4, \quad \text{and} \quad T_a^r = (T_r^a)^{-1} = (T_r^a)^T. \quad (1.5)$$

Definition of the surface coordinate system is similar:

1. Define Y_s parallel to Z_r , and Z_s parallel to X_r :

$$T_1 = \begin{bmatrix} 0 & 1 & 0 \\ 0 & 0 & 1 \\ 1 & 0 & 0 \end{bmatrix}. \quad (1.6)$$

2. Rotate about the Z_r axis by the offset angle η (Figure 1.3):

$$T_2 = \begin{bmatrix} \cos \eta & \sin \eta & 0 \\ -\sin \eta & \cos \eta & 0 \\ 0 & 0 & 1 \end{bmatrix}. \quad (1.7)$$

3. Rotate about the Y_r axis by the blade tilt angle β (Figure 1.2):

$$T_3 = \begin{bmatrix} \cos \beta & 0 & -\sin \beta \\ 0 & 1 & 0 \\ \sin \beta & 0 & \cos \beta \end{bmatrix}. \quad (1.8)$$

4. Rotate about the Z_r axis by the azimuth angle ψ :

$$T_4 = \begin{bmatrix} \cos \psi & \sin \psi & 0 \\ -\sin \psi & \cos \psi & 0 \\ 0 & 0 & 1 \end{bmatrix}. \quad (1.9)$$

5. Finally:

$$T_r^s = T_1 T_2 T_3 T_4, \quad \text{and} \quad T_s^r = (T_r^s)^{-1} = (T_r^s)^T. \quad (1.10)$$

1.2 Problem Setup and Required Inputs

The following information is required as input to the BEM method:

1. the blade profile, in terms of (r, z) coordinates defining a discrete set of nodes in cylindrical polar coordinates; also, the tangential distance out of the (r, z) plane, if the blade is offset or swept like an airplane wing;
2. aerodynamic lift, drag, and moment coefficients C_L , C_D , and C_M for each blade element, with properties being assumed constant between each set of nodes;
3. the chord length and static twist angle of each blade element, along with the pitch angle of the blade;
4. the number of blades and the azimuth angle of blade number one (the blades are assumed to be equally spaced);
5. the rotational speed;
6. the properties of the ambient air: density and viscosity; and,
7. the magnitude and direction of airflow incident upon each element of the upwind half of the swept surface; that is, at a particular location on the rotor, the velocity that the air would have if the rotor were not there.

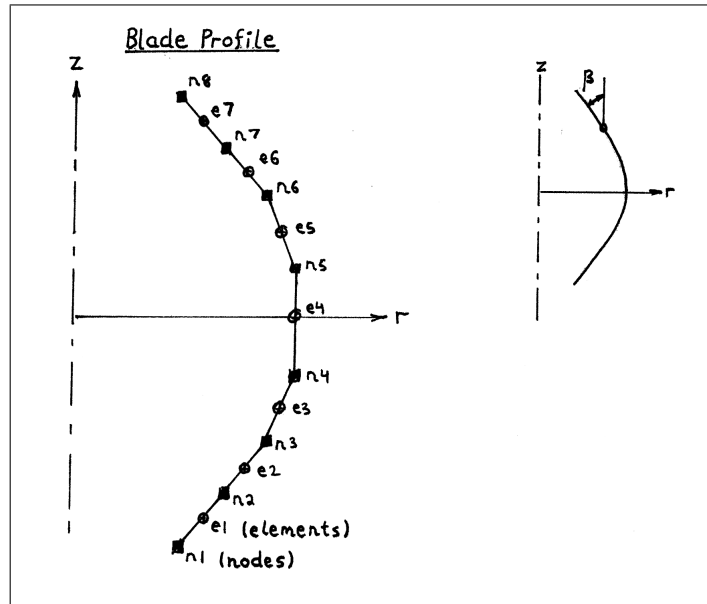


Figure 1.2: Blade profile definition

1.2.1 Discretization of the Blade and Swept Surface

The blade is defined by a profile of nodes in cylindrical coordinates (Figure 1.2): distance from the axis of rotation r , distance along the axis of rotation z , and a tangential offset (Figure 1.3). Note that a tangential offset (“swept wing”) is equivalent, from the perspective of a blade element, to increasing the radius and modifying the blade pitch angle.

Blade elements are defined between adjacent nodes, interpolating separately the magnitude and direction of the vector coordinate of each node. The element’s normal vector is perpendicular to the line connecting its bounding nodes.

Figure 1.4 illustrates the discretized swept surface. To discretize the swept surface into surface elements, the blade profile is rotated at discrete intervals, interval k being at azimuth angle $90^\circ + (\delta\psi)/2 + k \delta\psi$. At each interval, the (rotated) blade element centroids and normal vectors define the surface element centroids (x_s) and normal vectors (n_s). Thus, the length of each surface element is the same as its generating blade element. The width of each surface element is:

$$w_e = \delta\psi \sqrt{(x_s^r)_X^2 + (x_s^r)_Y^2}. \quad (1.11)$$

1.2.2 Chord, Twist, and Pitch

The chord of the blade, c , is defined as in Figure 1.1. Figure 1.5 illustrates twist and pitch angles. The twist angle of a blade element, ξ , is the rotation about the Z_a axis, relative to some fixed reference on the blade. The pitch angle of the blade, ζ , is the rotation of all elements on the blade, about their Z_a axes. The algorithm that transforms coordinates should work for straight blades with twist and pitch control, or an arbitrary blade profile with twist, but not an arbitrary blade profile with pitch control, because the algorithm does not account for the translation of elements which are not aligned with the blade pitch axis.

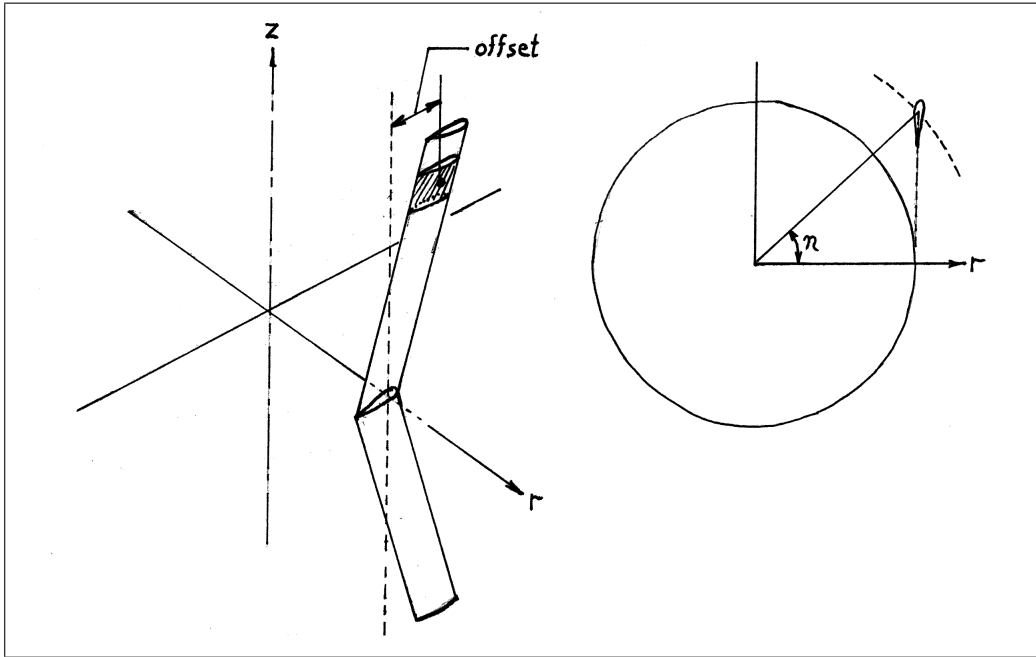


Figure 1.3: Offset of the blade profile to define a “swept-wing” configuration

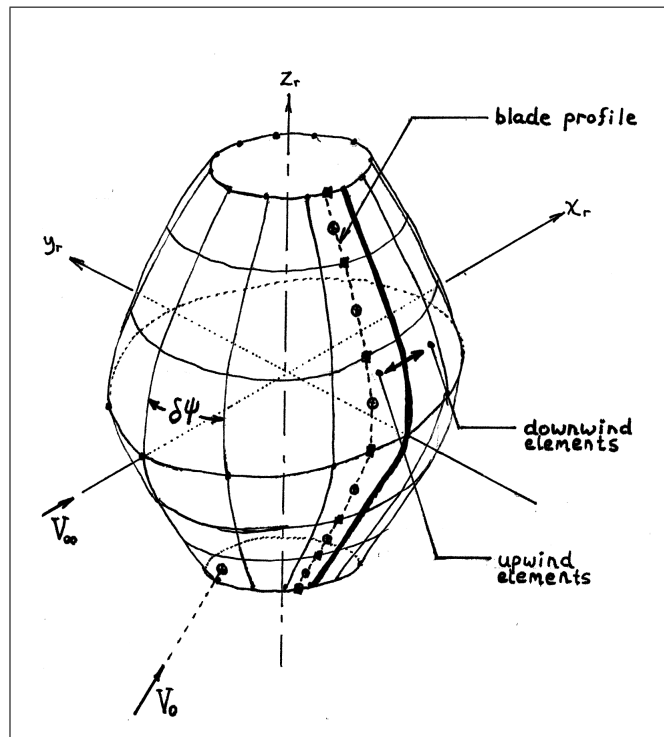


Figure 1.4: Discretization of the swept surface by rotating the blade profile

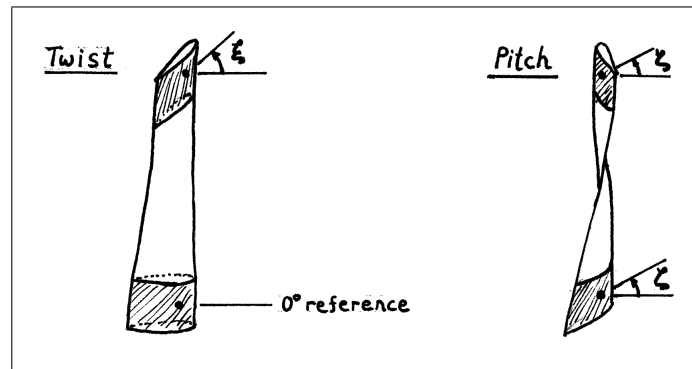


Figure 1.5: Blade twist and pitch angles

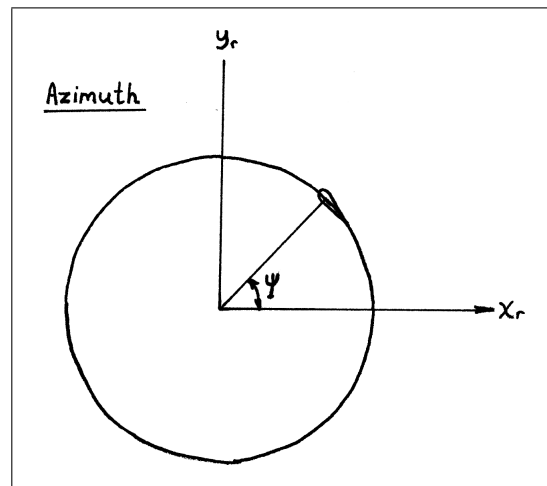


Figure 1.6: Azimuth angle

1.2.3 Blade Azimuth Angle

For purposes of input, one of the blades is designated Blade #1, and an initial azimuth angle is given for this blade; Figure 1.6. The other blades are assumed to be evenly spaced about the azimuth.

1.2.4 Incoming Airflow

The incoming air velocity vector, V_0 , must be given for each upwind surface element. An example is shown in Figure 1.4. The V_0 vectors may vary in magnitude and direction, in order to model turbulence, however assumptions of the analysis will be violated if the direction of incoming flow diverges greatly from one surface element to another. That is, turbulence should be small fluctuations imposed on a uniform incoming flow.

Chapter 2

Airfoil Forces

Airfoil forces are computed by first looking up coefficients from an input table, as a function of Reynolds number Re and the instantaneous angle-of-attack α , and then correcting the coefficients for dynamic stall.

Interpolating coefficients from the input table is the most computationally-intensive part of the BEM calculation. The calculation can be sped up significantly by modelling the coefficient curves with a series of closed-form equations, as functions of Re and α .

2.1 Airfoil Coefficients

Induced velocity V_i^a , remote air velocity V_0^a , and blade velocity V_b^a are obtained in airfoil coordinates, transforming from rotorplane coordinates. Relative air velocity at the airfoil is calculated as:

$$V^a = V_0^a + V_i^a - V_b^a \quad (2.1)$$

Figure 2.1 shows an example of these velocity vectors. (Note that V_b in the sketch is drawn negative, opposite the velocity of blade motion. V_b should be input to the software as the positive velocity vector of blade motion.)

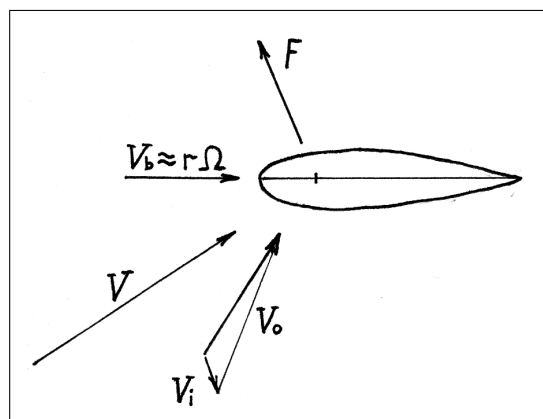


Figure 2.1: Velocity vectors that are components of the local velocity at the blade

Here an approximation must be made. Airfoil coefficients are based upon test data in which there is no spanwise flow, perpendicular to the airfoil cross-section. In most cases, the flow about an actual wind turbine blade will have a spanwise component of velocity, especially with a Darrieus type turbine, portions of whose blades are not perpendicular to the wind. This spanwise velocity is neglected when computing airfoil loads. Define a velocity magnitude:

$$|V| = \sqrt{(V^a)_X^2 + (V^a)_Y^2} \quad (2.2)$$

where $(V^a)_X$ is the X component and $(V^a)_Y$ the Y component of relative air velocity in airfoil coordinates. Define the angle-of-attack:

$$\alpha = \tan^{-1} \left(\frac{(V^a)_Y}{(V^a)_X} \right) \quad (2.3)$$

Define Reynolds number:

$$\text{Re} = \frac{\rho |V| c}{\mu} \quad (2.4)$$

where ρ is air density, μ is air viscosity, and c is the airfoil chord length. Given Reynolds number and angle-of-attack, airfoil coefficients are calculated using linear interpolation between available tabulated values. Forces are computed from airfoil coefficients:

$$\begin{aligned} F_L &= \frac{1}{2} C_L \rho |V|^2 c L \\ F_D &= \frac{1}{2} C_D \rho |V|^2 c L \\ M &= \frac{1}{2} C_M \rho |V|^2 c^2 L \end{aligned} \quad (2.5)$$

Lift and drag forces are broken into their components in the airfoil coordinate system:¹

$$\begin{aligned} (F_b^a)_X &= -F_L \sin \alpha + F_D \cos \alpha \\ (F_b^a)_Y &= F_L \cos \alpha + F_D \sin \alpha \\ (M_b^a)_Z &= M \end{aligned} \quad (2.6)$$

The Z component of moment results in torsion of the blade. This moment plays no role in the remainder of the momentum balance calculation, although it is included in the final loads output.

¹Drag and lift forces are by definition parallel to and perpendicular to the flow direction at the blade. The airfoil X and Y axes are parallel to and perpendicular to the chord of the airfoil. Drag and lift are offset from the airfoil X and Y axes by the angle-of-attack.

2.1.1 Airfoil Coefficient Extrapolation

Tabulated airfoil data rarely includes coefficients for angles-of-attack significantly beyond stall; for typical airfoils, stall occurs when the magnitude of angle-of-attack exceeds somewhere between 10° and 20° .² The blades of a VAWT will operate beyond stall over the downwind portion of rotation when windspeeds are high. Therefore, values for coefficients at high angles-of-attack must be estimated theoretically; a modified flat-plate theory is used.

To estimate lift and drag coefficients (C_L and C_D) in the deep-stall range, first a matching point is defined as the last (highest angle-of-attack) data that the user has entered. Denote the matching point with a subscript s : C_{L_s} , C_{D_s} , and α_s .

The maximum drag, when the airfoil is oriented perpendicular to the flow ($\alpha = \pm 90^\circ$), is calculated by:³

$$C_{D,\max} = 2 - 0.82 \left(1 - e^{-17/\text{AR}}\right) \quad (2.7)$$

where AR is the aspect ratio of the entire blade, which can be computed by:⁴

$$\text{AR} = \frac{(R_o - R_i)^2}{\sum (c L)} \quad (2.8)$$

Then, lift and drag coefficients are extrapolated by the following formulas:⁵

$$C_L = \frac{C_{D,\max}}{2} \sin 2\alpha + (C_{L_s} - C_{D,\max} \sin \alpha_s \cos \alpha_s) \left(\frac{\sin \alpha_s}{\cos^2 \alpha_s} \right) \left(\frac{\cos^2 \alpha}{\sin \alpha} \right) \quad (2.9)$$

$$C_D = C_{D,\max} \sin^2 \alpha + \frac{C_{D_s} - C_{D,\max} \sin^2 \alpha_s}{\cos \alpha_s} \cos \alpha \quad (2.10)$$

Moment coefficient extrapolation is performed by the method of Lindenburg. [15] First, the airfoil, when oriented perpendicular to the flow, is represented by a wedge, as shown in Figure 2.2. Nose and tail wedge angles ϕ_n and ϕ_t are estimated by the user, and defined in the airfoil data file. Next, normal force coefficient is calculated by rotating lift and drag coefficients into rotorplane coordinates:

$$C_N = C_L \cos \alpha + C_D \sin \alpha \quad (2.11)$$

A semi-empirical expression is used to compute the location at which the resultant of the normal force acts. As a fraction of chord length, the expression is:⁶

$$x_{cp} = 0.5 - 0.35[\phi_t(0.2 + 0.08\phi_t)]$$

²Abbott and von Doenhoff [1] appendix IV

³Lindenburg [15], figure 2.4, plots several proposed expressions for the drag of a rectangular plate, orthogonal to the flow, as a function of the plate's aspect ratio. The expressions are all essentially in agreement with each other and with the test data. I used the one recommended by Lindenburg.

⁴ c and L are the chord and spanwise lengths of individual blade elements. The sum is taken over all the elements on the current blade.

⁵Moriarty and Hansen [19] p 22; watch out for the typo in equation 102.

⁶The expressions for x_{cp} and C_M were taken from Lindenburg [15], p 16.

$$+(0.3 - \phi_n(0.2 + 0.08\phi_n))(1 - 1.8\sqrt{r_n/c} - 0.3] \quad (2.12)$$

where r_n is the nose radius, and c is the chord, as shown in Figure 2.2. Note that ϕ_n and ϕ_t should be in units of radians when used in the above equation (they are input by the user as degrees). Moment coefficient is calculated by:

$$C_M = -C_N \left[x_{cp} - 0.16 \left(1 - \frac{2\alpha}{\pi} \right) - 0.25 \right] \quad (2.13)$$

where α is in radians.

2.2 Dynamic Stall

The aerodynamic pressure forces on an airfoil exhibit time-history effects; the forces at a given point in time are a function of both the instantaneous and previous flow conditions. In wind turbine analysis software, these time-history effects are typically referred to as dynamic stall; although time-history effects are present under all flow conditions, they are particularly pronounced in the vicinity of initial stall.

Dynamic stall behavior dominates the performance of a vertical-axis wind turbine above the rated windspeed. (Figures 4.2 and 4.8 show examples.) There is a large difference in the predicted power at high windspeeds, between analyses that omit and include dynamic stall.

Although the flow about a blade in stall is highly complex, simplified engineering methods have been shown to capture the most important effects. One example is the Leishman-Beddoes dynamic stall model,⁷ which includes:

1. a time-delay associated with the change in circulation (lift) under attached-flow conditions;
2. a time-delay associated with the change in leading-edge pressure, which lags the circulation;
3. a time-delay associated with the movement of the separation point (the chordwise location on the airfoil at which flow separates from the low-pressure surface), which lags the leading-edge pressure; and,
4. a model of vortex shedding from the leading-edge, which tends to occur under large changes in angle-of-attack, and results in a sharp spike in the normal force.

An alternative, and much simpler, dynamic-stall model was presented by Øye [20]. This approach combines the first three time-delays into a single one, and omits leading-edge vortex shedding. Studies comparing dynamic stall models, such as Larsen et al. [11] and Paraschivoiu ([21], Section 6.5), indicate that the Leishman-Beddoes dynamic stall model is more accurate, but that the Øye model captures the most important effect, which is the delay in motion of the separation point.⁸ In light of this, it was decided to implement the Øye model in the present version of the BEM software.

⁷Leishman and Beddoes [13],[14]

⁸The data presented by Gupta and Leishman [5] indicates that the “trigger” for leading-edge vortex shedding, defined in the Leishman-Beddoes model, does not always trip when it should. In other words, the Leishman-Beddoes model does not always properly account for leading-edge vortex shedding. Correcting this would require refinement of the criteria for initiation of vortex shedding.

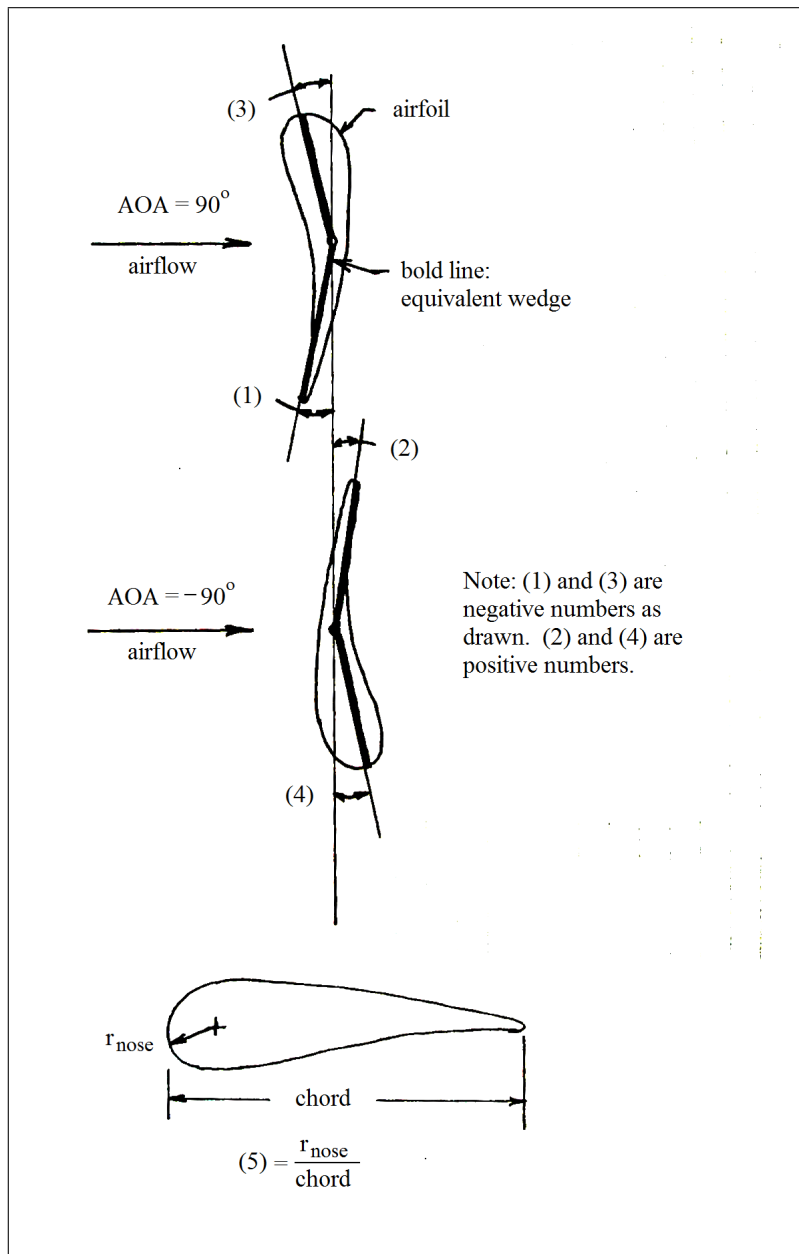


Figure 2.2: Definition of parameters used to extrapolate airfoil coefficients

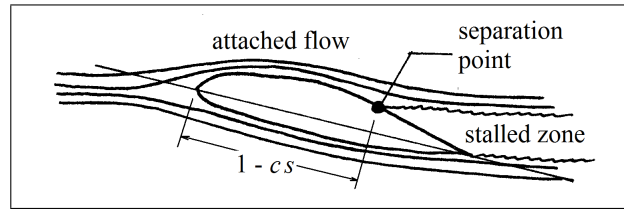


Figure 2.3: A parameterization of the location of the separation point along the low-pressure surface, in terms of the parameter s

2.2.1 Separation Point Motion

The basic features of dynamic stall can be understood in terms of a time-delay on the motion of the separation point with respect to the instantaneous angle-of-attack. To express this mathematically, the position of the separation point along the low-pressure surface of the airfoil is parameterized by a variable s . The definition of s is sketched in Figure 2.3: it is the fraction of the chord length measured from the trailing edge to the point of flow separation. Positive angles-of-attack are associated with positive s , and negative angles-of-attack are associated with negative s . Thus s is zero when flow is fully-attached, +1 when flow is fully-separated due to a large positive α , and -1 when flow is fully-separated due to a large negative α .⁹

Following Hansen et al. [6], the instantaneous lift coefficient C_L can be related to s by the Kirchhoff formula:¹⁰

$$C_L = \frac{1}{4} \left(\frac{dC_L}{d\alpha} \right)_a (\alpha - \alpha_z) \left(1 + \sqrt{1 - |s|} \right)^2. \quad (2.14)$$

Here, α_z is the angle-of-attack at zero lift, and:¹¹

$$\left(\frac{dC_L}{d\alpha} \right)_a = \max_{\alpha_q} \left[\frac{C_{Lq}}{\alpha_q - \alpha_z} \right]; \quad (2.15)$$

Equation 2.14 is valid when $|s| < 1$. For $|s| \geq 1$, the quasi-steady coefficient curve applies.

2.2.2 Implementation of the Øye Method

The key equation of the Øye method states that the instantaneous position of the separation-point s lags the quasi-steady position s_q – that is, s_q would be the location of the separation-point if α were held constant for a long time. The time-lag function is:

$$\frac{ds}{dt} = \frac{s_q - s}{\tau}. \quad (2.16)$$

⁹This is opposite the usual definition of the separation-point position, which is typically measured from the *leading* edge. Because here we are dealing with both positive and negative angles-of-attack, it is most convenient that the separation-point parameter be continuous across the trailing edge.

¹⁰Leishman and Beddoes relate the *normal* force to s using this expression. The distinction is not so important for small angles-of-attack. In the context of the Øye method, it has been shown (for instance Fuglsang [3]) that there is very little hysteresis in the drag force, thus it seems appropriate to limit the separation-point function to the lift force.

¹¹This comes from Hansen et al. [6] pp 11-12.

This has the solution:

$$s(t) - s_q = [s(t_0) - s_q]e^{-(t-t_0)/\tau}. \quad (2.17)$$

The present method differs from the original Øye model [20] in two ways. First, the Kirchhoff formula, Equation 2.14, is used to relate the position of the separation point to the lift coefficient. (This is consistent with Hansen et al. [7]. Øye used interpolation between the lift coefficient under fully-attached flow and a simplified estimate of the lift coefficient under fully-separated flow.) Second, the separation point is allowed to travel along both the upper and lower sides of the airfoil, because the angle-of-attack on a VAWT blade may be positive or negative. Special logic is required to handle the transition between flow separation on the upper and lower surfaces; otherwise, unrealistically high forces are obtained. This logic is described in Section 2.2.3. Here we limit the discussion to fluctuations that do not change the sign of the angle-of-attack.

The modified Øye method requires, as input, tabulated C_{Lq} versus α data. This is the standard quasi-steady lift coefficient data; but here it is necessary to mark it with a q subscript, since the instantaneous value of C_L deviates from the quasi-steady curve. Several quantities must be defined (or located by searching numerically) based upon the tabulated data. These are α_z and $(dC_L/d\alpha)_a$, from above, and the angle-of-attack at which flow is fully separated, α_{FS} . This latter quantity is calculated by setting s to 1 (or -1) in Equation 2.14:

$$\alpha_{FS} = \alpha_z + 4 \frac{C_{Lq}}{(dC_L/d\alpha)_a}, \quad (2.18)$$

where both C_{Lq} and α_{FS} lie upon the quasi-steady curve.¹²

Here is how the dynamic stall calculation works for a single timestep. For a given, instantaneous angle-of-attack α (here considering only positive values, to keep the discussion simple), the quasi-steady position of the separation point can be calculated from Equation 2.14:

$$s_q = \begin{cases} 1; & \alpha \geq \alpha_{FS} \\ 1 - \left(2 \sqrt{\frac{C_{Lq}}{(dC_L/d\alpha)_a(\alpha - \alpha_z)} - 1} \right)^2; & \alpha < \alpha_{FS} \end{cases} \quad (2.19)$$

Equation 2.17 can be written, using discrete timesteps:

$$s(t) = s_q + [s(t - \Delta t) - s_q] e^{-\Delta t/\tau_s}, \quad (2.20)$$

which can be evaluated numerically, using s from the previous timestep, and the value of s_q from Equation 2.19.¹³

Once the position of the separation point s is known, the instantaneous lift coefficient can be calculated from Equation 2.14. It should be emphasized that in Equation 2.14 α is the instantaneous angle-of-attack, and s is the instantaneous separation point position. Observe that Equation 2.14 has been applied multiple times, to solve for different quantities. This is consistent, though, because different values of lift coefficient, angle-of-attack, and separation point have been used each time.

¹² C_{Lq} is positive when α is positive, and negative when α is negative.

¹³It is assumed that s_q changes over a timescale that is large in comparison with Δt . Since s_q is calculated based upon the instantaneous α , this means that the timestep Δt must be fine enough to smoothly capture changes in α .

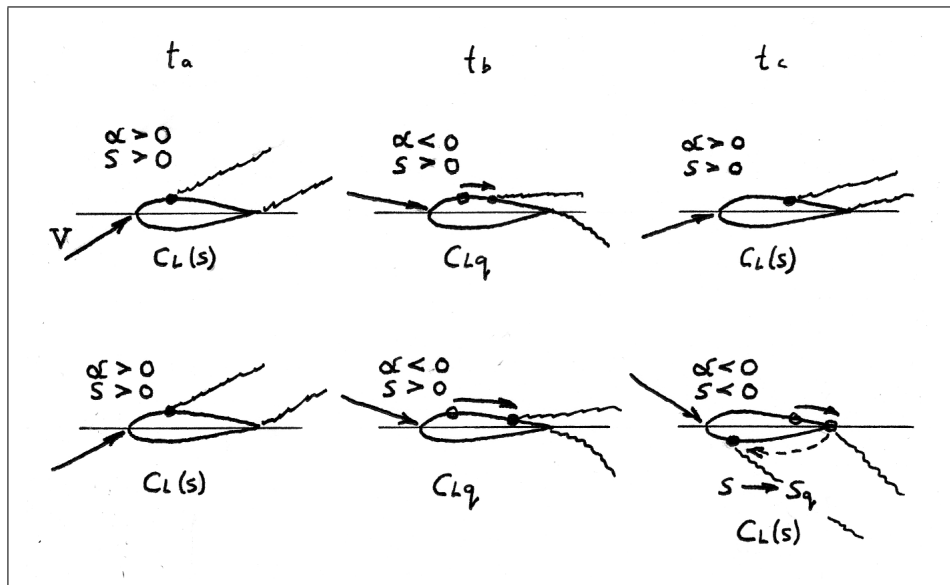


Figure 2.4: A sketch of two possible scenarios in which the sign of the angle-of-attack changes: in the first scenario, the sign changes only briefly, not long enough for the separation-point to reach the trailing edge on (what has now become) the high-pressure surface; in the second scenario, the sign changes for a longer length of time

2.2.3 Positive and Negative Angles-of-Attack

As a vertical-axis wind turbine rotates, the blade retreats from the wind over part of the cycle. When the windspeed is high, the angle-of-attack shifts rapidly from a large negative value to a large positive value, over a timescale that is comparable to τ ; therefore dynamic stall is relevant.¹⁴ However, the dynamic stall equations are not well-defined when α and s are of opposite sign. Numerical studies showed that special logic is required to handle this situation.¹⁵

The logic is sketched in Figure 2.4, in this case for an angle-of-attack that begins positive and ends up negative. (The logic for an angle-of-attack that begins negative and ends up positive is the same, switching $<$ and $>$ signs.) The starting point, at time t_a , is a large positive α , such that s is near 1. At time t_b , which is a very short time after t_a , α has rapidly decreased and become negative. Due to the time-lag (Equation 2.16), s remains on the upper (what has become the high-pressure) surface, although it begins to move towards the trailing edge.

The first question is: what should the value of the lift coefficient be at time t_b , when α and s are of opposite sign? In reality, the state of flow about the airfoil will be complicated, and not easily represented by a simple force coefficient. It appears, though, that reasonable results are obtained if C_L is set to the quasi-steady value, C_{Lq} . For a retreating blade, in high winds, α progresses from a large positive to large negative value; letting $C_L = C_{Lq}$ results in

¹⁴Dynamic stall is also relevant on the upwind half of the rotation, but here the angle-of-attack is nicely behaved.

¹⁵Without special logic, it was observed that airfoil forces jumped instantaneously from one value to another; also, forces became unrealistically high when α and s were of opposite sign.

a local power that is near zero, and a local thrust that points consistently downwind.

In some cases, in the immediate vicinity of $\psi = 270^\circ$, as the blade crosses from the upwind to downwind halves of the swept surface, and α is near zero, it may switch signs several times, all in the span of a few timesteps.¹⁶ This case is shown in the upper row of Figure 2.4. If, as in this example, α fluctuates from positive to negative to positive again, with s remaining positive the entire time,¹⁷ then at time t_c the lift coefficient should be calculated according to Equation 2.14. In other words, the calculation should proceed as if α never changed sign.

The lower row in Figure 2.4 shows a more typical case, when α retains its new sign. In reality, what will happen is that over some short period of time (a bit less than τ), the original circulation will be convected away, and circulation will build in the new direction, with flow separating from the new low-pressure surface, if α is large enough. It was found that reasonable results are obtained if initially (at time t_b) C_L is allowed to attain its quasi-steady value C_{Lq} . Now, let t_c be the time at which the separation point (evolving according to Equation 2.17, as usual) reaches the trailing edge, and s switches sign. As it switches sign, s is made to “jump” to s_q , associated with α and C_{Lq} . Then, during subsequent timesteps, the calculation proceeds as normal, according to Equations 2.14 and 2.17.

The above logic has the advantages that (1) there is no abrupt jump in the lift force as s “rounds the corner” at the trailing edge, even if α varies wildly; and (2) the time-delay as s approaches the trailing edge has a physical basis, since, when α abruptly changes sign, circulation and flow separation must build on the new low-pressure surface.

2.2.4 An Example of Dynamic Stall

The above dynamic stall calculations are illustrated here with an example. The VAWT BEM software was used to compute the aerodynamics of the Sandia 17 m diameter Darrieus VAWT, in its configuration with two NACA 0012 blades.¹⁸ The turbine was set to rotate at a constant speed of 3.52 rad/s (33.6 rpm). The incoming wind was uniform and constant.

For a first analysis, the windspeed was set to 10 m/s. Figure 2.5 plots the angle-of-attack α , separation-point position s , and contribution to the thrust $(F^r)_X$ and torque T of a blade element adjacent to the equator of the turbine. (The blades were discretized into 20 elements along their length – corresponding to rows of the swept surface – thus Row 10 is just below the equator.) Here ψ is the azimuth angle, defined such that $\psi = 0$ when the blade crosses from the downwind to the upwind side of the rotor (the Y^r axis).

The angle-of-attack varies through a range of approximately -20° to $+20^\circ$, which means that the airfoil passes into and out of stall. This is evident from the separation-point position, which nears a magnitude of 1 (fully-separated flow) over both the upwind and downwind halves of the cycle.

It is observed that there are sharp changes in the torque curve in the vicinity of $\psi = 150^\circ$ and $\psi = 210^\circ$. These are artifacts of the quasi-steady drag coefficient curve,¹⁹ which features an abrupt increase in drag at an angle-of-attack of about 12° ; thus the “jumps” in the torque are not related to the dynamic stall calculation.

At an azimuth ψ of about 205° , there is a jump in the separation-point position, from zero

¹⁶This has to do with the calculation of induced velocity.

¹⁷The logic given here is valid even if *alpha* changes signs an unlimited number of times, as long as the sign of s stays the same.

¹⁸Chapter 4 provides references which contain a description of this turbine.

¹⁹See Figure 2.6.

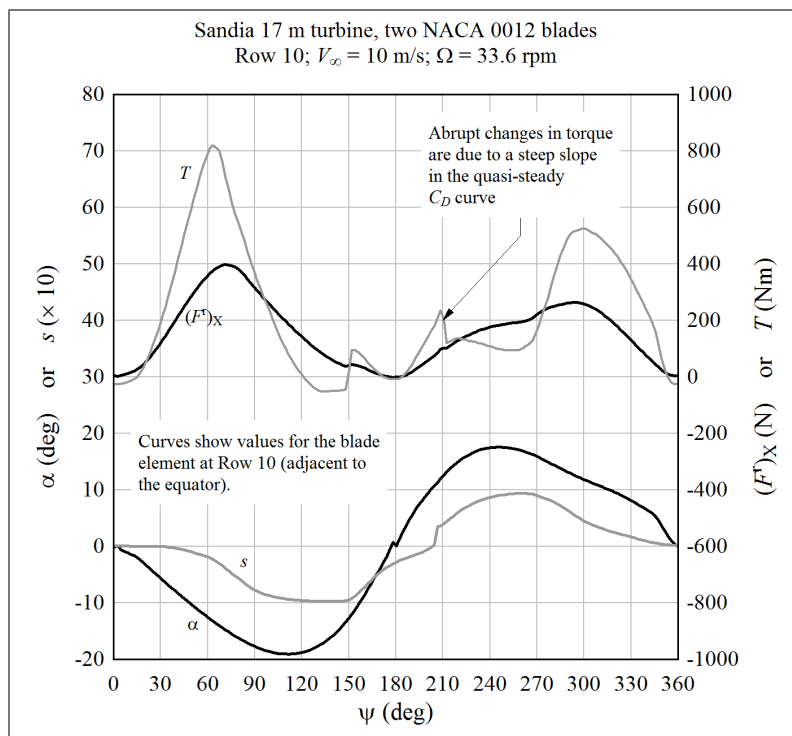


Figure 2.5: A plot of the aerodynamic state and forces at a location on the blade near the equator of the turbine, at a windspeed slightly over rated (for the chosen rotational speed)

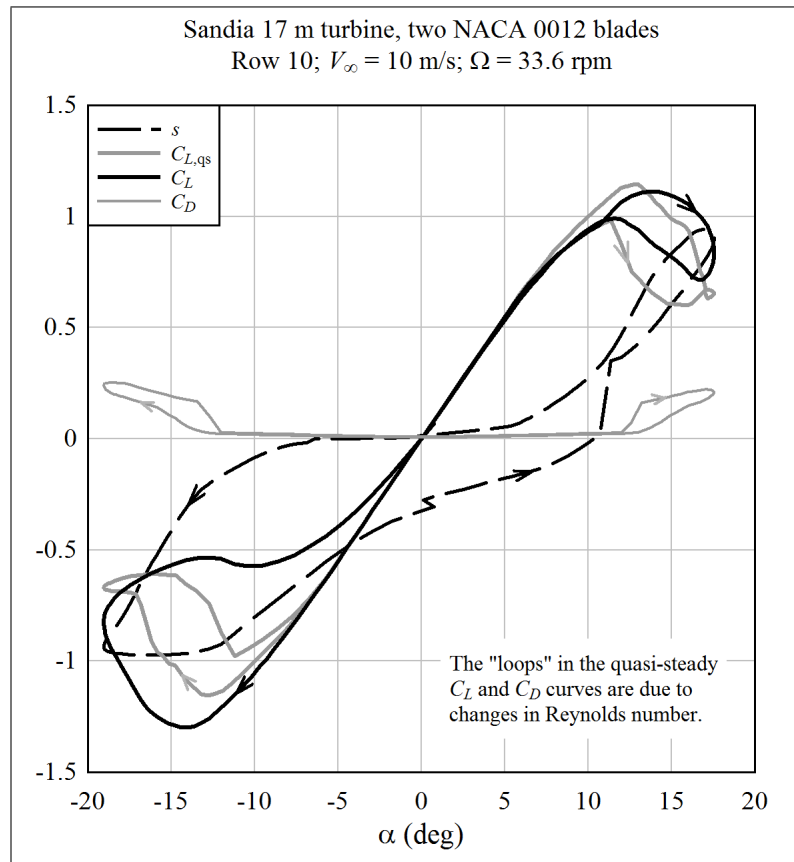


Figure 2.6: A plot of the aerodynamic state and forces at a location on the blade near the equator of the turbine, at a windspeed slightly over rated (for the chosen rotational speed), presented as airfoil coefficient curves

to its quasi-steady value. This is due to the logic shown in Figure 2.4, where the circulation about the airfoil is “recovering” from an abrupt change in the sign of the angle-of-attack, occurring at an azimuth of 180° . It can be seen from the thrust curve that the forces on the airfoil stay consistent as the separation-point position is reset.

Figure 2.6 provides an alternate view of the same blade element forces. Here the forces (expressed in the local airfoil coordinate system) are reduced to lift and drag coefficients, and are plotted against the instantaneous angle-of-attack.

The quasi-steady lift coefficient $C_{L,qs}$ is plotted as a thick gray line. It is noteworthy that there is significant hysteresis in the quasi-steady curve; this is due to changes in the Reynolds number as the airfoil advances and retreats from the incoming wind. (The NACA 0012 airfoil is sensitive to the value of Reynolds number in the range 5.6×10^5 to 1.2×10^6 .)

The actual lift coefficient C_L is plotted as a thick black line. Starting with $\psi = 0^\circ$, at which $\alpha \approx 0^\circ$, α decreases, and a large dynamic-stall loop occurs as the airfoil sweeps over the upwind half of the rotor. As the airfoil retreats from the wind in the vicinity of $\psi = 180^\circ$, α rapidly changes sign. It can be seen that α becomes positive while s is still negative. Here, the logic of Section 2.2.3 dictates that the lift coefficient should follow the quasi-steady value, which is indeed what is observed in Figure 2.6. After some time delay, over which circulation

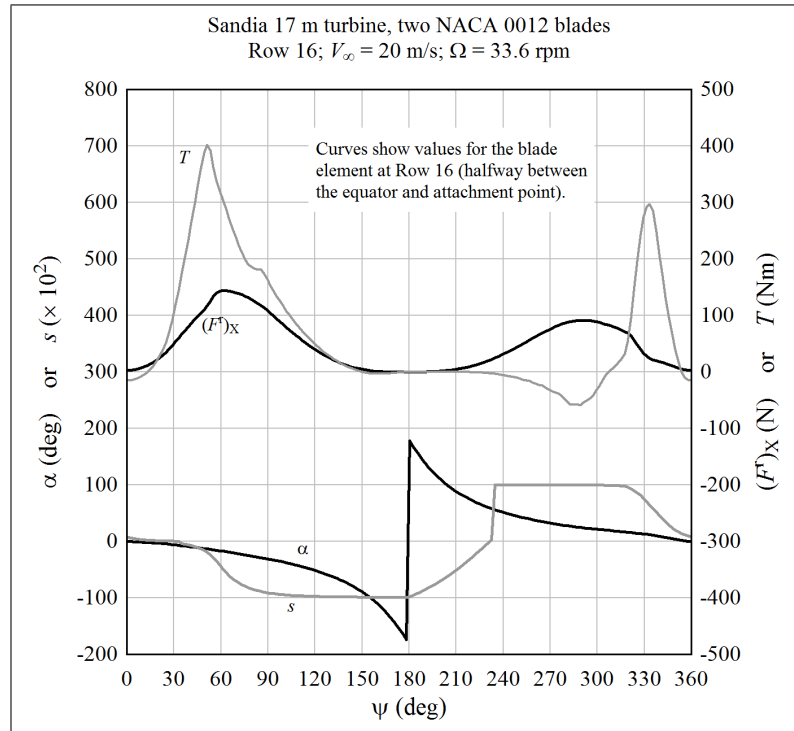


Figure 2.7: A plot of the aerodynamic state and forces at a location on the blade near the root of the blade, at a high windspeed

builds, s changes sign and jumps to its quasi-steady value. After this, the dynamic-stall calculation proceeds as normal, and a small hysteresis loop is observed as the airfoil sweeps over the downwind half of the rotor.

Abrupt changes in drag are evident in Figure 2.6; it is these which resulted in corresponding changes in torque, seen in Figure 2.5.

A second case was run, in which the windspeed was set to 20 m/s. Data was collected for a blade element at Row 16, which is midway between the equator and the root of the blade. Here the blade is slanted at an angle of about 33° with respect to the vertical.

Figures 2.7 and 2.8 show the angle-of-attack, separation-point position, and forces. In this case, the angle-of-attack cycles through 360° as the rotor rotates. Torque is produced over the half-cycle where the blade advances into the wind: the angle-of-attack crosses zero, so flow briefly attaches. (Attached flow can be identified by values of s near zero, in Figure 2.7 in the range $0^\circ \leq \psi \leq 45^\circ$.)

Figure 2.8 shows the airfoil forces, plotted as coefficient curves, in the vicinity of the region of attached flow. The angle-of-attack progresses from positive to negative – right to left, in Figure 2.8 – as the rotor spins. Due to the time-delay on flow attachment, the airfoil does not achieve its full quasi-steady lift coefficient when α is positive; but then there is a pronounced dynamic-stall response when α is negative.

When the blade is retreating from the wind, the flow comes from behind the blade, passing across the trailing edge. This is the reason for the jump from $\alpha = -180^\circ$ to 180° seen in Figure 2.7. Here the airfoil coefficients are equal to their quasi-steady values.

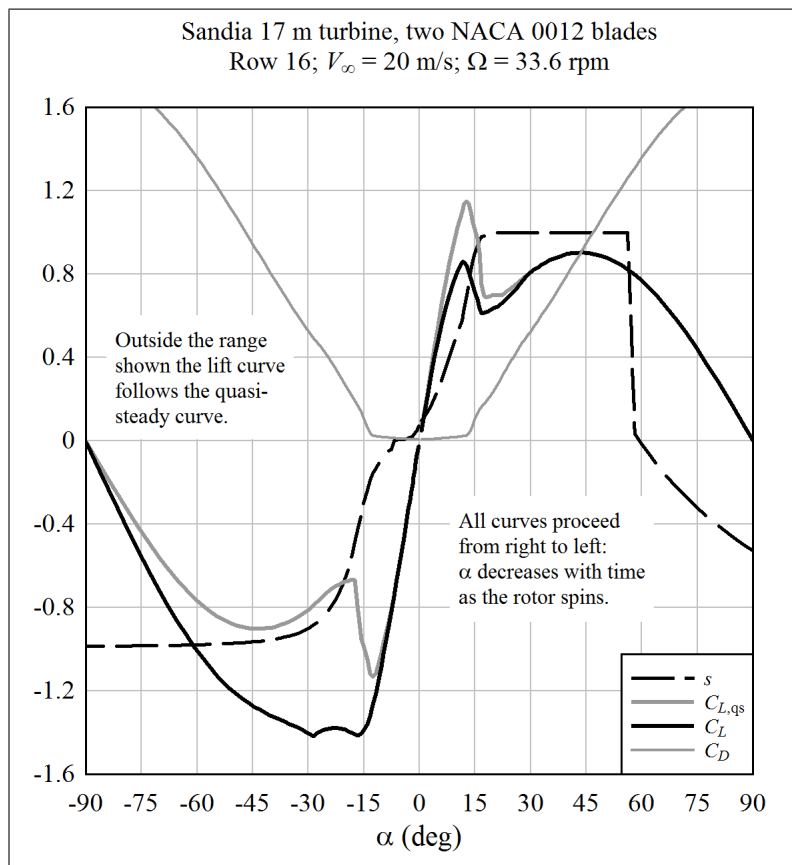


Figure 2.8: A plot of the aerodynamic state and forces at a location on the blade near the root of the blade, at a high windspeed, presented as airfoil coefficient curves

It is seen that the dynamic stall logic of Section 2.2.3 results in smooth and continuous variations in forces over the entire angle-of-attack range.

2.2.5 Changes in Reynolds Number

The lift coefficient curve varies with the Reynolds number, and the Reynolds number varies with the local flow velocity. Therefore, to be precise, the dynamic stall parameters α_z , α_{FS} , and $(dC_L/d\alpha)_a$ should be derived from the coefficient tables during every timestep. This is computationally intensive. It is noted, however, that the coefficient curves are only weakly dependent upon the Reynolds number. Therefore, in the software, the parameters α_z , α_{FS} , and $(dC_L/d\alpha)_a$ are determined upfront, based upon a Reynolds number calculated using a nominal local velocity:²⁰

$$V = \sqrt{(r\Omega)^2 + V_\infty^2}, \quad (2.21)$$

with $r = \sqrt{(x_b^r)_X^2 + (x_b^r)_Y^2}$, where x_b^r is the position of the blade element centroid, in rotor coordinates.

²⁰In the software, a block of code is included which, when un-commented, updates these parameters on each timestep; but then the calculation runs less than half as fast.

Chapter 3

Momentum Balance

The purpose of the momentum balance portion of the calculation is to find the induced velocity at the swept surface. The induced velocity is the change in velocity from far upstream to a location on the swept surface. In other words, the incoming velocity seen by the blade is $V_0 + V_i$, with V_0 the remote velocity vector and V_i the induced velocity vector. Once V_i is known, the local velocity vector at the blade can be calculated as $V = V_0 + V_i - V_b$ (where V_b is due to the motion of the blade). Then the forces along the blade can be calculated by the methods of Chapter 2.

Strictly speaking, the induced velocity is due to vorticity in the wake, which is well-defined only under conditions of attached flow. The flow through the rotor becomes more complicated when the blades stall. Nonetheless, the BEM method is applied at high windspeeds, with results that are accurate enough for a preliminary calculation.

3.1 Momentum Balance Equation

The vector momentum balance equation is:¹

$$F = -2\rho A_e f |(V_0 + fV_i) \cdot n| V_i. \quad (3.1)$$

Here, F is the time-average force at the swept surface,² ρ is the air density, A_e is the area of the element of the swept surface, and f is the Prandtl factor. The term $|(V_0 + fV_i) \cdot n|$ is the rate of flow through the surface element.

F and the rightmost V_i (outside the absolute value sign) can in principle be expressed in any coordinate system; and the terms in the mass flow rate, $|(V_0 + fV_i) \cdot n|$, can also be expressed in any coordinate system. However, when dynamic inflow is considered (Section 3.5) it is most convenient to express momentum balance in the surface coordinate system:

$$F^s = -2\rho A_e f |(V_0^s)_Z + f(V_i^s)_Z| V_i^s, \quad (3.2)$$

where only Z^s components are present in the mass flow rate term, which follows from the definition of the surface coordinate system (Figure 1.1).

¹For example, Wilson and Lissaman [25], Burton et al. [2], and Hansen [7]. Reference [16] contains a derivation which uses the same terminology as this report.

²The time-average force is discussed further in Section 3.4. It represents the force of the air on the blades, rather than the blades on the air; hence the negative sign on the right-hand side of the equation.

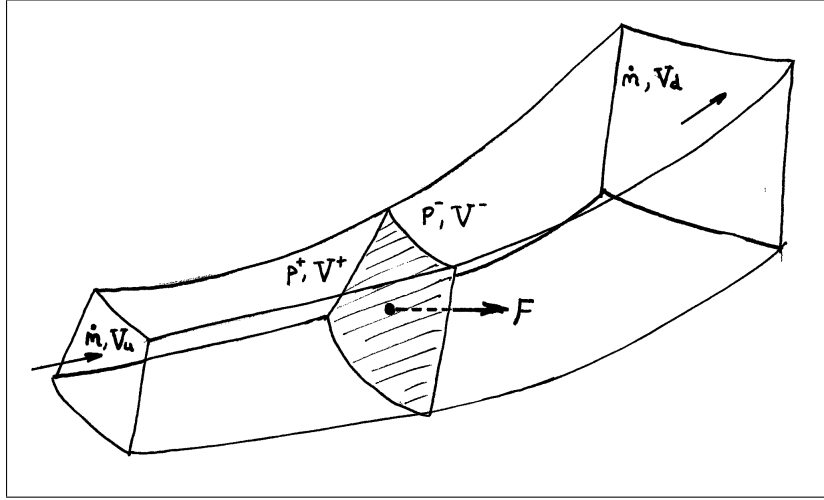


Figure 3.1: A streamtube passing through an element on the swept surface, at which a force is applied; the mass flow rate is conserved in the streamtube, as no flow passes through its walls

Momentum balance applies to a streamtube passing through a fictitious surface in space, at which a force is applied. Such a streamtube is sketched in Figure 3.1. (The variables shown on the sketch are relevant for a detailed derivation of the momentum balance equation, and are not central to the discussion here.) For the concept of a streamtube to be valid, no flow can pass through its walls. This criterion is violated if $(V_i^s)_Z > -0.5(V_0^s)_Z$, because in this case the downstream flow reverses back towards the surface element. The only way this is possible, while preserving the conservation of mass, is for flow to cross the walls of the streamtube. In such a case, the actual physics of the flow would be complicated; but it can be said for certain that (for an energy extraction device) Equation 3.1 does not apply outside the range $0 < (V_i^s)_Z < -0.5(V_0^s)_Z$.³ In the software, $(V_i^s)_Z$ is limited to this range.

As discussed in Section 3.6, a similar constraint is applied to the components $(V_i^s)_X$ and $(V_i^s)_Y$, in order to explicitly prohibit that the blades accelerate the flow.

3.2 Double-Multiple Streamtube BEM

For vertical-axis wind turbines, the BEM method is implemented as a “double-multiple streamtube” calculation. What this means is illustrated in Figure 3.2. Each swept surface element on the upwind side is associated with its mirror element across the (Y_r, Z_r) plane. It is assumed that the flow which leaves the upwind element subsequently impinges on the downwind element. Expansion and deflection of the airflow coming off the upwind half of the rotor are therefore neglected. The flow velocity “far” downstream of the upwind half is $V_m = V_0 + 2V_i$. This “matching” velocity V_m is used as the input to an identical set of calculations on the downwind surface element; V_m for the downwind element is akin to V_0 for the upwind element.

³As a technicality, note that this statement applies for the upwind half of the rotor. Because of the definition of the surface coordinate system, with the normal pointing outwards, the criterion is $0 > (V_i^s)_Z > -0.5(V_0^s)_Z$

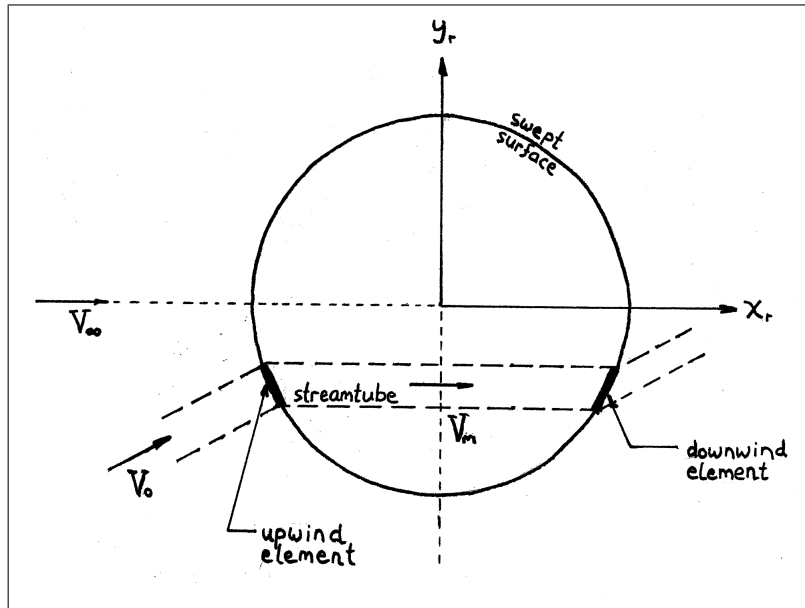


Figure 3.2: Double-multiple streamtube

3.3 Correction for Finite Aspect Ratio

The lift on a blade or wing of finite span goes smoothly to zero at the tips. However the tabulated airfoil data is derived from experiments which approximate an infinite span. Therefore the value of F_b must be modified.

Prandtl [22] developed a simple modification factor that is valid for tip-speed ratios above 5. (At tip speed ratios below 5, the Prandtl factor tends to overpredict the lift force.) The formula is:

$$f = \frac{2}{\pi} \cos^{-1} \left(e^{N_b(r-R)/(2r \sin \phi)} \right), \quad (3.3)$$

with:

$$\sin \phi = \frac{|V \cdot n|}{|V|}. \quad (3.4)$$

The vector V is the flow at the swept surface, including the remote velocity, the induced velocity, and the motion of the blade.

The wake of a straight-bladed (H-rotor) vertical-axis wind turbine is similar to the wake geometry analyzed by Prandtl. It can thus be argued that the Prandtl factor should apply to a straight-bladed VAWT. For a Darrieus turbine, it is expected that the aspect ratio correction is negligible, with $f \approx 1$ over the central portion of the blade that produces the majority of the power.

It was found that the solution could be numerically unstable at the elements adjacent to the blade root (very near the axis of rotation) if the Prandtl factor was applied to a Darrieus turbine. Therefore, while the software can calculate the Prandtl factor, it is recommended to

on the downwind half.

set the factor to 1 when analyzing a Darrieus rotor. The Prandtl factor should be activated when analyzing an H-rotor.

3.4 Induced Velocity

It is not entirely obvious how to calculate the induced velocity over the rotor of a vertical-axis wind turbine, using momentum balance.⁴ There are two things that make the calculation challenging: first, at a given element on the swept surface, a blade is present only a fraction of the time.⁵ Second, because of dynamic stall effects, the blade arrives at the surface element with a state of flow that depends upon what the blade experienced during previous timesteps. Therefore the forces at a given surface element cannot be considered independent of the other surface elements.⁶

Because of these difficulties, there is no consensus on how the induced velocity should be calculated. Several options are presented in the literature.

The simplest option that is shown to give reasonable predictions of *average* power output is the method described by Paraschivoiu.⁷ Here the induced velocity is considered to be constant over the upwind and downwind halves of the swept surface, not a function of the azimuth. In other words, the swept surface is divided into horizontal (constant latitude) bands, with each band being swept by a given spanwise element on the blade. Then the blade forces are integrated over the upwind and downwind halves of rotation. These average forces are used to find the average X^r component of induction, $(\overline{V_i^r})_X$, over the upwind and downwind halves of the band.

Paraschivoiu demonstrates that this sort of simplified calculation can be used to predict the global behavior of the rotor, although omitting the local variations in induced velocity tends to result in a moderate overprediction of power.⁸ Another downside to taking an azimuth-average of the induction is that the instantaneous loads on the blade are not correctly predicted.⁹ Thus if one is concerned with blade structural dynamics or fluctuations in power output, a more refined model is required.

Homicz [8] studied the behavior of a VAWT under atmospheric turbulence, which required knowing the azimuthal variation of induced velocity. Therefore the swept surface was divided both horizontally and vertically into a series of approximately rectangular elements. Instead of taking an azimuthal average of blade forces, Homicz computed the time-average force at each surface element. For a rotor rotating at constant speed, this is equivalent to applying a factor of $N_b \Delta\psi/2\pi$ to the local blade forces; in other words, the blade forces are factored by the fraction of the time that they spend at a given surface element, and this reduced force is used in Equation 3.1 to calculate the induced velocity.

⁴The theory is more straightforward if the wake is explicitly modelled, although in this case the calculations become much more complicated.

⁵Contrast this with a horizontal-axis wind turbine, where the swept surface is defined as an annulus swept by a spanwise section of the blades. In this case, the blades are always “present” at the swept surface.

⁶Again, contrast this with a horizontal-axis wind turbine, where it is typically assumed that each annulus is entirely independent of the others.

⁷Paraschivoiu [21], Section 6.4, describing the CARDAA software. Paraschivoiu later shows results from the CARDAAV software, which implements a local calculation of induced velocity, akin to the method used in this study.

⁸For instance, Paraschivoiu [21] Figure 6.35.

⁹Paraschivoiu [21] Figure 6.39

Homicz made a simplifying assumption in order to decrease the calculation time: the induced velocity was calculated once, based upon steady flow conditions, at the beginning of the calculation. Then, it was assumed that the stochastic turbulence did not affect the induced velocity; in other words, the induced velocity was held constant¹⁰ for the remainder of the analysis.

The assumption that induced velocity is constant in time is expected to be accurate if the velocity fluctuations due to turbulence are small in comparison with the mean velocity, if the frequency band of the turbulence is above the rotor rotational frequency $\Omega/2\pi$, and if Ω is constant. These conditions may be satisfied in certain circumstances. However, the focus of the present project is a variable-speed VAWT. Also, when one looks at plots of windspeed under typical atmospheric conditions, it is seen that the windspeed can depart significantly from the average over a timescale of several tens of seconds. Therefore, it should not be assumed in general that the induced velocity is constant in time.

(That being said, it is also incorrect to assume that the induced velocity follows the local windspeed at each timestep, according to a quasi-steady, iterative solution of Equation 3.1. Rather, the induced velocity changes with the timescale of wake development, typically on the order of the period of one rotor revolution. This time-lag is implemented with a dynamic inflow model, as described in Section 3.5.¹¹)

The question remains, then, how to calculate the appropriate force at each surface element, for use in Equation 3.1. There are two options. One option is to pretend that there is *always*, at each timestep, a blade associated with each surface element. In other words, the momentum balance calculation is performed for each surface element, independently of the actual azimuthal locations of the blades.¹² The problem with this approach is that the effects of dynamic stall must then be extrapolated from the previous *element*, rather than the previous *timestep*. In other words, the effective timestep for the dynamic stall analysis becomes a function of the number of elements that are used, rather than the physical timestep. This is undesirable.

The second option is to track the instantaneous blade forces as the blade sweeps across each surface element, and update the force term in the momentum balance equation only for those elements “containing” one of the blades. In this way, the dynamic stall calculation evolves naturally from one timestep to the next. The problem with this approach is that it tends to be numerically unstable, because the force associated with each element is updated in bursts. Also, it fits poorly with a dynamic inflow model.

A viable solution was found by combining the above two options. The aerodynamic model of the rotor is defined with N_c blades, where N_c is the number of columns into which the azimuth of the rotor is divided; that is, $N_c = 2\pi/\Delta\psi$. There are therefore N_b real blades, and $N_c - N_b$ “ghost” blades, as sketched in Figure 3.3. In this manner, there is always the equivalent of one blade associated with each surface element. As the calculation proceeds,

¹⁰That is, constant in time. The induced velocity was calculated separately for each surface element.

¹¹In typical implementations of the BEM method for HAWTs, dynamic inflow is not very important for stall-regulated turbines. The reason is that it is typical to calculate an average induction about the annulus swept by a given blade element. This area is spread over a large region of space, so high-frequency components of turbulence are not correlated, and tend to average to zero. The low-frequency components of turbulence, which are correlated over large distances, affect the induction in a quasi-steady manner. The situation is different for a VAWT, where one is looking at a small element on the swept surface. The induced velocity at such an element should not follow the high-frequency components of turbulence, therefore it is important to implement a time-lag.

¹²The calculated airfoil coefficients are factored by $N_b \Delta\psi/2\pi$, to provide the appropriate magnitude.

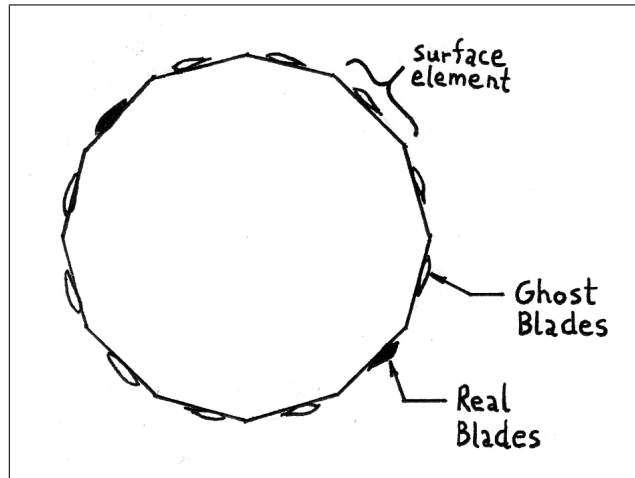


Figure 3.3: An illustration of ghost blades for a single row of elements about the rotor azimuth; the number of elements has been reduced for convenience of sketching ($N_c = 36$ has been used in the analyses in this report)

the state of flow about each blade, including dynamic stall, is allowed to evolve freely. The force associated with each surface element, for use in Equation 3.1, is taken as an average of the forces at the two adjacent blades, weighted linearly according to the distance of each blade from the element centroid, and factored by N_b/N_c .

Using ghost blades allows the induced velocity at each surface element to evolve naturally according to the dynamic inflow model, while at the same time the aerodynamic forces are allowed to evolve naturally according to the dynamic stall model. The calculation remains valid in the presence of turbulence and during changes in the rotational speed.

In the event that structural calculations are being performed, it is sufficient to limit aeroelastic analysis to the real blades, and consider the ghost blades to be perfectly rigid.

The downside of the ghost blade calculation is that it is slow, particularly when it comes to interpolating airfoil coefficients at each timestep for each blade. For a quick, approximate analysis, it is recommended to revert to the method of Homicz: run a ghost blade analysis until induced velocities converge (roughly one revolution, if the dynamic inflow method of Section 3.5 is used), then freeze the induced velocities and consider only the real blades for the remainder of the analysis.

Note that induced velocities can be neglected when checking extreme gust loads, because at high windspeeds V_i is small with respect to V_0 .

3.5 Dynamic Inflow

At each timestep, Equation 3.1 is solved in the following manner:

$$V_i = \frac{-F}{2\rho A_e f |(V_0^s)_Z + f(V_i^s)_Z|}, \quad (3.5)$$

where $(V_i^s)_Z$ is taken to be the value at the previous timestep. (It is typically initialized to zero for the first timestep.) There are a couple issues with Equation 3.5, though. First, if

iterated directly (including the necessary updating of F and f), it tends to be numerically unstable. Second, the induced velocity is caused by vorticity in the wake, and therefore evolves on the same timescale as the wake, typically on the order of the period of one rotor revolution.

A dynamic inflow analysis addresses both these problems. A time-lag is introduced such that the induced velocity changes with the appropriate timescale. This introduces sufficient numerical damping so that the calculation is always stable.¹³

It does not appear, based upon a literature review, that a simple engineering-type dynamic inflow model has been developed specifically for VAWTs.¹⁴ Therefore a model developed for HAWTs has been borrowed: the T.U. Denmark (TUDk) model described in Snel and Schepers [24]. In principle, the timescale of evolution of vorticity in the wakes of a HAWT and VAWT should be similar, therefore it is expected that the model is applicable, if not precise.

The TUDk model consists of two time lags in series:

$$v' + \tau_1 \frac{dv'}{dt} = v_q + 0.6\tau_1 \frac{dv_q}{dt}; \quad (3.6)$$

$$v + \tau_2 \frac{dv}{dt} = v'. \quad (3.7)$$

Here v_q is the quasi-steady induced velocity: V_i calculated according to Equation 3.5, using the instantaneous force at the surface element. v' is an intermediate variable, and v is the output, time-delayed induced velocity, that is used in the calculations of blade forces in the next timestep.

The time constants have been derived based upon horizontal-axis wind turbines. The first time constant is:

$$\tau_1 = \frac{1.1}{1 - 1.3a} \left(\frac{R}{|V_0|} \right), \quad (3.8)$$

where:

$$a = \frac{|V_i|}{|V_0|}. \quad (3.9)$$

For purposes of VAWT analysis, R is taken to be the outer radius of the rotor. The second time constant is:

$$\tau_2 = \left[0.39 - 0.26 \left(\frac{r}{R} \right)^2 \right] \tau_1. \quad (3.10)$$

Since, for a VAWT, r/R is poorly defined in this context, it is simply set equal to 0.7 to represent a “typical” value. Thus:

$$\tau_2 = 0.263\tau_1. \quad (3.11)$$

¹³... unless one uses a ridiculously large timestep.

¹⁴Wake vortex and CFD models implicitly include the relevant physics.

3.6 Vector Versus X^r Momentum Balance

References describing the double-multiple streamtube BEM method, such as Paraschivoiu [21], consider only the X^r component of induced velocity $(V_i^r)_X$. In general, the conservation of momentum (Newton's law) applies to each component of a vector: acceleration is aligned with the direction of force. In the case of a VAWT streamtube, the force at the airfoil includes axial, horizontal, and vertical components, and by Equation 3.1 it is expected that the direction of induced velocity opposes that of the force.

The BEM method does not indicate how the streamtubes evolve as they pass through the interior of the rotor. As stated in Section 3.2, it is assumed that the streamtubes pass directly through the rotor, aligned with the mean wind direction.¹⁵ It would be expected that Y^r and Z^r components of induced velocity would change the direction of the streamtubes. Therefore, there are physical inconsistencies with the DMST BEM method, whether momentum balance is performed considering only the X^r component, or all three vector components, of induced velocity.

Two versions of the present software were created, one performing full vector momentum balance, and the other including only $(V_i^r)_X$, setting $(V_i^r)_Y = (V_i^r)_Z = 0$. Comparing output of the two versions, it was observed that differences in global, mean rotor loads were small: Figure 3.4 is typical. However, local airfoil forces may be different, especially away from the equator. Figures 3.5 shows an example of local blade thrust $(F^r)_X$ and torque (tangential force times distance from the rotor axis) at a location near the equator, and Figure 3.6 shows the same quantities at a location away from the equator. The net effect of including transverse components of induced velocity is to transfer a portion of the energy extraction from the upwind to the downwind side of the rotor.

Working in the surface coordinate system, it is not entirely clear from the basic momentum theory what constraints should be placed on the X^s and Y^s components of induced velocity. Here it was decided to use the same type of constraint as for the Z^s component; that is, $0 < (V_i^s)_X < -0.5(V_0^s)_X$ and $0 < (V_i^s)_Y < -0.5(V_0^s)_Y$. In this way, no component of the incoming flow is allowed to reverse, nor accelerate, downstream of the rotor.

Full vector momentum balance has been adopted as the default. It is suspected that this may provide a more accurate estimate of induced velocity when flow over part of the rotor departs from the mean wind direction, as in a turbulent wind field. It may also give a more accurate estimate of induced velocity when the rotor is tilted (there is an incoming flow component along the Z^r axis). However, there is a lack of data which can be used to substantiate this.

¹⁵Paraschivoiu [21], pp 189-199, provides a method that can be used to estimate expansion of the streamtubes as they pass through the rotor, although only the X^r component of induced velocity is considered in the formulation. Modelling streamtube expansion in this manner does not have a significant effect on calculated blade loads.

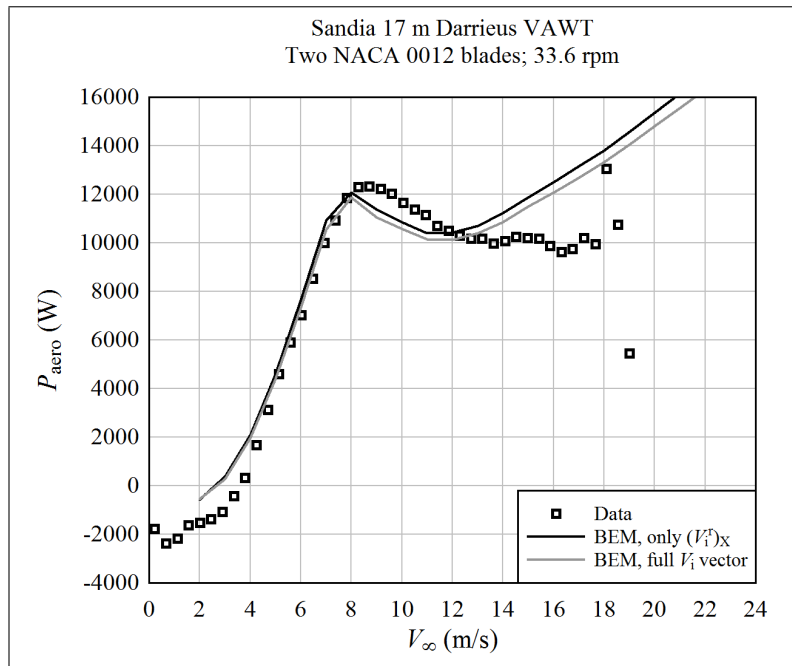


Figure 3.4:

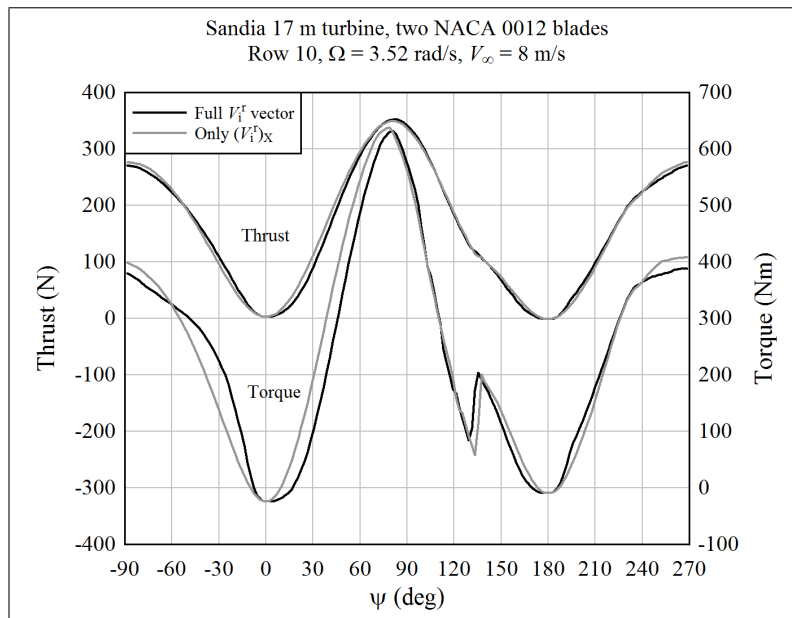


Figure 3.5:

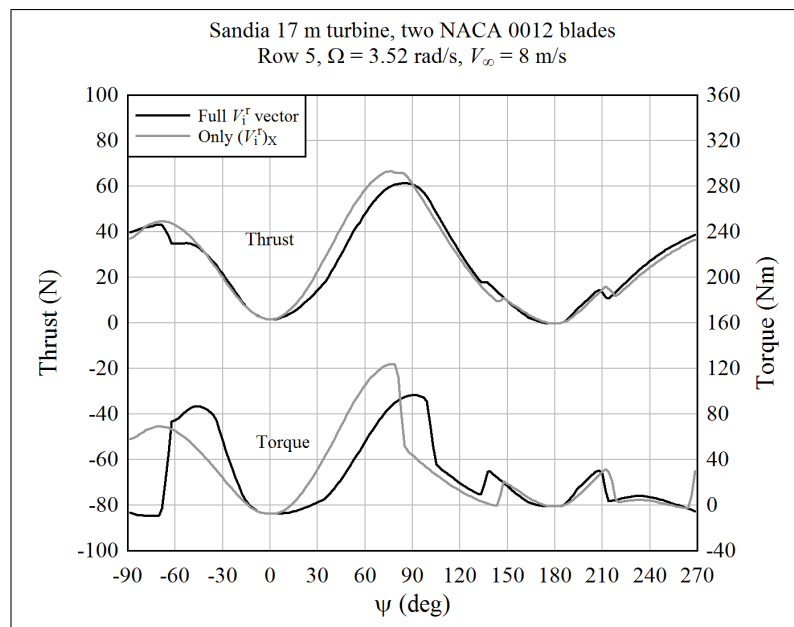


Figure 3.6:

Chapter 4

Validation

Operating data has been published for a number of VAWTs.¹ Among the published results, however, it is difficult to find a complete description that allows reproduction of the measurements. In particular, it is especially hard to find reliable airfoil coefficient data, at the appropriate Reynolds numbers.

The behavior of a VAWT at and above the rated power is very sensitive to the stall behavior of the airfoils. In other words, the behavior of the airfoil as the angle-of-attack approaches and exceeds the value at the maximum lift coefficient determines the behavior of the VAWT at high windspeeds.

Unfortunately, the lift and drag behavior beyond the maximum lift coefficient has traditionally been omitted from published airfoil datasets.² The data in this range was measured,³ but not reported; it was not of interest to aircraft designers. In addition, symmetric airfoils, as used on VAWTs, have not been studied as extensively as cambered airfoils, as used on HAWTs or airplane wings.

As a result, the validation here is limited to one turbine, the Sandia 17 m diameter research prototype, tested in the late 1970's and early 1980's. The geometry of this turbine and measurements of the output power are described by Worstell.⁴ The NACA 0012 airfoil was used for the blades; coefficients, including the critical range of stall, are provided by Sheldahl.⁵ Although lift curves were reported up to $Re = 1.76 \times 10^6$, deep-stall drag coefficients were reported only up to $Re = 7 \times 10^5$. (It is not known why Sheldahl did not give the full drag curves for $Re = 1.76 \times 10^6$.) Therefore the trends seen at $Re = 7 \times 10^5$ had to be extrapolated to higher Reynolds numbers.⁶ Figure 4.1 shows the lift and drag coefficients that were used in the validation analyses.

Figures 4.2 through 4.8 compare the measured and calculated power curves of the Sandia

¹Paraschivoiu [21], Chapter 7, provides an overview of laboratory experiments and prototypes through the year 2002.

²For example, Abbott and von Doenhoff [1].

³Early NACA reports, like Goett and Bullivant [4], give full lift and drag data. But in these early tests there were errors in the drag measurement. [10]

⁴Worstell ([26] and [27])

⁵Sheldahl [23]. Only the experimentally-measured coefficients reported by Sheldahl should be trusted. Analytically-derived coefficients are also reported, but these contain errors in the lift and drag trends in the stalled range.

⁶Abbott and von Doenhoff [1] was used for the lift curve at $Re = 3 \times 10^6$, but drag data was not available past the point of maximum lift.

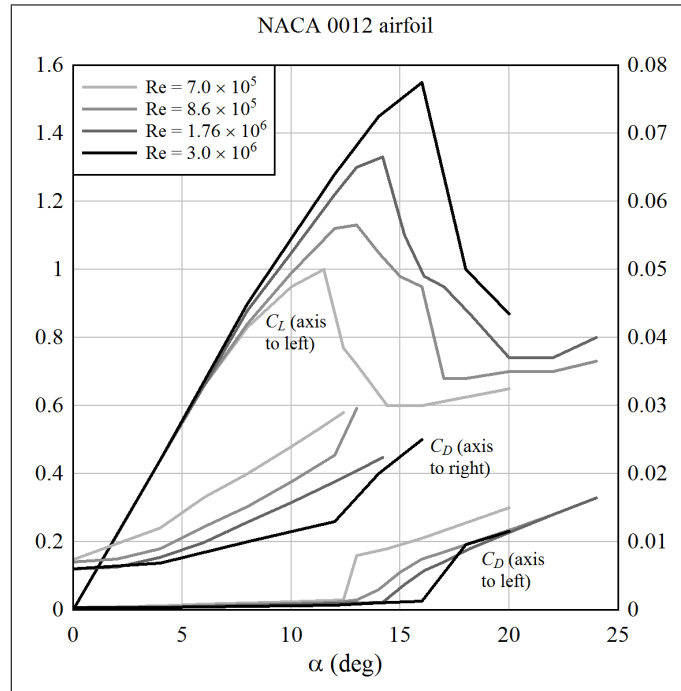


Figure 4.1: Estimated coefficients for the NACA 0012 airfoil

17 m turbine. First, focus on the attached-flow range, below the rated windspeed.⁷ It is seen that, in this range, the trend in output power is well-predicted at low rotational speeds, and moderately overpredicted at high rotational speeds.

Below the rated windspeed, airfoil lift and drag data was available, and dynamic stall is not an issue. That the predictions of power are reasonably accurate in this range indicate that the implementation of the double-multiple streamtube momentum balance calculation is correct.

Above the rated windspeed, the behavior of a VAWT is very sensitive to the properties of the airfoils in stall, as well as the dynamic stall model. As described in the sections above, the coefficients are somewhat uncertain in the stalled range, and the dynamic stall model is one of the simplest available. Therefore, it is not surprising that the calculations do not precisely match the data. It is suspected, based upon a study by Paraschivoiu [21], that the underprediction of power is due primarily to the overly simple dynamic stall model, which does not consider phenomena such as leading-edge vortex shedding. That being said, the Øye dynamic stall model provides a large improvement over quasi-steady coefficients. This can be seen in the plots at 29.6 and 52.5 rpm, which include analyses with and without dynamic stall.

Figure 4.9 and 4.10 show power curves for the same turbine, but with three blades instead of two. The results are similar to those from the two-bladed case.

As another verification check, the power and thrust curves of the Deepwind 5 MW preliminary design, described in an informal document, was analyzed. The Deepwind 5 MW design uses NACA 0018 airfoils, for which reliable coefficient data was not available. Lift coefficient

⁷The rated windspeed can be taken as the windspeed at which the calculated power is maximum.

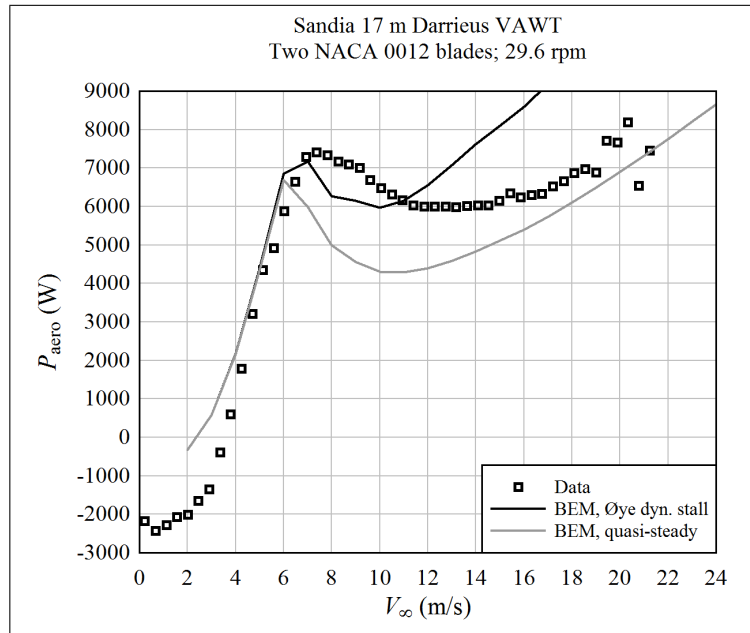


Figure 4.2: Aerodynamic power versus windspeed for the Sandia 17 m diameter turbine; two NACA 0012 blades; 29.6 rpm

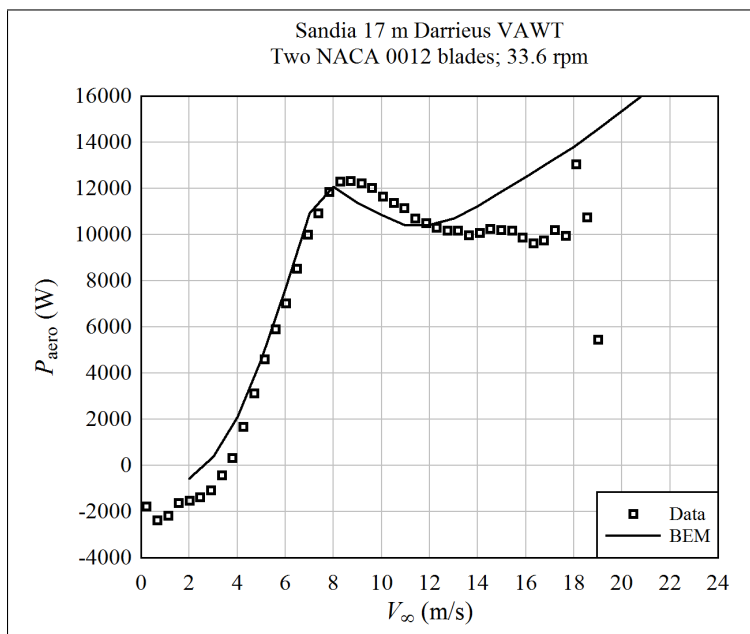


Figure 4.3: Aerodynamic power versus windspeed for the Sandia 17 m diameter turbine; two NACA 0012 blades; 33.6 rpm

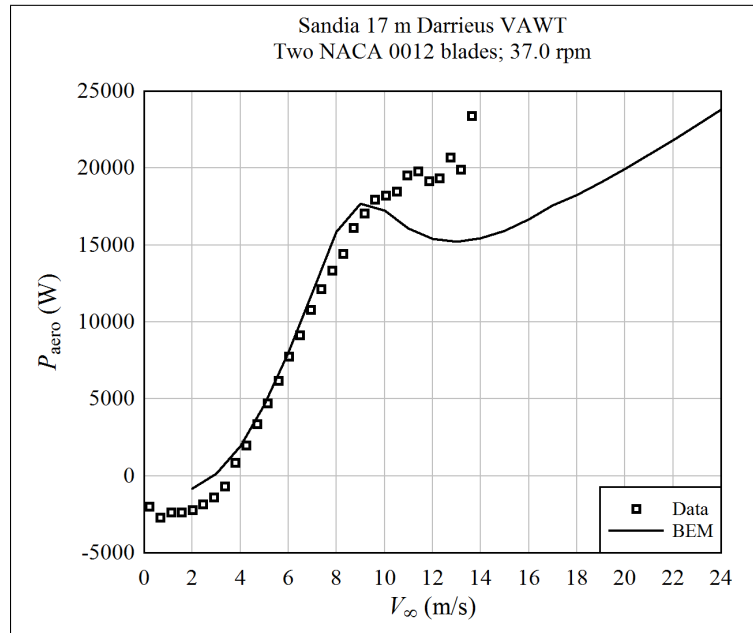


Figure 4.4: Aerodynamic power versus windspeed for the Sandia 17 m diameter turbine; two NACA 0012 blades; 37.0 rpm

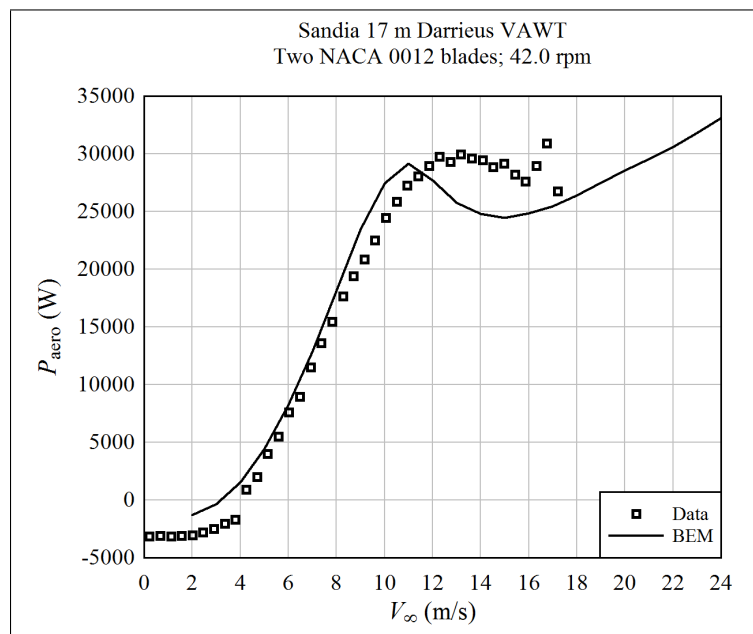


Figure 4.5: Aerodynamic power versus windspeed for the Sandia 17 m diameter turbine; two NACA 0012 blades; 42.0 rpm

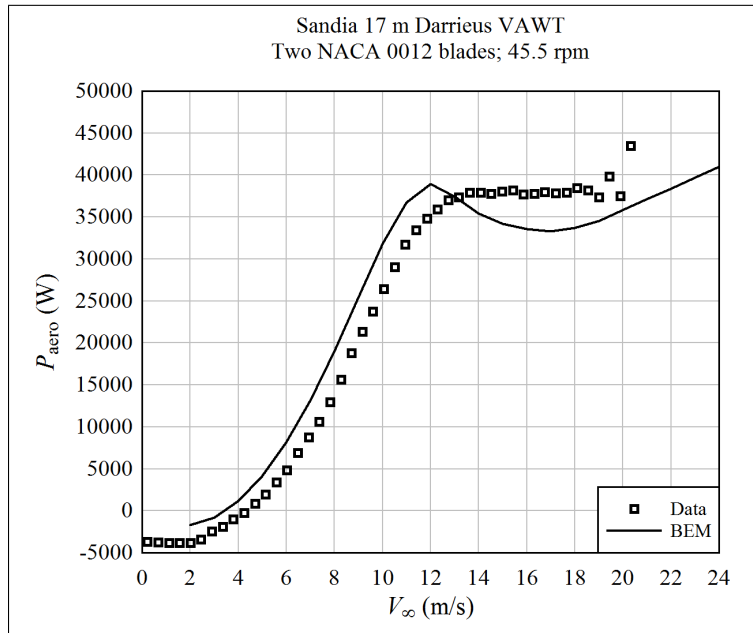


Figure 4.6: Aerodynamic power versus windspeed for the Sandia 17 m diameter turbine; two NACA 0012 blades; 45.5 rpm

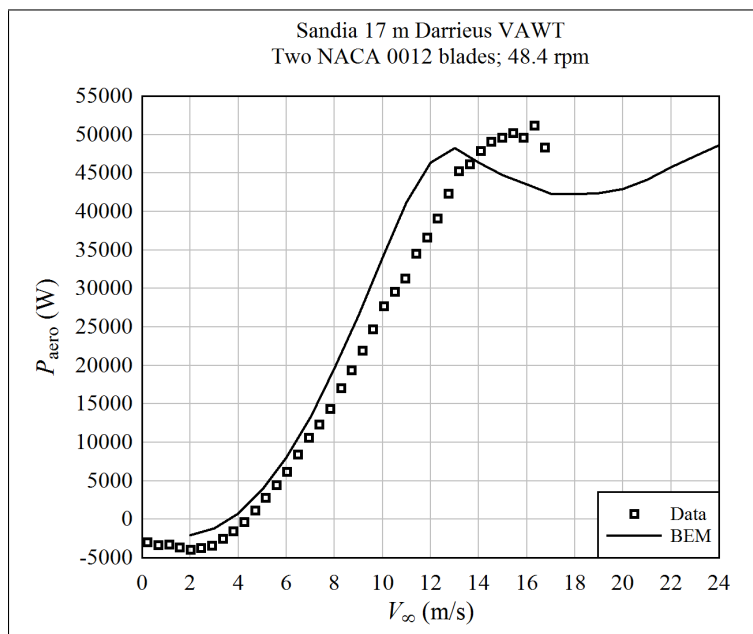


Figure 4.7: Aerodynamic power versus windspeed for the Sandia 17 m diameter turbine; two NACA 0012 blades; 48.4 rpm

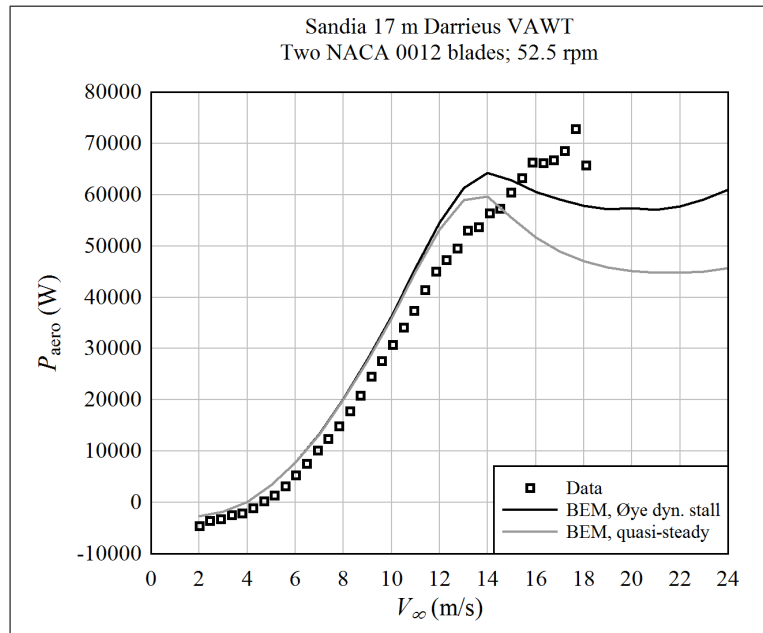


Figure 4.8: Aerodynamic power versus windspeed for the Sandia 17 m diameter turbine; two NACA 0012 blades; 52.5 rpm

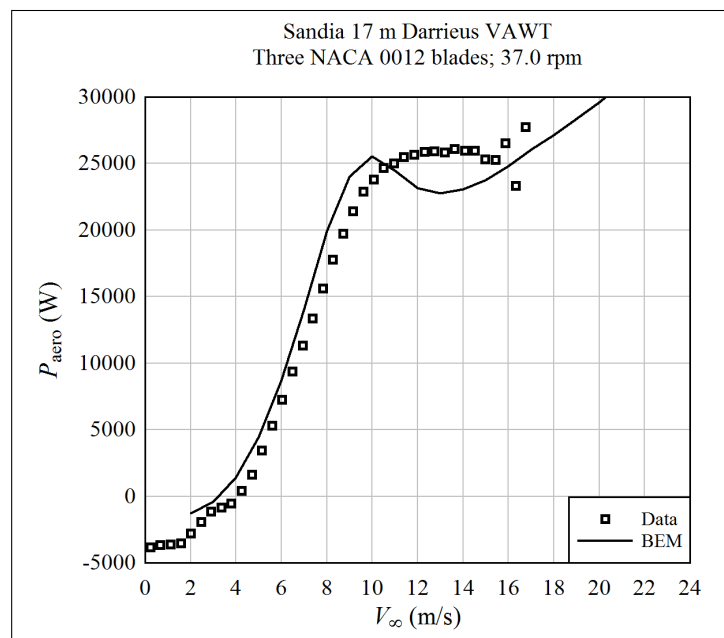


Figure 4.9: Aerodynamic power versus windspeed for the Sandia 17 m diameter turbine; three NACA 0012 blades; 37.0 rpm

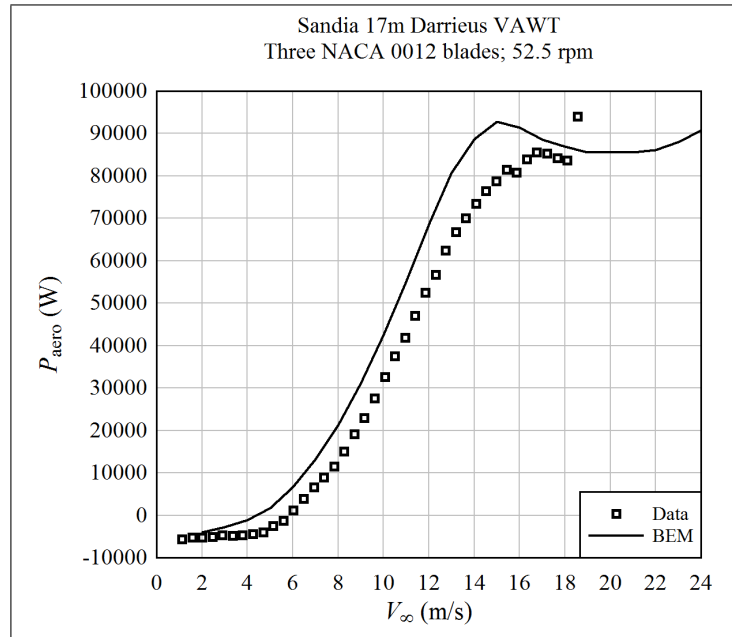


Figure 4.10: Aerodynamic power versus windspeed for the Sandia 17 m diameter turbine; three NACA 0012 blades; 52.5 rpm

data was taken from Jacobs and Sherman [9], but the drag data from this reference is not reliable. Therefore, drag was estimated based upon an empirical model in the author's thesis. [17]

The predicted power curves are shown in Figure 4.11. It appears that the analytical results in the design document were obtained without including dynamic stall. The difference between the two curves which do not include dynamic stall can likely be attributed to the airfoil coefficients.

Figure 4.12 compares the thrust curves. The results using quasi-steady coefficients compare well with the Deepwind reference values.

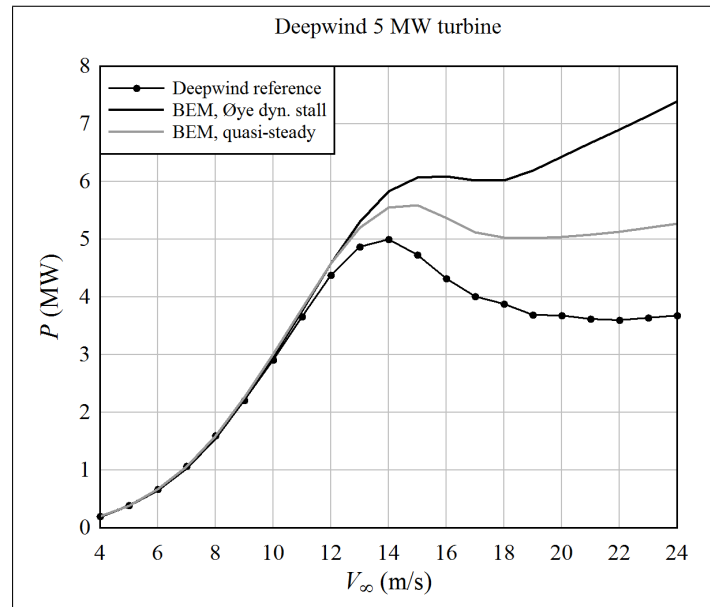


Figure 4.11: Average aerodynamic power versus windspeed for the Deepwind 5 MW preliminary design, compared against analytical results in the informal document describing the design

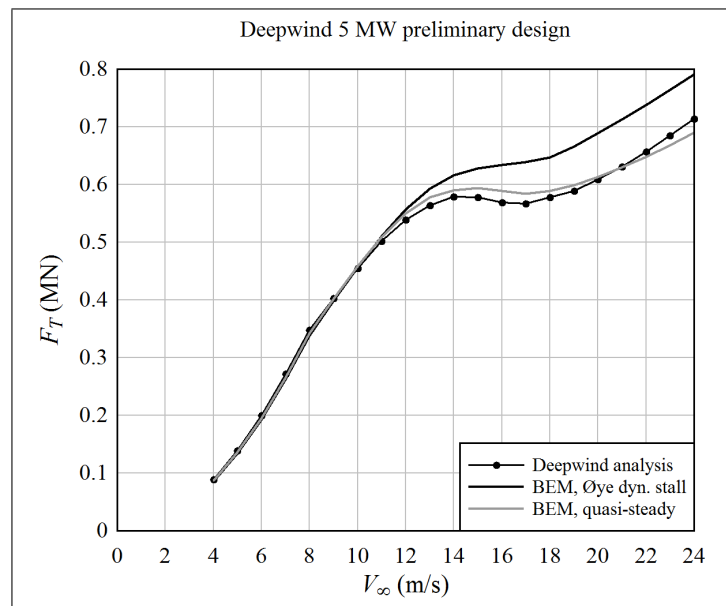


Figure 4.12: Average thrust versus windspeed for the Deepwind 5 MW preliminary design, compared against analytical results in the informal document describing the design

Chapter 5

Conclusions

A double-multiple streamtube BEM method has been programmed. The method provides aerodynamic loads on the blades of a VAWT, under conditions in which windspeeds fluctuate. The software is suitable for modelling the behavior of a VAWT in the presence of atmospheric turbulence, wakes from upwind turbines, or motion of the support platform.

The double-multiple streamtube BEM method is accurate when flow on the blades is attached, below the rated windspeed. Above the rated windspeed, when the blades are stalled, predictions of power output are poor. For more accurate estimates, it is necessary to calibrate the aerodynamic properties of the airfoils empirically; this is especially so for the model of dynamic stall.

The BEM method implemented here explicitly models many blades about the rotor azimuth, most of which are fictitious. Using such “ghost” blades allows the induced velocity, associated with each element on the swept surface, to respond smoothly to fluctuations in the local windspeed. The induced velocity and loads on the blades evolve naturally according to dynamic stall and dynamic inflow models.

The BEM method may be used for preliminary aerodynamic and structural design of a VAWT rotor. For detail design and certification, it is recommended to implement a more robust aerodynamic model.

Bibliography

- [1] Abbott, I.H.; von Doenhoff, A.E.; *Theory of Wing Sections, Including a Summary of Airfoil Data*; Dover Publications, New York, USA, 1959
- [2] Burton, T., et al.; *Wind Energy Handbook*; John Wiley & Sons, UK, 2001
- [3] Fuglsang, P., et al.; “Wind Tunnel Test of the Risø-1 Airfoil”; Report Risø-R-999(EN), Risø National Laboratory, Roskilde, Denmark, 1998
- [4] Goett, H.J.; Bullivant, W.K.; “Tests of N.A.C.A. 009, 0012, and 0018 Airfoils in the Full-Scale Tunnel”; Report No. 647, National Advisory Committee for Aeronautics, USA, 1938
- [5] Gupta, S.; Leishman, J.G.; “Dynamic Stall Modelling of the S809 Aerofoil and Comparison with Experiments”; *Wind Energy* 9 (2006) 521-547
- [6] Hansen, M.H., et al.; “A Beddoes-Leishman Type Dynamic Stall Model in State-Space and Indicial Formulations”; Risø National Laboratory Report Risø-R-1354, Roskilde, Denmark, 2004
- [7] Hansen, M.O.L.; *Aerodynamics of Wind Turbines*; Second Edition, Earthscan, London, UK, 2008
- [8] Homicz, G.F.; “Numerical Simulation of VAWT Stochastic Aerodynamic Loads Produced by Atmospheric Turbulence: VAWT-SAL Code”; Report SAND91-1124, Sandia National Laboratories, Albuquerque, NM, USA, 1991
- [9] Jacobs, E.N.; Sherman, A.; “Airfoil Section Characteristics as Affected by Variations of the Reynolds Number”; Report No. 586, National Advisory Committee for Aeronautics, USA, 1937
- [10] Jacobs, E.N.; Abbott, I.H.; “Airfoil Section Data Obtained in the N.A.C.A. Variable-Density Tunnel as Affected by Support Interference and Other Corrections”; Report No. 669, National Advisory Committee for Aeronautics, USA, 1939
- [11] Larsen J.W.; Nielsen S.R.K.; Krenk S.; “Dynamic Stall Model for Wind Turbine Airfoils”; *Journal of Fluids and Structures* 23 (2007) 959-982
- [12] Leishman, J.G.; “Challenges in Modelling the Unsteady Aerodynamics of Wind Turbines”; *Wind Energy* 5 (2002) 85-132

- [13] Leishman, J.G.; Beddoes, T.S.; “A Generalised Model for Airfoil Unsteady Aerodynamic Behaviour and Dynamic Stall Using the Indicial Method”; Proceedings of the 42nd Annual Forum of the American Helicopter Society, Washington, D.C., June 1986, 243-265
- [14] Leishman, J.G.; Beddoes, T.S.; “A Semi-Empirical Model for Dynamic Stall”; Journal of the American Helicopter Society 34 (1989) 3-17
- [15] Lindenburg, C.; “Investigation into Rotor Blade Aerodynamics – Analysis of the stationary measurements on the UAE phase-VI rotor in the NASA-Ames wind tunnel”; Report ECN-C-03-025, Energy Research Centre of the Netherlands, 2003
- [16] Merz, K.O.; “BA8607 Final Project: Preliminary Concepts and Aerodynamic Analysis Methods for a Vertical-Axis Deepwater Offshore Wind Turbine”; Norwegian University of Science and Technology (NTNU), Department of Civil and Transport Engineering, Trondheim, Norway, 2009
- [17] Merz, K.O.; *Conceptual Design of a Stall-Regulated Rotor for a Deepwater Offshore Wind Turbine*; Doctoral Thesis 2011:191, Department of Civil Engineering, Norwegian University of Science and Technology, 2011
- [18] Merz, K.O.; “A Method for Analysis of VAWT Aerodynamic Loads under Turbulent Wind and Platform Motion”; to be presented at the 9th Deep Sea Offshore Wind R&D Seminar, Trondheim, Norway, January 19-20, 2012
- [19] Moriarty, P.J.; Hansen, A.C.; “Aerodyn Theory Manual”; Report NREL/TP-500-36881, National Renewable Energy Laboratory, Golden, CO, USA, 2005
- [20] Øye, S.; “Dynamic Stall, Simulated as a Time Lag of Separation”; McAnulty, K.F. (editor); Proceedings of the Fourth IEA Symposium on the Aerodynamics of Wind Turbines, ETSU-N-118, 1991
- [21] Paraschivoiu, I.; *Wind Turbine Design, with Emphasis on Darrieus Concept*; Polytechnic International Press, Montréal, Québec, Canada, 2002
- [22] Prandtl, L. (translated by the staff of the National Advisory Committee for Aeronautics); “Applications of Modern Hydrodynamics to Aeronautics”; NACA Report 116, USA, 1921
- [23] Sheldahl, R.E.; Klimas, P.C.; “Aerodynamic Characteristics of Seven Symmetrical Airfoil Sections Through 180-Degree Angle of Attack for Use in Aerodynamic Analysis of Vertical Axis Wind Turbines”; Report SAND80-2114, Sandia National Laboratories, Albuquerque, NM, USA, 1981
- [24] Snel, H.; Schepers, J.G.; “Joint Investigation of Dynamic Inflow Effects and Implementation of an Engineering Method”; ECN Report ECN-C-94-107, Energy Research Centre of the Netherlands, 1995
- [25] Wilson, R.E.; Lissaman, P.B.S.; “Applied Aerodynamics of Wind Power Machines”; Oregon State University, USA, 1974

- [26] Worstell, M.H.; “Aerodynamic Performance of the 17 Meter Diameter Darrieus Wind Turbine”; Report SAND78-1737, Sandia National Laboratories, Albuquerque, NM, USA, 1978
- [27] Worstell, M.H.; “Aerodynamic Performance of the 17-M-Diameter Darrieus Wind Turbine in the Three-Bladed Configuration: An Addendum”; Report SAND79-1753, Sandia National Laboratories, Albuquerque, NM, USA, 1979